

# Synthesis of Three Types of $\text{LiVOP04}$ ( $\alpha$ , $\alpha 1$ , and $\beta$ ) and the Electrochemical Characteristics in Li-ion Battery

野島, 昭信

<https://doi.org/10.15017/4060195>

---

出版情報 : Kyushu University, 2019, 博士 (工学) , 課程博士  
バージョン :  
権利関係 :



# **Synthesis of Three Types of $\text{LiVOPO}_4$ ( $\alpha$ , $\alpha_1$ , and $\beta$ ) and the Electrochemical Characteristics in Li-ion Battery**

(3種類の  $\text{LiVOPO}_4$ ( $\alpha$ ,  $\alpha_1$ , and  $\beta$ )の合成とリチウムイオン電池におけるその電気化学特性)

Supervisor: Prof. Shigeto Okada

Akinobu Nojima

March 2020

Institute for Materials Chemistry and Engineering  
Kyushu University

# Contents

Chapter 1. Introduction.....	3
1. 1 Background of Li ion secondary batteries .....	4
1. 1. 1 Trends in energy demand .....	4
1. 1. 2 Li ion battery market.....	8
1. 2 Li ion secondary batteries .....	13
1. 2. 1 Structure and principle of Li ion secondary batteries .....	13
1. 2. 2 Cathode materials for Li ion secondary batteries.....	21
1. 3 LiVOPO <sub>4</sub> background .....	26
1. 4 Objectives of this study.....	32
References.....	33
Chapter 2. Evaluation of LiVOPO <sub>4</sub> Synthesized by Hydrothermal Method.....	37
2. 1 Introduction.....	38
2. 2 Experimental.....	39
2. 2. 1 Synthesize for LiVOPO <sub>4</sub> .....	39
2. 2. 2 Electrode and half-cell fabrication, and evaluation method .....	42
2. 2. 3 Analysis method .....	43
2. 3 Results and Discussion .....	44
2. 3. 1 Evaluation of phase transition by <i>in-situ</i> heating XRD .....	44
2. 3. 2 Evaluation of crystallinity of LiVOPO <sub>4</sub> .....	46
2. 3. 3 Electrochemical evaluation for LiVOPO <sub>4</sub> .....	53
2. 3. 4 Lithium deintercalation capability of LiVOPO <sub>4</sub> .....	59
2. 4 Conclusions.....	63
References.....	64

Chapter 3. Electrochemical Characterization, Structural Evolution, and Thermal Stability of LiVOPO <sub>4</sub> over Multiple Lithium Intercalations .....	65
3. 1 Introduction.....	66
3. 2 Experimental.....	67
3. 2. 1 Preparation for LiVOPO <sub>4</sub> .....	67
3. 2. 2 Electrode and half-cell fabrication, and evaluation method .....	68
3. 2. 3 Characterization for LiVOPO <sub>4</sub> .....	69
3. 3 Results and Discussion .....	72
3. 3. 1 Electrochemical performance at low voltage region .....	72
3. 3. 2 Crystal evolution of LiVOPO <sub>4</sub> in charge/discharge .....	76
3. 3. 3 Evaluation of valence of vanadium for LiVOPO <sub>4</sub> by XAFS .....	81
3. 3. 4 Thermal stability of LiVOPO <sub>4</sub> .....	90
3. 4 Conclusions.....	93
References.....	94
 Chapter 4. Bipolar battery using LiVOPO <sub>4</sub> .....	 96
4. 1 Introduction.....	97
4. 2 Experimental.....	98
4. 3 Results and Discussion.....	100
4. 4 Conclusions.....	112
References.....	113
 Chapter 5. Conclusions.....	 114
 Acknowledgement.....	 119

# Chapter 1

## Introduction

## **1. 1 Background on Li ion batteries**

### **1. 1. 1 Trends in energy demand**

The production of energy and food are important issues as the global population increases. Demand for energy is an issue that should be considered on a global scale in relation to the depletion of fossil fuels and pollution of the global environment. Electricity is an indispensable energy for daily life and is the energy produced by many fossil fuels. However, fossil fuels are known to emit high levels of CO<sub>2</sub> emissions during energy production. CO<sub>2</sub> is a greenhouse gas, so high levels of CO<sub>2</sub> emissions have led to a serious global warming problem. Figure 1-1 shows the amount of CO<sub>2</sub> emissions from power generation in Japan <sup>1)</sup>. These values include the energy consumed to manufacture and eventually disposal of power-generation equipment. The data indicate that renewable energy is good for the global environment not only during operation but also but also during periods of nonproduction. Therefore, replacement of fossil fuel energy with renewable energy is an effective means to solve environmental issues in power generation. Figure 1-2 shows energy demand cited in a 2019 white paper published by the Japanese government's Agency for Natural Resources and Energy. The share of nuclear power generation has declined since the Great East Japan Earthquake, and fossil fuels and natural gas have replaced that share. According to one study of trends in energy demand, the share of renewable energy, such as solar, wind, and geothermal power generation, is increasing in the domestic primary energy supply <sup>2)</sup>. The benefits of introducing renewable energy are very diverse, from global issues related to global warming countermeasures to Japan's energy policies such as improving energy self-sufficiency and reducing fossil fuel procurement funds, as well as to Japan's industrial policy such as strengthening the international competitiveness of industries <sup>3)</sup>. Japan of course is not alone in its desire to promote the use of renewable energy. The penetration rate of renewable energy is particularly high in Europe, where environmental concerns are deeply entrenched. In China, the efforts to increase renewable energy are increasing along with economic growth. The introduction of solar power generation around the world has accelerated since the late 2000s, and by the end of 2017 approximately 400 million kW of cumulative solar energy capacity had been installed. In addition, the large expansion

of the solar power generation market has led to a reduction in the cost of introducing power generation facilities, and in recent years it has also spread to emerging countries. In particular, China overtook Germany in 2015 as the country with the highest installed solar power capacity <sup>4)</sup>. The world's wind power generation capacity has also increased rapidly in recent years, reaching about 590 million kW in 2018. China (211.3 million kW), which accounts for about one-third of the global total, has the largest installed volume, followed by the United States (96.67 million kW) and Germany (59.56 million kW). Therefore, these three countries account for about 60% of the world's wind power generation capacity <sup>4)</sup>. In this way, efforts to increase renewable energy are spreading all over the world.

However, renewable power generation systems are not stable. For example, solar power systems cannot generate electric power at night. Naturally, wind power also cannot generate electric power on windless days. Energy consumption has peak and off-peak periods by day and by season, and these do not necessarily coincide with periods of power generation. Therefore, in order to spread renewable energy, it is necessary to balance the supply and demand of energy in combination with energy storage systems. According to the Ministry of Economy, Trade and Industry's technology roadmap, lithium-ion batteries, redox flow batteries, and sodium-sulfur batteries are potential storage systems <sup>5)</sup>. Electric power companies are promoting the introduction of large storage battery systems in order to popularize renewable energy. For example, Hokkaido Electric Power Co. has introduced the redox flow battery. Kyushu Electric Power Co. has introduced a large-scale sodium-sulfur battery. Tohoku Electric Power Co. has introduced large-scale lithium ion secondary batteries (LIBs) in two locations. These introduction attempts have been proven to affect the balance of energy supply and demand. Therefore, lithium-ion batteries play an important role in spreading renewable energy.

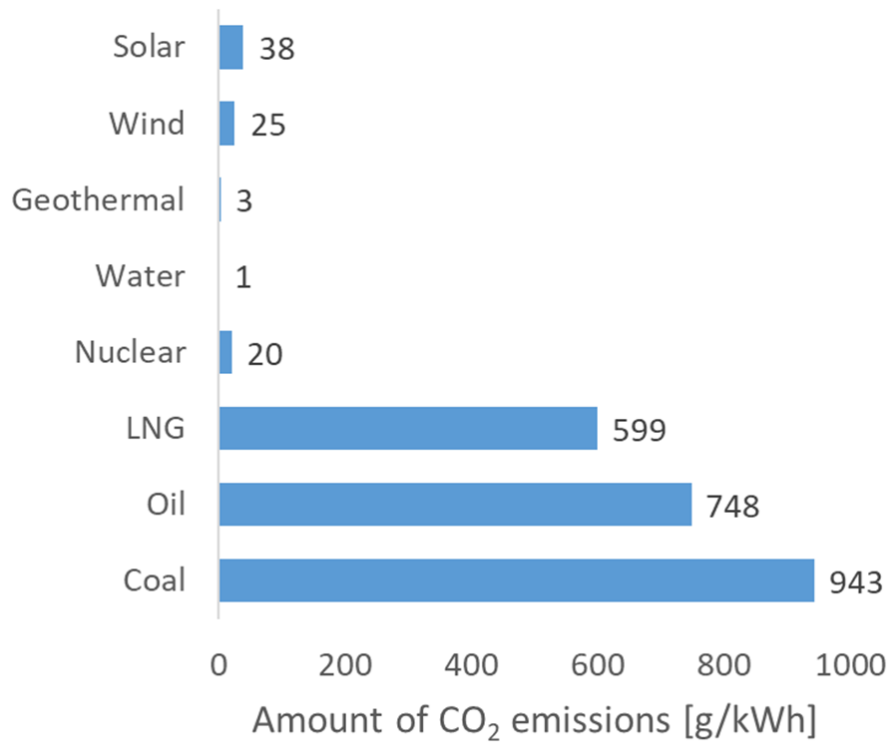


Fig. 1-1. CO<sub>2</sub> emissions based on a report by the Central Research Institute of Power Industry (2016).

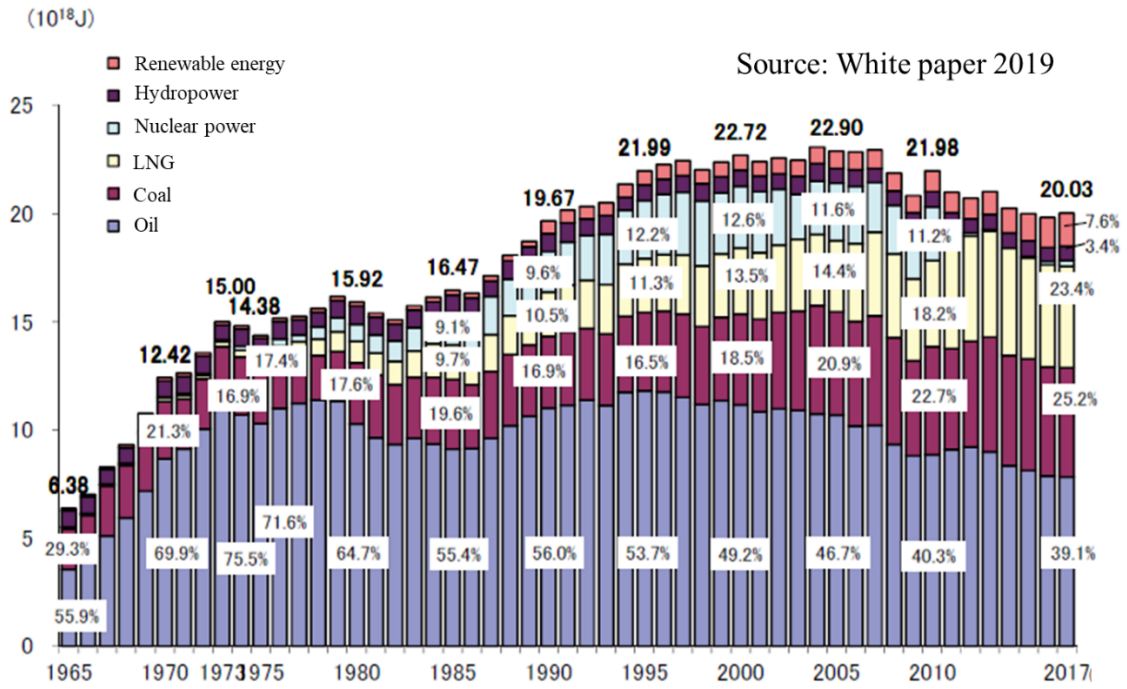


Fig. 1-2. Trends in energy demand based on a 2019 white paper published by the Agency for Natural Resources and Energy <sup>2)</sup>.

### 1. 1. 2 Li ion battery market

With the development of mobile devices such as mobile phones and notebook PCs, power sources with higher energy density have been required to allow the manufacture of smaller and lighter devices. Therefore, it can be said that the spread of LIBs has progressed with mobile devices. LIBs are currently used not only in mobile devices but also in a wide range of applications. They play an important role as a power supply because a lot of modern electrical devices do not have power cords and do not rely on fossil fuels. For example, vacuum cleaners traditionally were powered by energy from an electric outlet, but now cordless vacuum cleaners are commonplace because of the higher power and higher energy density of LIBs.

LIBs contribute to electric vehicles (EVs), their most notable application. As mentioned above, it is important to decrease CO<sub>2</sub> emissions and the use of fossil fuels, and automobiles are one of the culprits. Changing their energy source from fossil fuels to batteries is an effective way to decrease CO<sub>2</sub> emissions. An electric vehicle's cruising range is related to the capacity of its battery. Depending on the size of the car, it is possible to drive more than 500 km on a single charge of a 100 kWh battery. In the calculation, a 100 kWh battery has about 4700 cylindrical cells, each with a capacity of 21 Wh, so the EV market is expected to be huge. Volkswagen has set a goal of selling up to 3 million EVs per year in 2025 <sup>6)</sup>. Why are automakers increasing EV production by 2025? The most important factor is environmental regulations for automobiles. From 2018, such regulations became strict in Europe, the United States, and China. Since 2018, the California Air Resources Board (CARB) regulations have mandated a certain percentage of zero-emission vehicles in a manufacturer's sales volume and increased the ratio of zero-emission vehicles, as shown in Table 1-1. It has been announced that vehicles powered only by engines will be banned in Germany in 2030 and in China and France in 2040. Therefore, the production of batteries for EVs must increase.

The demand for batteries will also increase in the drone market, especially the industrial drone market. Industrial drones are used to spray agricultural pesticides, to find survivors of natural disasters and other mishaps, to inspect buildings, and so on. In Japan, attempts are being made to utilize robot technology and information and communication

technology (ICT) against the backdrop of social issues such as a declining agricultural population and an aging overall population. Figure 1-3 shows the number of registered agriculture drones and pesticide application areas using drones in Japan. The use of drones for agriculture has been increasing significantly year by year<sup>7)</sup>. The factors behind the spread of agricultural drones are their lower price, including maintenance, compared to helicopters, and their stability and ease of control. Automatic pesticide spraying and pinpoint spraying are possible in conjunction with GPS. Drones are powered by LIBs because their performance characteristics, such as high energy density and high power, are suitable for drones. However, drones require more than one battery pack; because the current drone flight time is only 20 - 30 minutes per pack, equivalent to 1 ha of pesticide spraying, a spare battery is absolutely necessary.

The demand for energy storage systems (ESS) arises not only for power plants but also for residential use. A residential ESS is desirable as an emergency power supply in the event of a disaster or power outage, or as surplus power so that solar power generated in the daytime can be used at night. Japan experiences long-term power outages due to disasters such as earthquakes and typhoons. An increasing number of people are seeking safety and security by preparing for such disasters. In Japan, a surplus power purchase system using solar power was started in 2009, but the purchase system ended in 2019 because the purchase period was 10 years. As of 2019, the number of completed purchases was 560,000, and more than 200,000 per year are expected to continue after 2020<sup>8)</sup>. Thus, both large-scale ESS and residential ESS are expected to become large battery markets.

Figure 1-4 shows the trend in LIB pack shipments based on a B3's market report<sup>8)</sup>. Note that the battery pack capacity varies widely depending on the kind of device. For example, the capacity of a battery pack for mobile phones is around 10 Wh, but that for an ESS is several MWh. Although there are no major changes in existing markets such as cellular phones and notebook PCs, it can be seen that new LIB demand in EVs, cleaners, and wearable devices is increasing.

Table 1-1. CARB regulations of the percentages of zero-emission vehicles in a manufacturer's sales volume

Model Year	Ratio of zero-emission vehicle
2018	4.5%
2019	7.0%
2020	9.5%
2021	12.0%
2022	14.5%
2023	17.0%
2024	19.5%
2025	22.0%

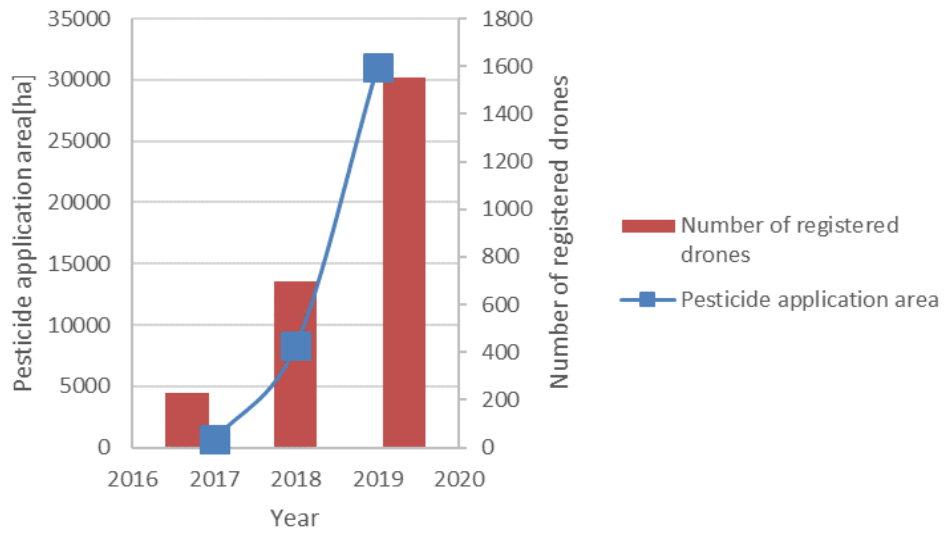


Fig. 1-3. Number of registered agriculture drones and size of pesticide application area using drones

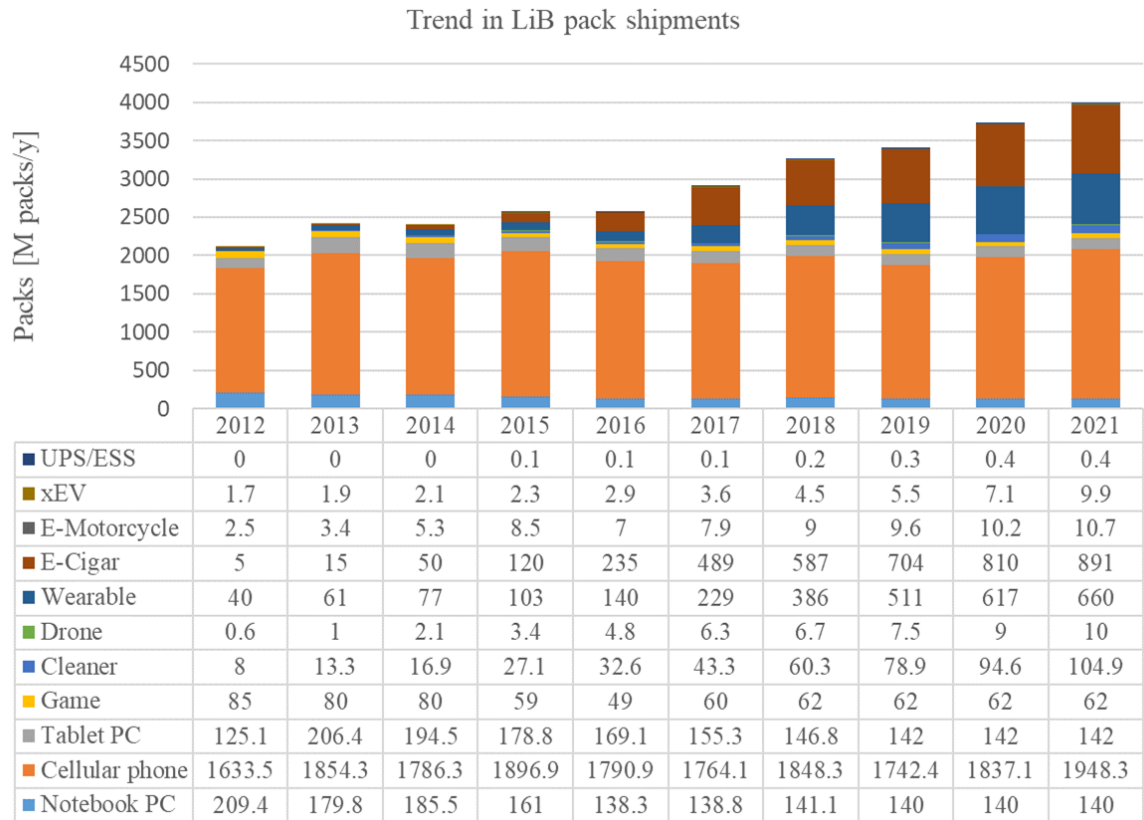


Fig. 1-4. The trend in LIB pack shipments based on B3 report published data

## 1. 2 Li ion secondary batteries

### 1. 2. 1 Structure and principle of Li ion secondary batteries

Li ion secondary batteries are composed of a cathode, an anode, a separator, and an electrolyte. Figure 1-5 shows the schematic image of a LIB. The cathode is composed of active materials, a conductive assistant, and a binder that coat Al foil as a current collector. In LIBs currently on the market, the cathode active material is the Li ion source. A typical cathode active material is  $\text{LiCoO}_2$ , which was discovered by Goodenough *et al.*<sup>10)</sup>. The cathode active materials are oxide materials, which have high electronic resistance, so the cathode needs to include a conductive assistant in the coating layer. The binder is included to bind the active material, the conductive assistant, and the current collector. In general, acetylene carbon is used as the conductive assistant and polyvinylidene fluoride (PVdF) is used as the binder for the cathode. Figure 1-6 shows a cross-sectional scanning electron microscope (SEM) image of a cathode. The upper image is the second electron image and the lower one is a reflected electron image. The large particles are cathode materials, which in this case formed secondary particles. The dark-contrast area in the reflected electron image indicates the conductive assistant and the binder. Because both of these are mainly composed of carbon, they were indistinguishable by the reflected electron image. In order to increase the packing density of cathode active materials, a mixture of large and small particles is used.

The anode is composed of anode active materials, the conductive assistant, and the binder. Graphite is widely used as an anode active material because of its high degree of safety, good productivity, and low cost. Graphite does not, of course, include lithium, so it can be used as an anode when it is combined with a lithium-containing cathode active material. Styrene-butadiene rubber is used as a binder for the anode. Cu foil is used as a current collector. Figure 1-7 shows the cross-sectional SEM images of the anode.

The electrolyte is one of the important components characterizing battery characteristics. Because the operating voltage is more than 1.5 V, an aqueous-type electrolyte could not be used. The electrolyte is an organic solvent in which lithium salt is dissolved.  $\text{LiPF}_6$  is generally used as a lithium salt. The organic solvent is a mixture of organic solvents, and the materials are ethylene carbonate (EC), propylene carbonate (PC),

diethyl carbonate (DEC), ethyl methyl carbonate (EMC), and dimethyl carbonate (DMC). Which organic solvent is used depends on the battery application and the required characteristics.

The separators are made of a compound called polyolefin and have a thickness of about 15  $\mu\text{m}$ , and a film with a small hole of 1  $\mu\text{m}$  or less on the surface is used. The materials include polyethylene (PE) and polypropylene (PP). The functions of the separator are not only to prevent electrical shorts but also to hold the electrolyte and, in case of a thermal runaway, the separator shuts down the battery system by the melting of the separator, which thus fills the small holes. Figure 1-8 shows the surface SEM image of the separator.

Although a battery is basically composed of these members, different types of LIBs are commercially available. Figure 1-9 shows three kinds of LIBs as examples. Cylindrical cells are used in a wide range of applications because of their high productivity and low cost. The capacity of cylindrical cells ranges from 2.0 to 4.0 Ah. Tesla uses 7000 cylindrical cells as a power source for its electric vehicles. Because pouch cells are superior flexibility in shape of cells, IT devices such as smartphones and tablet PCs use them. Prismatic cells are often used for batteries with relatively large capacity.

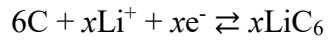
Here we describe the charge/discharge principle of LIBs. As noted before, the source of lithium is the cathode material. The charging and discharging of a lithium ion battery occurs when lithium ions move in an electrolyte solution in a separator. Lithium ions move from the cathode during charging and from the anode during discharging. The following reaction formula is a charge/discharge reaction formula of a lithium ion battery in which the cathode is made of lithium cobalt oxide ( $\text{LiCoO}_2$ ) as a cathode active material and the anode is made of graphite (C) as an anode active material. During charging, lithium ions and electrons are released from  $\text{LiCoO}_2$  and the lithium ions move in the electrolyte, after which they are inserted into graphite. Electrons travel through an external circuit, and the same amount of electrons as lithium ions move. Otherwise, electrical neutrality cannot be maintained. When discharging, the reverse reaction occurs. During discharge, lithium ions flow through the electrolyte from the anode toward the cathode, and simultaneously electrons flow through the external circuit from the cathode

toward the anode.

Cathode reaction



Anode reaction



Electrical neutrality cannot be maintained if only lithium ions come in and out. For this reason, the transition metal element compensates for charges by the oxidation-reduction reaction. In the case of  $\text{LiCoO}_2$ ,  $\text{Co}^{3+}$  is changed to  $\text{Co}^{4+}$  by moving lithium and electrons from  $\text{LiCoO}_2$  during charging.

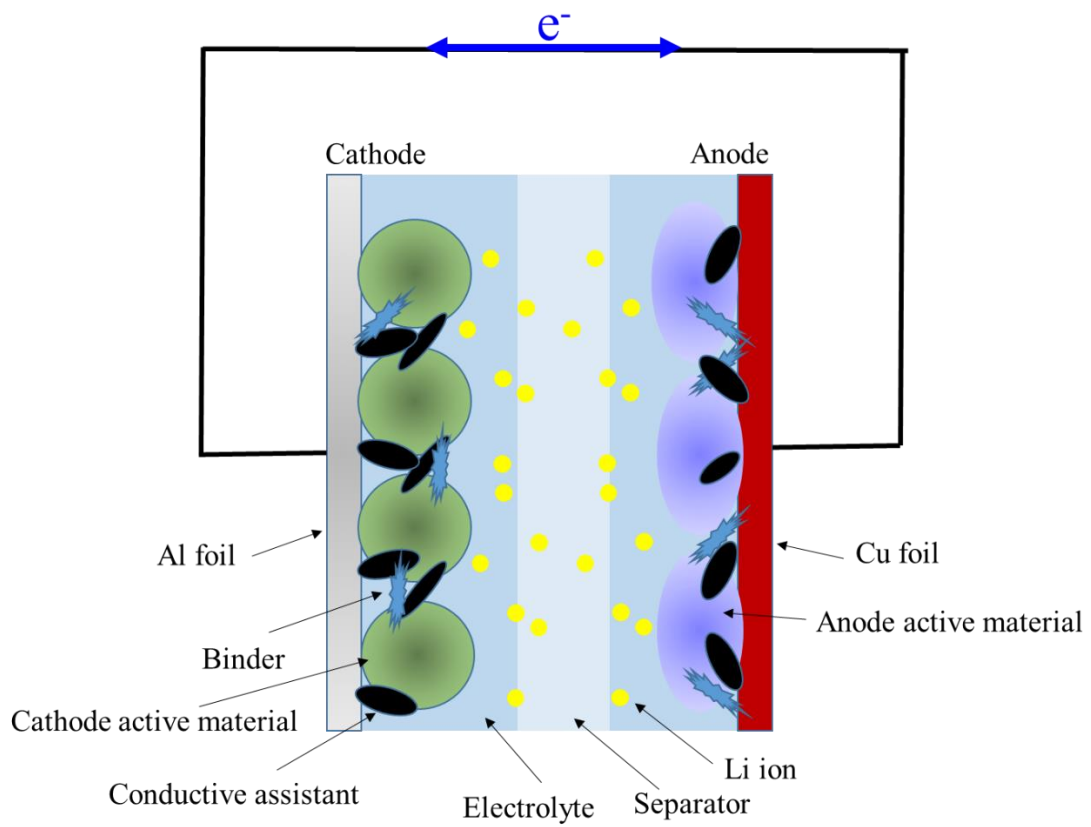


Fig. 1-5. Schematic image of Li ion secondary battery

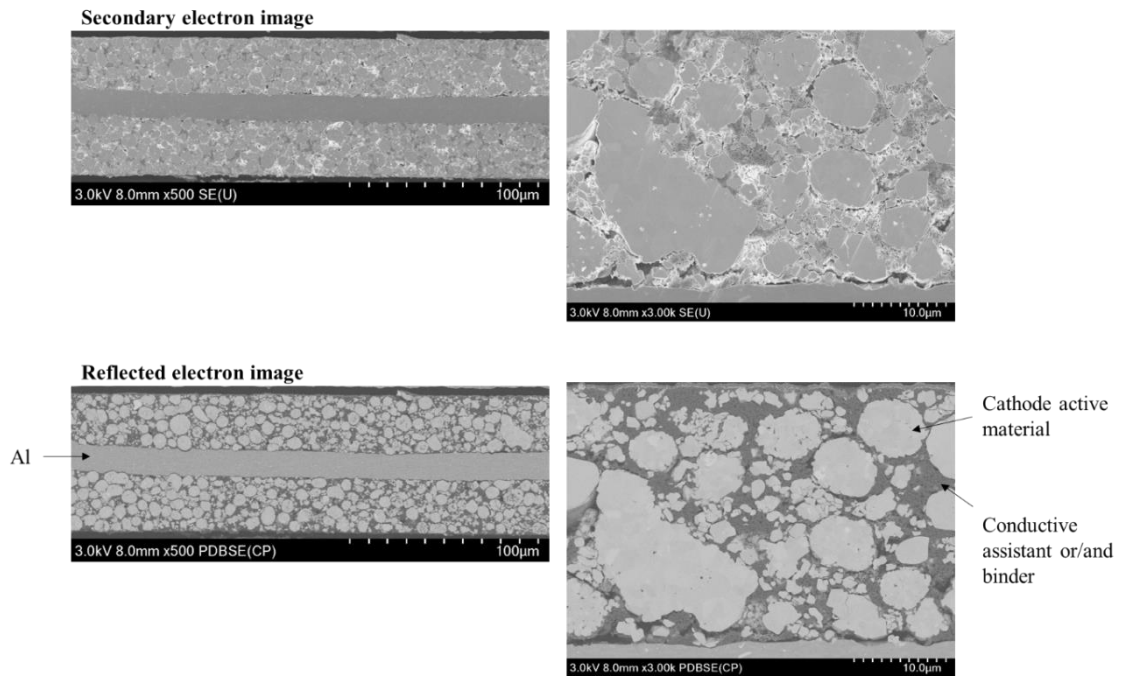


Fig. 1-6. Cross-sectional SEM images of a cathode

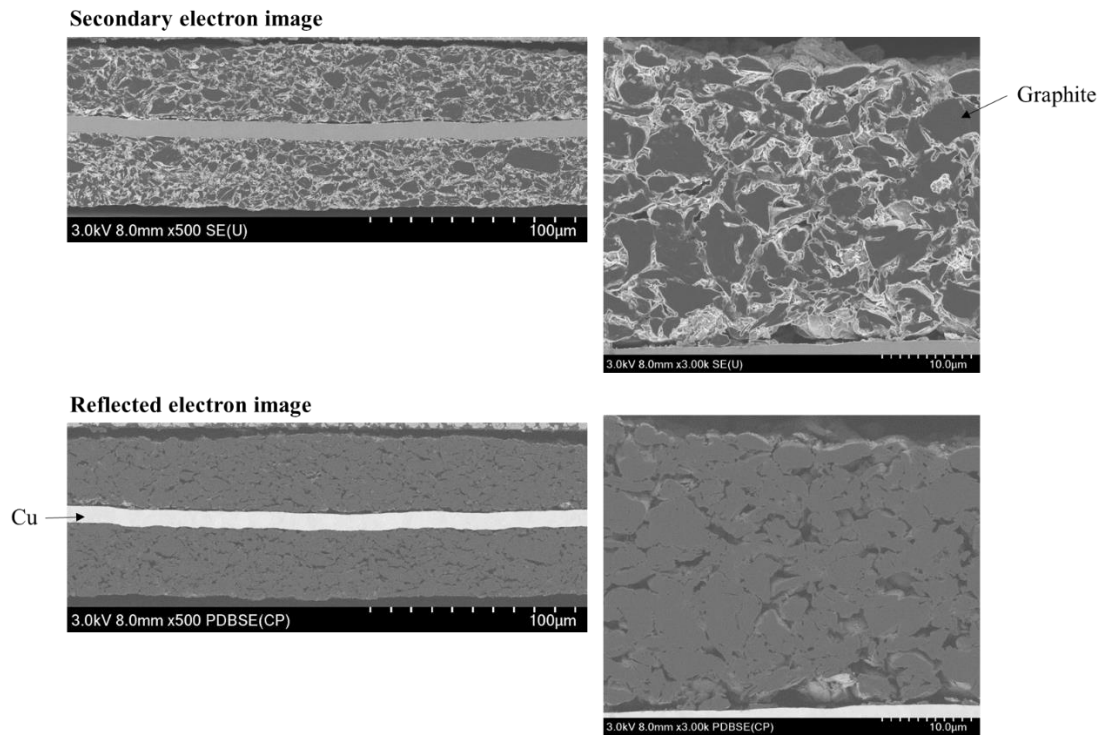


Fig. 1-7. Cross-sectional SEM images of an anode

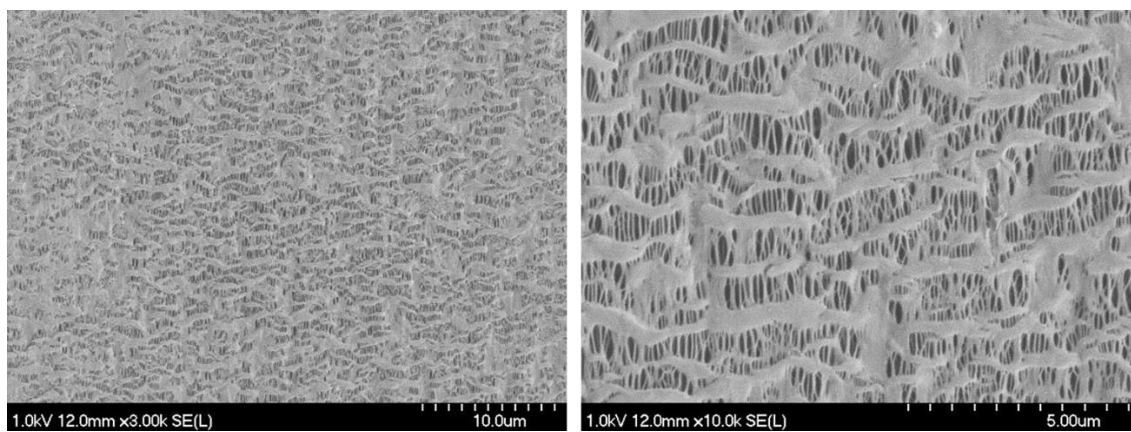


Fig. 1-8. Surface SEM images of a separator



Pouch cell

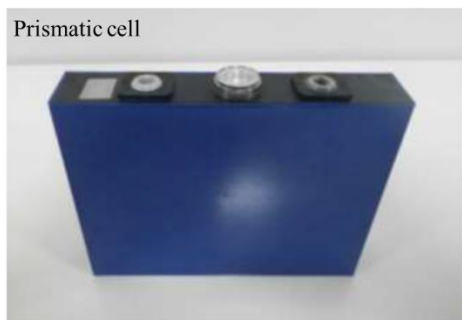


Fig. 1-9. Types of Li ion battery

### 1.2.2 Cathode materials for Li ion secondary batteries

The energy density of LIBs is deeply related to cathode active materials because the source of Li ions is a cathode active material. For a battery, it is important to pack as much active material as possible in a restricted container to increase the capacity, and both the energy density per volume and the energy density per weight of a cathode active material are important. A lot of materials have been investigated to increase the energy density of a LIB. Materials having representative structures are: layered rock salt-type  $\text{LiCoO}_2$ , spinel-type  $\text{LiMn}_2\text{O}_4$ , and olivine-type  $\text{LiFePO}_4$ .

$\text{LiCoO}_2$ <sup>10-14)</sup> and other transition metal layered rock salt structures such as  $\text{LiNi}_a\text{Co}_b\text{Mn}_c\text{O}_2$  ( $a+b+c = 1$ )<sup>15-17)</sup> are well known to have high energy density and are widely used.  $\text{LiMO}_2$  (M is a transition metal) has  $R-3m$  symmetry; Fig. 1-10 shows the crystal structure of  $\text{LiCoO}_2$ . The lithium and cobalt ions occupy alternate octahedral sites between the cubic-close-packed oxygen planes. Thus, lithium ions deintercalate and intercalate during the charging/discharging process. However, destabilization of the crystal structure promotes the deterioration of characteristics and the decline of thermal stability<sup>17-19)</sup>. During charging/discharging, as shown in Fig. 1-11, when the amount of lithium is  $x < 0.5$  in  $\text{Li}_x\text{CoO}_2$ , the phase changes irreversibly to a monoclinic structure, which greatly affects the deterioration of cycle characteristics<sup>20)</sup>. Therefore, it is difficult to use all of the lithium accommodated.

The olivine phosphate structure is known to be a stable crystal structure for LIB cathodes, because  $\text{PO}_4$  has strong covalent bonds that prevent oxygen release<sup>21-23)</sup>. Among such as the phosphate cathode active materials, lithium iron phosphate ( $\text{LiFePO}_4$ ) having an olivine structure as reported by Padhi *et al.* in 1997, has a high charge/discharge voltage of about 3.4 V (vs.  $\text{Li}/\text{Li}^+$ ), and its theoretical capacity is 170 mAh/g, comparable to that of  $\text{LiCoO}_2$ . The space group of  $\text{LiFePO}_4$  is  $Pnma$ , and Fig. 1-12 shows the crystal structure of  $\text{LiFePO}_4$ .  $\text{LiFePO}_4$  shares one edge of  $\text{PO}_4$  tetrahedra with  $\text{FeO}_6$  octahedra. Compared with a layered rock salt-type active material, oxygen release from an active material is less likely to occur, and since it has high structural stability in the charged state, it is attracting attention for its high degree of safety. However, a characteristic of polyanion phosphate materials in general is that their electrical conductivity is remarkably

low. The value of electrical conductivity is  $10^{-3}$  S/cm for  $\text{LiCoO}_2$  but falls to  $10^{-8}$  S/cm for  $\text{LiFePO}_4$  <sup>24</sup>). Various improvement methods have been studied to improve this extremely low electrical conductivity, such as covering the surface of the active material with a conductive material, adding a highly conductive material <sup>25, 26</sup>), and improving the electrical conductivity of the active material itself by substituting different elements into the crystal lattice <sup>27</sup>).

As materials with higher energy density than  $\text{LiFePO}_4$ , lithium manganese phosphate ( $\text{LiMnPO}_4$ ), lithium cobalt phosphate ( $\text{LiCoPO}_4$ ), and lithium nickel phosphate ( $\text{LiNiPO}_4$ ) have been also actively studied <sup>28, 29</sup>).  $\text{LiMnPO}_4$  cannot obtain sufficient charge/discharge characteristics due to the valence change of divalent manganese to unstable trivalent manganese with lithium deintercalation.  $\text{LiCoPO}_4$  has a high charge/discharge voltage and has not been as good as  $\text{LiFePO}_4$  due to problems such as decomposition of the electrolyte. The capacity of  $\text{LiNiPO}_4$  has not been confirmed in charging/discharging up to 5 V, and nickel oxidation/reduction occurs at a potential of 5 V or higher. Therefore,  $\text{LiNiPO}_4$  is considered to be less practical than  $\text{LiCoPO}_4$ .

$\text{Li}_3\text{V}_2(\text{PO}_4)_3$ , with a NASICON structure that uses vanadium as transition metal, has been studied as a polyanion compound without an olivine structure <sup>30, 31</sup>).  $\text{Li}_3\text{V}_2(\text{PO}_4)_3$  is capable of charge compensation by  $\text{V}^{3+}/\text{V}^{4+}$  oxidation-reduction of vanadium, and lithium deintercalation is possible. However, the occupation ratio by the polyanion in the structure is high and the usable capacity is about 130 mAh/g. This is the capacity of two Li reactions with respect to the theoretical capacity of 196 mAh/g, and is low with respect to  $\text{LiFePO}_4$ .

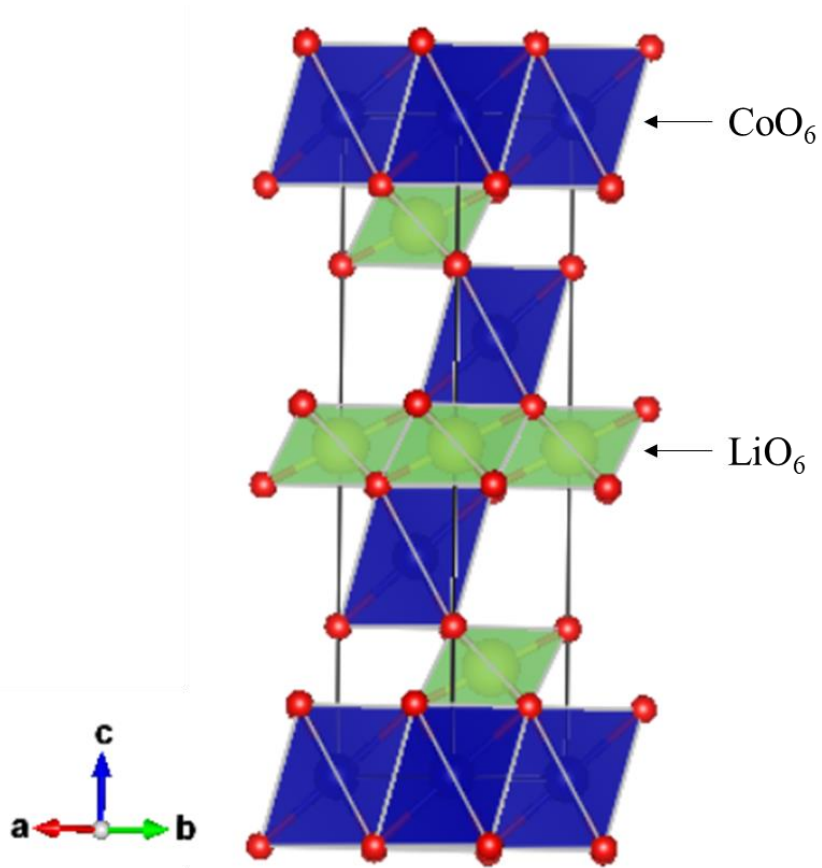


Fig. 1-10. Crystal structure of  $\text{LiCoO}_2$

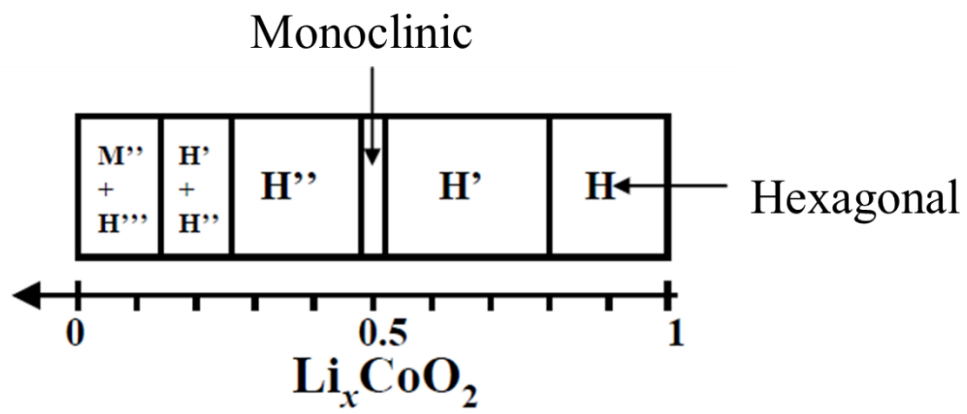


Fig. 1-11. Structural change of  $\text{LiCoO}_2$  with lithium content

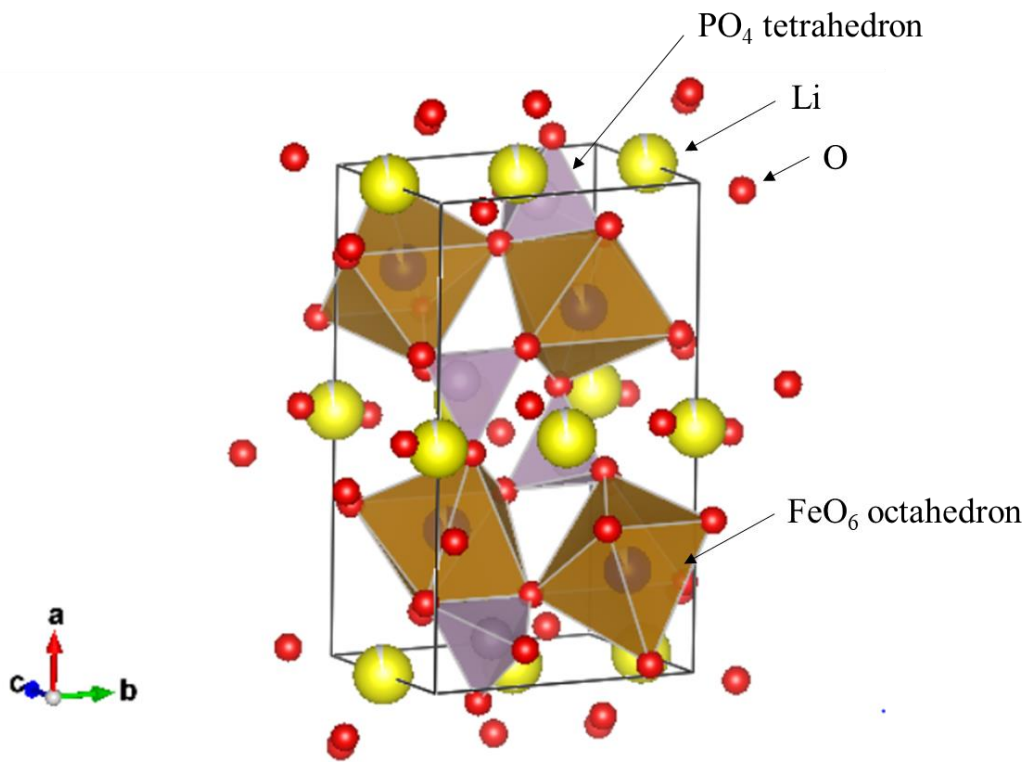


Fig. 1-12. Crystal structure of  $\text{LiFePO}_4$

### 1. 3 LiVOPO<sub>4</sub> background

LIBs have a high energy density and have been used in a wide range of applications, but there are failures due to battery swelling and fire/smoke incidents. Therefore, to satisfy market demand, both high energy density and high safety are required. Various factors lead to battery incidents, but the root cause is thought to be the thermal runaway of the cathode in the case of a short circuit, as shown in Fig. 1-13. In other words, the risk of an incident can be reduced by increasing the thermal stability of the cathode active material. As mentioned above, polyanion cathode materials have high thermal stability at the charging state because PO<sub>4</sub> has strong covalent bonds that prevent oxygen release. In particular, LiFePO<sub>4</sub> is expected to be a high-safety, long-life active cathode material. It has a flat operating voltage of 3.45 V and can use all accommodated Li. LiVOPO<sub>4</sub> has three types of crystal structure:  $\alpha_1$ -LiVOPO<sub>4</sub> (tetragonal phase; space group is *P4/nmm*)<sup>32-34</sup>,  $\beta$ -LiVOPO<sub>4</sub> (orthorhombic phase; space group is *Pnma*)<sup>35-38</sup>, and  $\alpha$ -LiVOPO<sub>4</sub> (triclinic phase; some reports describe it as  $\epsilon$ -LiVOPO<sub>4</sub>; space group is *P-1*)<sup>39-44</sup>. Its theoretical specific capacity is 159 mAh/g. Each crystal structure is shown in Fig. 1-14. Although the theoretical capacity of LiVOPO<sub>4</sub> is slightly lower than that of LiFePO<sub>4</sub>, the operating voltage of all LiVOPO<sub>4</sub> is 3.9 V; thus, LiVOPO<sub>4</sub> (618 Wh/kg) has a higher energy density than LiFePO<sub>4</sub> (587 Wh/kg). Therefore, LiVOPO<sub>4</sub> is expected to be a high-energy-density and high-safety cathode material.

Research on LiVOPO<sub>4</sub> began in 1999 with a report by Gaubicher *et al.*<sup>45</sup>). They investigated new host materials where transition elements are surrounded by O<sup>2-</sup> and (XO<sub>4</sub>)<sup>n-</sup> (X = S, P, As) and brought attention to LiVOPO<sub>4</sub> systems. In their study, the orthorhombic  $\beta$ -VOSO<sub>4</sub> with space group *Pnma* had good electrochemical behavior at 2.8 V with V<sup>4+</sup>/V<sup>3+</sup> couples<sup>46</sup>). In the crystal structure of  $\beta$ -VOSO<sub>4</sub>, VO<sub>6</sub> octahedra are connected by opposite corners to form chains along the a-axis. These polyhedra are twisted by pair along the c-axis and connected by SO<sub>4</sub> tetrahedra via corner sharing. Each sulfate group is linked along the b-axis to two other chains of VO<sub>6</sub> octahedra. Lithium cations can move in this open three-dimensional network with a corner-sharing chain. Because  $\beta$ -VOPO<sub>4</sub> is isostructural with  $\beta$ -VOSO<sub>4</sub><sup>47</sup>) and it operates on the V<sup>5+</sup>/V<sup>4+</sup> couples in charging/discharging, a  $\beta$ -VOPO<sub>4</sub> system can operate at a higher

charge/discharge voltage.

VOPO<sub>4</sub> has seven types of crystal structure that differ in the connection and arrangement of VO<sub>6</sub> octahedral and PO<sub>4</sub> tetrahedral units<sup>48-51</sup>). The electrochemical properties of each type of VOPO<sub>4</sub> were examined<sup>45, 52-55</sup>). Although the operating voltage of each phase of VOPO<sub>4</sub> was high enough to adapt to LIBs, the exhibited capacity was much smaller than the theoretical capacity. Even if the same method is used for preparation, the charge/discharge profile may be completely different<sup>45, 55</sup>). There is a possibility that the synthesis method affected the electrochemical properties.

VOPO<sub>4</sub> exhibits higher voltage than LiFePO<sub>4</sub> and comparable capacity to LiFePO<sub>4</sub>. However, VOPO<sub>4</sub> does not include lithium, so it cannot be used as a cathode for LIBs in combination with graphite anode. It needs lithiation other than that provided by electrochemical methods. Various synthesis methods have been reported for the production of LiVOPO<sub>4</sub>. Barker *et al.* reported a carbothermal reduction approach for making β-LiVOPO<sub>4</sub> and achieved 134 mAh/g at C/50 rate<sup>35</sup>). Azmi *et al.* prepared β-LiVOPO<sub>4</sub> using an impregnation method together with a ball milling process and obtained 123 mAh/g at C/40 rate<sup>36</sup>). Ren *et al.* proposed a sol-gel method for β-LiVOPO<sub>4</sub> production<sup>37</sup>). A microwave sintering method for α-LiVOPO<sub>4</sub> was demonstrated by Wang *et al.* and showed 154 mAh/g after 22 cycles<sup>38</sup>). Hameed *et al.* obtained 103 mAh/g of α<sub>1</sub>-LiVOPO<sub>4</sub> via LiVOPO<sub>4</sub>·2H<sub>2</sub>O<sup>33</sup>). These methods were suitable only for the synthesis of one crystal phase. Although Harrison and Manthiram reported making each crystal phase using a microwave-assisted solvothermal method, it was necessary to change the ratio of solvent and precursor to form different phases<sup>56</sup>). While these reports affirm the potential of LiVOPO<sub>4</sub> as a next-generation cathode material, it is difficult to determine which phase is most suitable for LIBs. In addition, these reports indicated only around half of the theoretical capacity even at a 1 C discharge rate. This was attributed to poor electrical conductivity and low lithium ionic diffusivity. However, because the crystal structures differ, the optimum particle size is also considered to differ. The reported capacity of LiVOPO<sub>4</sub> is shown in Fig. 1-15.

LiVOPO<sub>4</sub> and Li<sub>3</sub>V<sub>2</sub>(PO<sub>4</sub>)<sub>3</sub> are also attracting attention as multi-electron cathode active materials. Rui *et al.* reported the characteristics of Li<sub>3</sub>V<sub>2</sub>(PO<sub>4</sub>)<sub>3</sub> as an anode and showed

that Li intercalated stepwise between 2.0 V and 1.6 V and was about 130 mAh /g; however, its energy density is too low for it to be useful as an anode active material <sup>57)</sup>. On the other hand, LiVOPO<sub>4</sub> exhibited good electrochemical performance by the use of both the V<sup>3+</sup>/V<sup>4+</sup> and V<sup>4+</sup>/V<sup>5+</sup> redox couples. The crystal structure evolution from LiVOPO<sub>4</sub> to Li<sub>2</sub>VOPO<sub>4</sub> in relation to α<sub>1</sub>-LiVOPO<sub>4</sub> <sup>33)</sup>, β-LiVOPO<sub>4</sub> <sup>56, 58)</sup>, and α-LiVOPO<sub>4</sub> <sup>59, 60)</sup> has been studied, but the discharge voltages were 1.5 V in all cases, so it is hard to discuss the possibility of the valence of vanadium becoming less than a trivalent state and generating a larger capacity.

Although LiVOPO<sub>4</sub> is expected to have high thermal stability because it consists of PO<sub>4</sub>, no report has actually evaluated this. In particular, the crystal structure of a low-voltage region such as Li<sub>2</sub>VOPO<sub>4</sub> may be unstable because of the electrochemically lithiated insertion of Li.

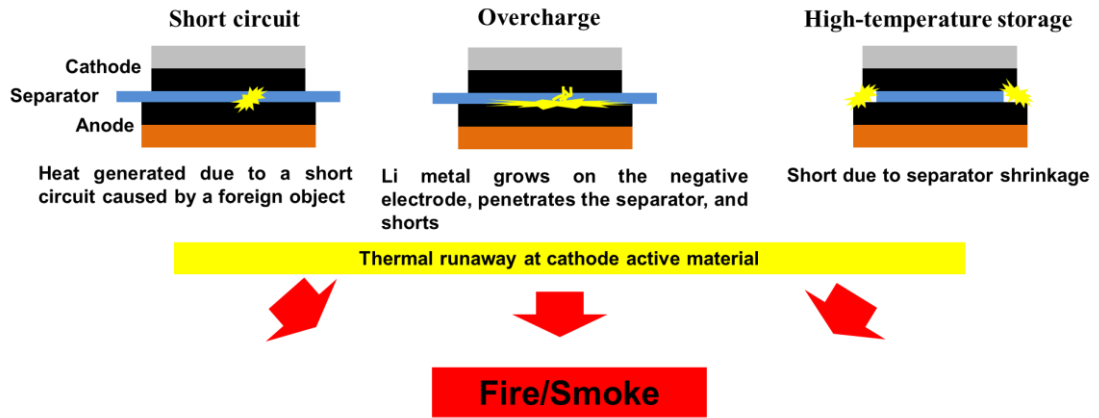


Fig. 1-13. Root cause of fire/smoke incident

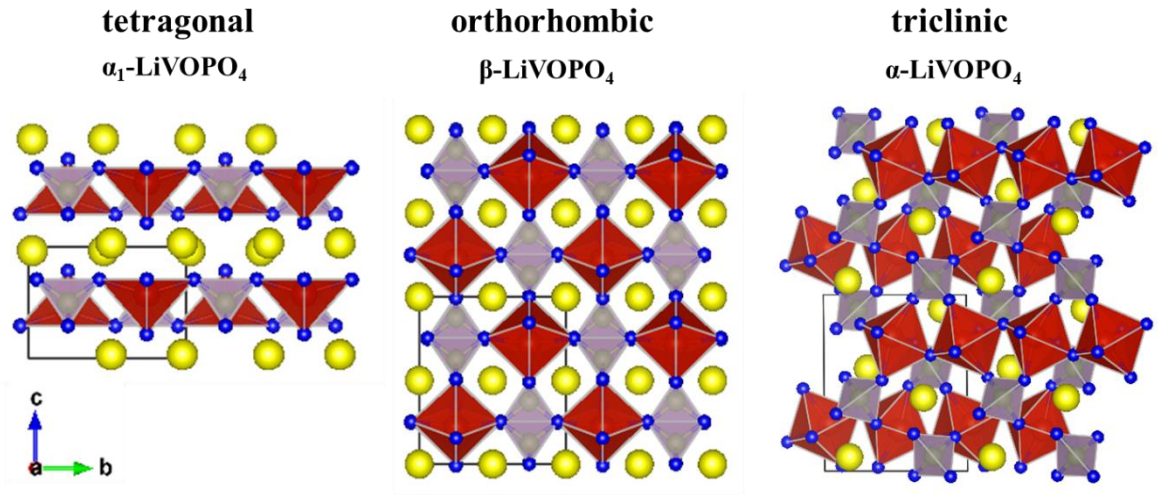


Fig. 1-14. Crystal structures of three types of LiVOPO<sub>4</sub>

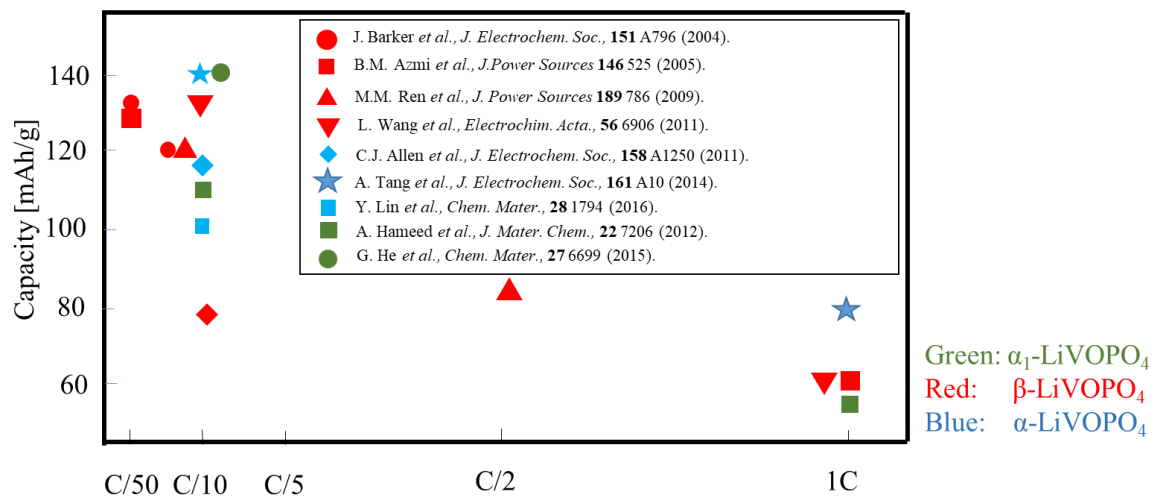


Fig. 1-15. The reported capacities of LiVOPO<sub>4</sub>

#### **1. 4 Objectives of this study**

On the basis of previous reports about  $\text{LiVOPO}_4$ , we can say that it could serve as a next-generation polyanion cathode material, but several challenges to replace  $\text{LiFePO}_4$  with  $\text{LiVOPO}_4$  must first be resolved, including:

- 1) A synthesis method with excellent mass productivity must be developed.
- 2) The capacity must match the theoretical capacity.
- 3) The capacity at high C rate must be improved.

$\text{LiVOPO}_4$  is also very interesting as a research material with regard to the following aspects:

- 1) Relationship between electrochemical property and crystal structure.
- 2) Crystal evolution during charging/discharging.
- 3) Thermal stability in the low-voltage region.

The purposes of this study are to develop a method of synthesizing  $\text{LiVOPO}_4$  to achieve the theoretical capacity and to improve the high C rate performance while considering mass productivity, as well as to clarify the relationship between electrochemical properties and crystal structure. In addition, the thermal stability of fully charged and Li-excess states is evaluated to clarify the thermal stability of  $\text{LiVOPO}_4$ . Based on our results, we determine which crystal phase is the best cathode active material for the battery.

## Reference

- 1 Central Research Institute of Electric Power, *General Technical Report*, **Y06** (2016).
- 2 Agency for Natural Resources and Energy, *Energy White Paper*, Chapter 1 (2019).
- 3 Ministry of the Environment, *Proposals for Low-carbon Energy to Create a Low-carbon Society* (2012).
- 4 Agency for Natural Resources and Energy, *Energy White Paper*, Chapter 2 (2019).
- 5 Agency for Natural Resources and Energy, *Energy-related Technology Roadmap* (2014).
- 6 Nikkei BP, *The Next Generation of Battery Technologies* (2019).
- 7 Ministry of Agriculture, Forestry and Fisheries, *Aircraft Implementation Report* (2019).
- 8 Nikkei Electronics, 7 (2018).
- 9 B3 report 19-20, Chapter 3 (2019).
- 10 K. Mizushima, P.C. Jones, P.J. Wiseman, and J.B. Goodenough, *Mater. Res. Bull.*, **15** 783 (1980).
- 11 J. Cho and G. Kim, *Electrochem. Solid-State Lett.*, **2** 253 (1999).
- 12 R. Koksang, J. Barker, H. Shi, and M.Y. Saidi, *Solid State Ionics*, **84** 1 (1996).
- 13 M. Broussely, P. Biensan, and B. Simon, *Electrochem. Acta.*, **45** 3 (1999).
- 14 G.G. Amatucci, J.M. Tarascon, and L.C. Klein, *J. Electrochem. Soc.*, **143** 1114 (1996).
- 15 M.H. Kima, H.S. Shin, D. Shin, and Y.K. Sun, *J. Power Sources*, **159** 1328 (2006).
- 16 J. Cho, H. Jung, Y. Park, G. Kim, and H. Lim, *J. Electrochem. Soc.*, **147** 15 (2000).
- 17 Y. Gao, M.V. Yakovleva, and W.B. Ebner, *Electrochem. Solid State Lett.*, **1** 117 (1998).
- 18 J.R. Dahn, E.W. Fuller, M. Obrovac, and U.V. Sacken, *Solid State Ionics*, **69** 265 (1994).
- 19 Y. Baba, S. Okada, and J. Yamaki, *Solid State Ionics*, **148** 311 (2002).
- 20 G.G. Amatucci, J.M. Tarascon, and L.C. Klein, *J. Electrochem. Soc.*, **143** 1114 (1996).
- 21 A.K. Padhi, K.S. Nanjundaswamy, and J.B. Goodenough, *J. Electrochem. Soc.*, **144** 1188 (1997).
- 22 A.K. Padhi, K.S. Nanjundaswamy, C. Masquelier, S. Okada, and J.B. Goodenough, *J. Electrochem. Soc.*, **144** 1609 (1997).

- 23 G. Li, H. Azuma, and M. Tohda, *J. Electrochem. Soc.*, **148** A960 (2001).
- 24 S.Y. Chung, J.T. Bloking, and Y.M. Chiang, *Nat. Mater.*, **2** 123 (2002).
- 25 P.S. Herle, B. Ellis, N. Coombs, and L.F. Nazar, *Nat. Mater.*, **3** 147 (2004).
- 26 A.A. Salah, A. Mauger, K. Zaghib, J.B. Goodenough, N. Ravet, M. Gauthier, F. Gendron, and C.M. Julien, *J. Electrochem. Soc.*, **153** A1692 (2006).
- 27 C. Delacourt, C. Wurm, L. Laffont, J.B. Leriche, and C. Masquelier, *Solid State Ionics*, **177** 333 (2006).
- 28 H.H. Li, J. Jin, J.P. Wei, Z. Zhou, and J. Yan, *Electrochem. Comm.* **11** 95 (2009).
- 29 F. Zhou, M. Cococcioni, C.A. Maroametti, D. Morgan, and G. Ceder, *Phys. Rev. B*, **70** 235121 (2004).
- 30 M.Y. Saidi, J. Barker, H. Huang, J.L. Swoyer, and G. Adamson, *J. Power Sources*, **119-121** 266 (2003).
- 31 H. Huang, S.C. Yin, T. Kerr, N. Taylor, and L.F. Nazar, *Adv. Mater.*, **14** 1525 (2002).
- 32 N. Dupre, G. Wallez, J. Gaubicher, and M. Quarton, *J. Solid State Chem.*, **117** 2896 (2004).
- 33 G. He, C.A. Bridges, and A. Manthiram, *Chem. Mater.*, **27** 6699 (2015).
- 34 A.S. Hameed, M. Nagarathinam, M.V. Reddy, B.V.R. Chowdan, and J.J. Vittal, *J. Mater. Chem.*, **22** 7206 (2012).
- 35 J. Barker, M.Y. Sadi, and J.L. Swoyer, *J. Electrochem. Soc.*, **151** A796 (2004).
- 36 B.M. Azmi, T. Ishihara, H. Nishiguchi, and Y. Takita, *J. Power Sources*, **146** 525 (2005).
- 37 M.M. Ren, Z. Zhou, L.W. Su, and X.P. Gao, *J. Power Sources*, **189** 786 (2009).
- 38 L. Wang, L. Yang, L. Gong, X. Jiang, K. Yuan, and Z. Hu, *Electrochim. Acta*, **56** 6906 (2011).
- 39 Y. Yang, H. Fang, J. Zheng, L. Li, G. Li, and G. Yan, *Solid State Sci.*, **10** 1292 (2008).
- 40 A. Tang, J. Shen, Y. Hu, G. Xu, D. He, Q. Yi, and R. Peng, *J. Electrochem. Soc.*, **161** A10 (2014).
- 41 N.F. Quackenbush, L. Wangoh, D.O. Scanlon, R. Zhang, Y. Chung, Z. Chen, B. Wen, Y. Lin, J.C. Woicik, N.A. Chernova, S.P. Ong, M.S. Whittingham, and L.F.J. Piper, *Chem. Mater.*, **27** 8211 (2015).

- 42 Y. Lin, B. Wen, K.M. Wiaderek, S. Sallis, H. Liu, S.H. Lapidus, O.J. Chupas, L.F.J. Piper, M.S. Whittingham, K.W. Chapman, and S.P. Ong, *Chem. Mater.*, **28** 1794 (2016).
- 43 Z. Liu, Z. Su, and H. Tian, *Ceram. Int.*, **44** 9372 (2018).
- 44 K. Saravanan, H.S. Lee, M. Kuezma, J.J. Vittal, and P. Balaya, *J. Mater. Chem.*, **21** 10042 (2011).
- 45 J. Gaubicher, T.L. Mercier, Y. Chabre, J. Angenault, and M. Quartona, *J. Electrochem. Soc.*, **146** 4375 (1999).
- 46 J. Gaubicher, Y. Chabre, J. Angenault, A. Lauti, and M. Quarton, *J. Alloys Compd.*, **262-263** 34 (1997).
- 47 R. Gopal and C. Calvo, *J. Solid State Chem.*, **5** 432 (1972).
- 48 E. Bordes, *Catal. Today* **1** 499 (1987).
- 49 E. Benabdelouahad, J.C. Volta, and R. Olier, *J. Catal.* **148** 334 (1994).
- 50 P. Amoros, M.D. Marcos, M. Roca, J. Alamo, A. Beltran-Porter, and D.B. Porter, *J. Phys. Chem. Solids*, **62** 1393 (2001).
- 51 S.C. Lim, J.T. Vaughey, W.T.A. Harrison, L.L. Dussack, A.J. Jacobson, and J.W. Johnson, *Solid State Ionics* **84** 219 (1996).
- 52 T.A. Kerr, J. Gaubicher, and L.F. Nazar, *Electrochem. Solid State Lett.* **3** 460 (2000).
- 53 N. Dupre, J. Gaubicher, T. Le Mercier, G. Wallez, J. Angenault, and M. Quarton, *Solid State Ionics* **140** 209 (2001).
- 54 N. Dupre, J. Gaubicher, J. Angenault, G. Wallez, and M. Quarton, *J. Power Sources* **97-98** 532 (2001).
- 55 B.M. Azmia, T. Ishihara, H. Nishiguchi, and Y. Takita, *J. Power Sources* **119-121** 273 (2001).
- 56 K.L. Harrison and A. Manthiram, *Chem. Mater.*, **25** 1751 (2013).
- 57 X.H. Rui, N. Yesibolati, and C.H. Chen, *J. Power Sources*, **199** 2279 (2011).
- 58 C.J. Allen, Q. Jia, C.N. Chinnsamy, S. Mukerjee, and K.M. Abraham, *J. Electrochem. Soc.*, **158** A1250 (2011).
- 59 M. Bianchini, J.M. Ateba-Mba, P. Dagault, E. Bogdan, D. Carlier, E. Suard, C. Masquelierade, and L. Croguennec, *J. Mater. Chem. A*, **2** 10182 (2014).

60 Y.C. Lin, B. Wen, K.M. Wiaderek, S. Sallis, H. Liu, S.H. Lapidus, O.J. Borkiericz, N.F. Quachenbush, N. A. Chernova, K. Karki, F. Omenya, P.J. Chupas, L.F. J. Piper, M.S. Whittingham, K.W. Chapman, and S.P. Ong, *Chem. Mater.*, **28** 1794 (2016).

# Chapter 2

## **Evaluation of $\text{LiVOPO}_4$**

### **Synthesized by Hydrothermal**

### **Method**

## 2.1 Introduction

As mentioned in chapter 1, various synthetic methods have been reported for the production of  $\text{LiVOPO}_4$ <sup>1-6)</sup>. These previously reported methods were only suitable for the synthesis of one crystal phase. Therefore, it is difficult to discuss which phase is most suitable for LIB. In addition, these reports are suffering from rate property. This was attributed to poor electric conductivity and low lithium ionic diffusivity. However, because the crystal structures are different, the optimum particle size is also considered to be different. For direct comparison of crystal structure and electrochemical properties, it is suitable to compare those made by the same synthetic method and process.

There are many kinds of method to synthesize materials, but considering the mass productivity and uniformity, the hydrothermal synthesis method is considered optimal, and the optimization of  $\text{LiVOPO}_4$  was studied based on the hydrothermal synthesis method. A chemical reaction involving water as a solvent under high-temperature and high-pressure reaction conditions of 100 °C or higher and 1 atm or higher is called hydrothermal reaction. A method of synthesizing substances using this hydrothermal reaction is called hydrothermal synthesis. A pressure vessel that holds high-temperature and high-pressure water is used, and this pressure vessel is called an autoclave. By using a pump of a raw material aqueous solution at room temperature, it is possible to continuously inject the apparatus into a high-temperature part and hydrothermally synthesize, which is called a continuous hydrothermal synthesis method. In the case of a continuous type, mass production is possible, and a continuous type apparatus is often used for industrial production.

In this chapter, we report a method for synthesizing the three phases of  $\text{LiVOPO}_4$  from the same precursor simply by controlling the temperature at the sintering process. Furthermore, we evaluate the electrochemical characteristics associated with the particle state in each phase.

## 2. 2 Experimental

### 2. 2. 1 Synthesize for LiVOPO<sub>4</sub>

The three crystal phases,  $\alpha_1$ -,  $\beta$ -, and  $\alpha$ -LiVOPO<sub>4</sub>, were obtained from a precursor prepared by a hydrothermal method. In a 500 ml flask, a mixture of 0.2 mol H<sub>3</sub>PO<sub>4</sub> (Nacalai Tesque first grade, purity 85%) and 180 ml deionized water were stirred with a magnetic stirrer (M-20G; Koike Precision Instruments). Subsequently, 0.1 mol of V<sub>2</sub>O<sub>5</sub> (99% Nacalai Tesque special grade) was added, and stirring was continued for 2.5 h. 0.05 mol of N<sub>2</sub>H<sub>4</sub>·H<sub>2</sub>O (98% Nacalai Tesque guaranteed reagent) was then added as a reducing agent, and stirring was continued for about 1 h. Finally, 0.1 mol of LiOH·H<sub>2</sub>O (99% Nacalai Tesque special grade) was added over about 10 min. The mixed solution was transferred to a glass cylinder, which was then placed in an autoclave (Taiatsu Techno Corp.) for hydrothermal treatment. Figure 2-1 shows the autoclave. It was heated to 250 °C at 1 °C/min, and held for 10 h after the heater was turned on. When heating was completed, the heater was turned off and the solution was cooled to 40 °C. Following the hydrothermal process, the precursor was obtained by heating the solution at 90 °C for 24 h in an oven, and then pulverizing it in a mortar. The obtained powder was placed in an alumina crucible and sintered under airflow from room temperature to 350 °C in 4 h for  $\alpha_1$ -LiVOPO<sub>4</sub>, 550 °C in 4 h for  $\beta$ -LiVOPO<sub>4</sub>, and 750 °C in 4 h for  $\alpha$ -LiVOPO<sub>4</sub>. Figure 2-2 shows the procedure of the synthesis for LiVOPO<sub>4</sub>.



Fig.2-1. Autoclave (Taiatsu Techno Corp.)

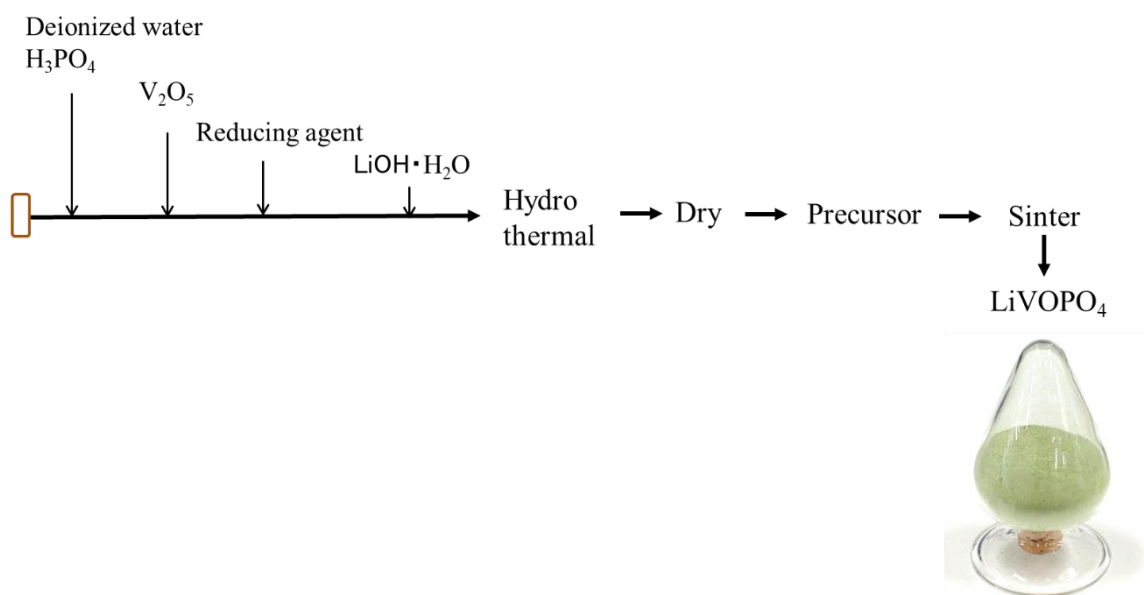


Fig.2-2. Procedure of synthesis for  $LiVOPO_4$ .

### 2.2.2 Electrode and half-cell fabrication, and evaluation method

Each  $\text{LiVOPO}_4$  was mixed with acetylene black at a weight ratio of 91:9, and 4 g of the composite powder was milled with  $\text{ZrO}_2$  balls (3 mm $\phi$  in diameter) using a planetary ball mill (PM-200, Retsch GmbH) at 550 rpm for 3 min. The composite powder and polyvinylidene fluoride (PVdF) at a weight ratio of 92:8 was dissolved into N-methylpyrrolidone (NMP) to yield a cathode coating liquid. The cathode, formed from around 7 mg/cm<sup>2</sup> cathode active material on Al foil, was obtained by following procedure. The coating liquid was applied to an Al foil by doctor blading and dried at 120 °C for 3 h, then pressed at 0.6 MPa. The cathode was then punched into a disc with an active area of about 1.13 cm<sup>2</sup>.

Electrochemical property was measured using Al laminate-type cells, consisting of the as-prepared cathode, and Li metal on Cu foil as an anode and separator (2400, Celgard, LLC.). Cells were assembled in a dry room in which the dew point was -40 °C, and in order to remove the influence of moisture mixing, it was dried for 12 h at 80 °C in a vacuum environment before injecting the electrolyte. 1 M of  $\text{LiPF}_6$  in a solution of ethylene carbonate (EC) and diethyl carbonate (DEC; volume ratio of EC:DEC = 3:7) was used as an electrolyte. Charge/discharge cycle testing was performed between 2.8 and 4.3 V at room temperature by a battery charge/discharge system (SM-8, Hokuto Denko Corp.).

### 2. 2. 3 Analysis method

Each phase of  $\text{LiVOPO}_4$  was characterized by powder X-ray diffraction (XRD). XRD patterns of each sample and *in-situ* X-ray diffractometry from 30 °C to 750 °C in 30 °C-steps under air were performed using a diffractometer (Ultima IV, Rigaku Corp.) with  $\text{Cu K}\alpha_1$  radiation ( $\lambda = 0.15418$  nm). Structural refinement of  $\text{LiVOPO}_4$  from the XRD pattern was accomplished using the Rietveld method (RIETAN-FP<sup>7</sup>). After a ball-milling process, these particles were observed by a scanning electron microscope (SEM) model SU8000 (Hitachi High-Technologies Corp.) at 5.0 kV. The morphology of each  $\text{LiVOPO}_4$  in the cathode was observed using a scanning transmission electron microscope (STEM) model JEOL 2100F at 200 keV. Amount of Li remaining after charging was estimated by electron energy loss spectroscopy (EELS), which is an application of STEM. Cathode samples for STEM, extracted from disassembled cells in a glove box and washed with DEC after 4.3 V constant current constant voltage (CC-CV) charge at rate of C/10 and C/50 cutoff (1 C = 1.03 mA/cm<sup>2</sup>), were prepared using the focused ion beam method (SMI 3050 TB, Seiko Instruments Inc.). Elemental maps of Li were reconstructed by extracted Li signal from EELS spectrum imaging.

## 2.3 Results and Discussion

### 2.3.1 Evaluation of phase transition by *in-situ* heating XRD

The phase transition during the sintering process from the precursor was investigated using *in-situ* heating XRD to determine optimal sintering conditions. Figure 2-3 shows the results of *in-situ* heating XRD from 30–750 °C in 30 °C-steps. The results of the XRD pattern at 30 °C reveals that the precursor is a composite of  $\text{LiVOPO}_4 \cdot 2\text{H}_2\text{O}$  and  $\alpha_1\text{-LiVOPO}_4$ . Reduction of the hydrate occurred at around 100 °C, and the precursor was changed to  $\alpha_1\text{-LiVOPO}_4$ . Since the intensity of the diffraction peaks of  $\alpha_1\text{-LiVOPO}_4$  increase with an increase in temperature, the crystallinity of  $\alpha_1\text{-LiVOPO}_4$  also increases.  $\alpha\text{-LiVOPO}_4$  and  $\beta\text{-LiVOPO}_4$  phases appeared between 420 °C and 510 °C, and the  $\alpha_1\text{-LiVOPO}_4$  phase disappeared. The single crystal phase of  $\beta\text{-LiVOPO}_4$  appeared in the range of 540–630 °C, and the single crystal phase of  $\alpha\text{-LiVOPO}_4$  phase appeared over 720 °C. Alterations below 420 °C were similar to those in previous reports <sup>1, 6)</sup>, but were different above 420 °C. Although the sintering environment is different,  $\alpha_1\text{-LiVOPO}_4$  was changed to  $\alpha\text{-LiVOPO}_4$  sintered at 500 °C in a vacuum <sup>5)</sup>. If we consider our results relative to that, it is clear that an air environment is required for direct conversion from  $\alpha_1\text{-LiVOPO}_4$  to  $\beta\text{-LiVOPO}_4$  in the sintering process. An insufficient amount of supplied air temporarily caused a partial  $\alpha\text{-LiVOPO}_4$  phase, which appeared between 420 °C and 520 °C.

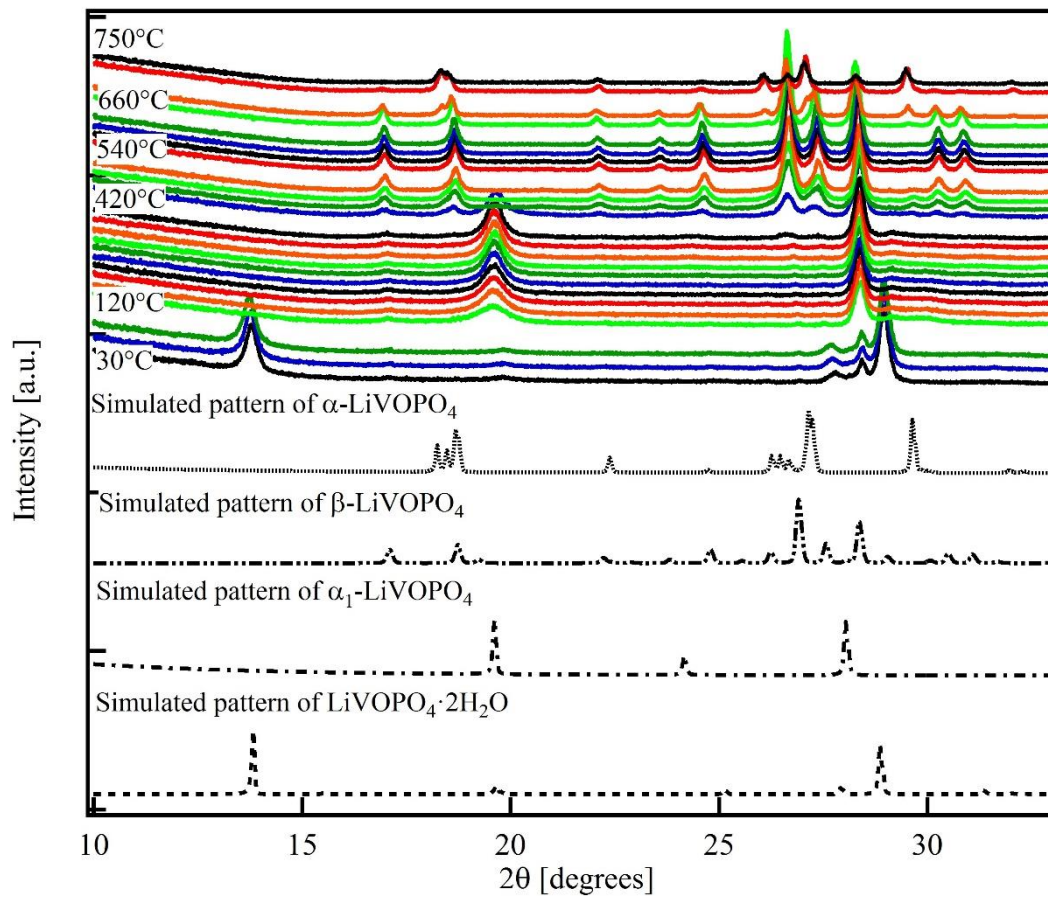


Fig. 2-3. *In-situ* heating XRD pattern of precursor from 30 to 750 °C in 30 °C steps and simulated XRD patterns.

### 2. 3. 2 Evaluation of crystallinity of LiVOPO<sub>4</sub>

The morphology of particles was observed using SEM. Figure 2-4 shows the result of SEM observation of each LiVOPO<sub>4</sub> before and after ball milling with acetylene black. Prior to ball milling, the particle morphology of  $\alpha_1$ -LiVOPO<sub>4</sub> was scaly crystal, and  $\beta$ -LiVOPO<sub>4</sub> had a nearly scale-like shape in which spherical crystals were densely aggregated, while that of  $\alpha$ -LiVOPO<sub>4</sub> was isolated single crystals. The morphology of particles in each phase was different than previous reports<sup>8, 9</sup>). This could be attributed to the synthesizing method and differences in raw materials for LiVOPO<sub>4</sub>. Although the particle size of  $\alpha$ -LiVOPO<sub>4</sub> is the largest of the three phases (> 5  $\mu\text{m}$ ), the ball-milling process succeeded in downsizing it.

Figure 2-5 shows the XRD pattern results and those of the Rietveld refinement for  $\alpha_1$ -LiVOPO<sub>4</sub> (a),  $\beta$ -LiVOPO<sub>4</sub> (b), and  $\alpha$ -LiVOPO<sub>4</sub> (c), examined after ball milling with acetylene black. Almost all the diffraction peaks are ascribed with each phase; however, diffraction peaks of  $\alpha_1$ -LiVOPO<sub>4</sub> are wider, indicating lower crystallinity than the other phases, and slight impurity was found. Low crystallinity is considered to be due to low sintering temperature. Other phases did not have impurity. Table 2-1 lists the structural parameter results, as well as reliability factors after the Rietveld analysis. Reliability factors were small enough to discuss crystal structure except for  $\alpha_1$ -LiVOPO<sub>4</sub>. See the differential XRD profile of Fig. 2-5 (a) indicated by the blue line; we found that the calculated profile was substantially off at around 20°. This diffraction peak is from the (001) reflection, and it indicates c-axis orientation. Hence, only the lattice constant could be refined by the Rietveld method. For this reason, reliability factors of  $\alpha_1$ -LiVOPO<sub>4</sub> were worse. Figure 2-6 shows the crystal structure of each LiVOPO<sub>4</sub> drawn using parameters derived from the Rietveld refinement. Only the lattice parameters are reflected in Fig. 2-6 (a), and atomic coordinates of  $\alpha_1$ -LiVOPO<sub>4</sub> were applied based on previously reported data<sup>10</sup>). It can be seen that structural parameters are much closer to previous reports<sup>11, 12</sup>).

Cross-sectional annular dark field STEM (ADF-STEM) images of the cathode are shown in Fig. 2-7. All of the particles are formed single particles.  $\alpha_1$ -LiVOPO<sub>4</sub> retains its scaly shape and the short direction of a particle is the c-axis. Although particle downsizing was achieved by the ball-milling process, particle diameter was still large for a polyanion

cathode active material suggesting poor electric conductivity. It is considered that  $\alpha_1$ -LiVOPO<sub>4</sub> has a layered structure, and vertical to the c-axis is stronger than the c-axis because VO<sub>5</sub> and PO<sub>4</sub> form a corner-sharing network in the a-b plane, as shown in Fig. 2-6, so that it is difficult to crush these particles oriented in the c-axis uniformly.  $\beta$ -LiVOPO<sub>4</sub> had the smallest particle diameter of the three phases, with particle size in the range from about 100 nm to 1  $\mu$ m. Most of the volume of the cathode coating layer was occupied by small particles.  $\alpha$ -LiVOPO<sub>4</sub> consisted of small particles (around 100 nm) and large particles (over 1  $\mu$ m). The coating layer was equally occupied by the small and large particles.

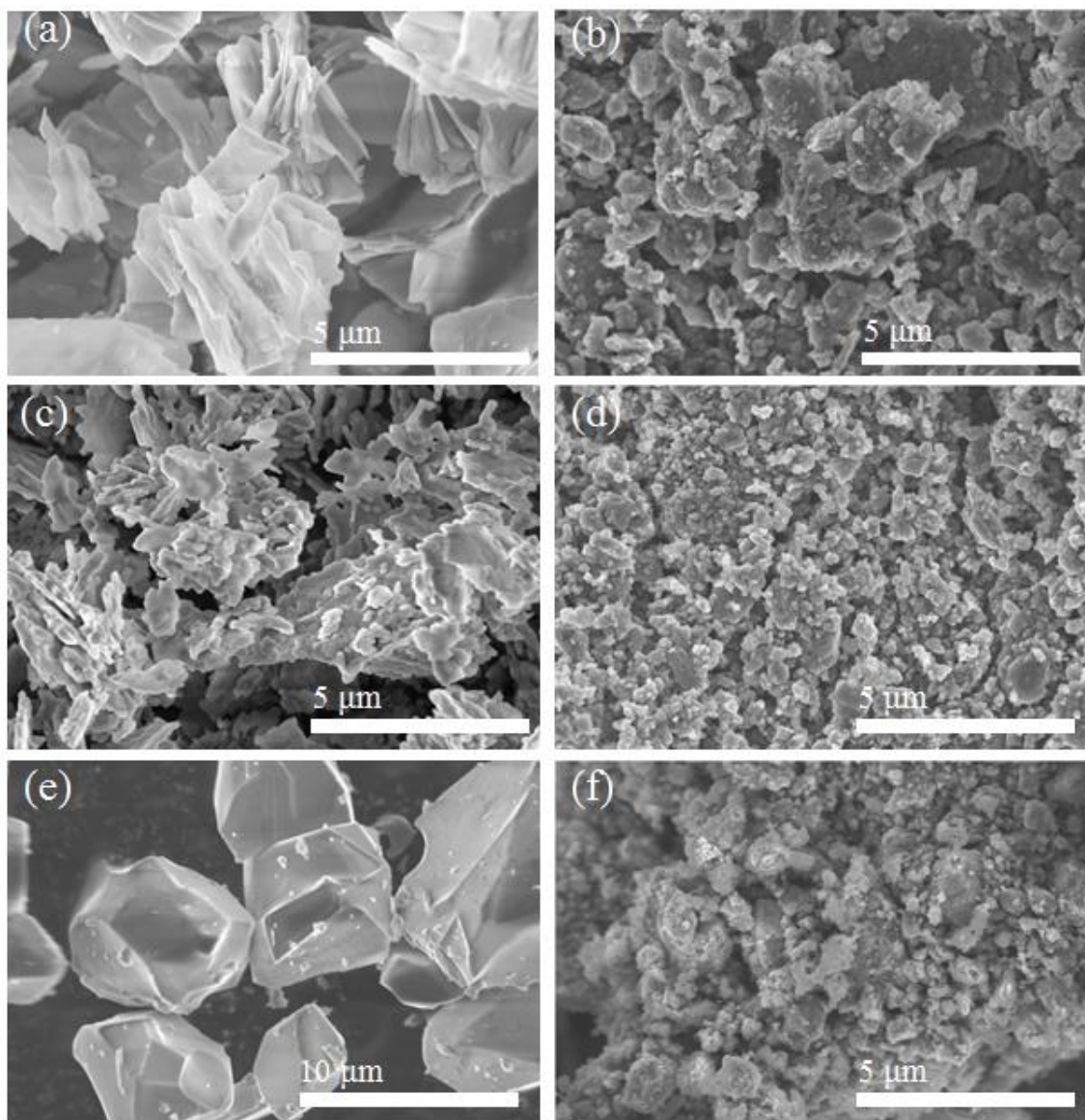


Fig. 2-4. SEM images of  $\alpha_1$ -LiVOPO<sub>4</sub> after sintering at 350 °C for 4 h (a) and after ball milling with acetylene black (b);  $\beta$ -LiVOPO<sub>4</sub> after sintering at 550 °C for 4 h (c) and after ball milling with acetylene black (d); and  $\alpha$ -LiVOPO<sub>4</sub> after sintering at 750 °C for 4 h (e) and after ball milling with acetylene black (f).

Table 2-1.

## Lattice parameters and reliability factor

Parameter	$\alpha_1$ -LiVOPO <sub>4</sub>	$\beta$ -LiVOPO <sub>4</sub>	$\alpha$ -LiVOPO <sub>4</sub>
Space group	<i>P4/nmm</i>	<i>Pnma</i>	<i>P-1</i>
Lattice parameter			
a (Å)	6.29602 (80)	7.45219(11)	6.74383(7)
b (Å)	6.29602 (80)	6.29303(9)	7.20203(8)
c (Å)	4.46295 (157)	7.18008(11)	7.91754(6)
$\alpha$ (deg)	90	90	89.8278(5)
$\beta$ (deg)	90	90	91.3239(5)
$\gamma$ (deg)	90	90	116.9375(6)
Reliability factor			
$R_{wp}$ (%)	20.013	6.234	6.574
$S$	3.7892	1.3416	1.1553
$R_B$ (%)	19.576	1.543	1.505
$R_F$ (%)	10.781	0.793	0.689
VO <sub>6</sub> local environments			
V–O (Å)		1.630(3)	1.615(8)
		2.343(3)	2.272(9)
		1.924(3)	2.022(9)
		1.9307(18)	1.968(8)
		1.9307(18)	1.941(8)
		2.073(3)	1.992(8)

Reliability-weighted pattern factor ( $R_{wp}$ ), goodness of fit ( $S$ ), reliability Bragg factor ( $R_B$ ), reliability structure factor ( $R_F$ ) for each LiVOPO<sub>4</sub> phase via the Rietveld refinements.

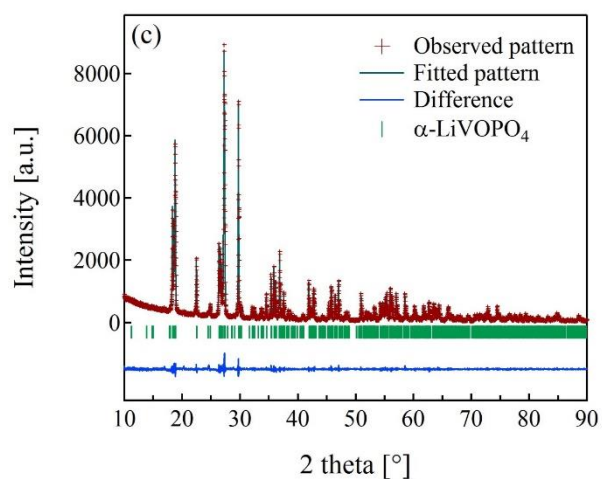
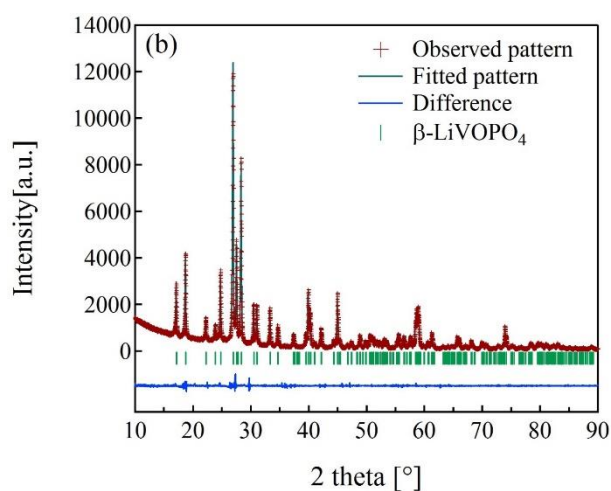
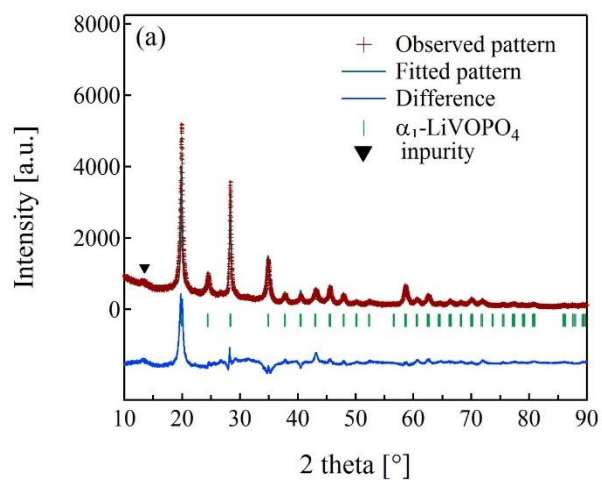


Fig. 2-5. Observed (crosses), calculated (black line), and differential (blue line) XRD profiles of  $\alpha_1$ -LiVOPO<sub>4</sub> (a),  $\beta$ -LiVOPO<sub>4</sub> (b), and  $\alpha$ -LiVOPO<sub>4</sub> (c). Vertical bars mark the possible Bragg reflection positions of each phase.

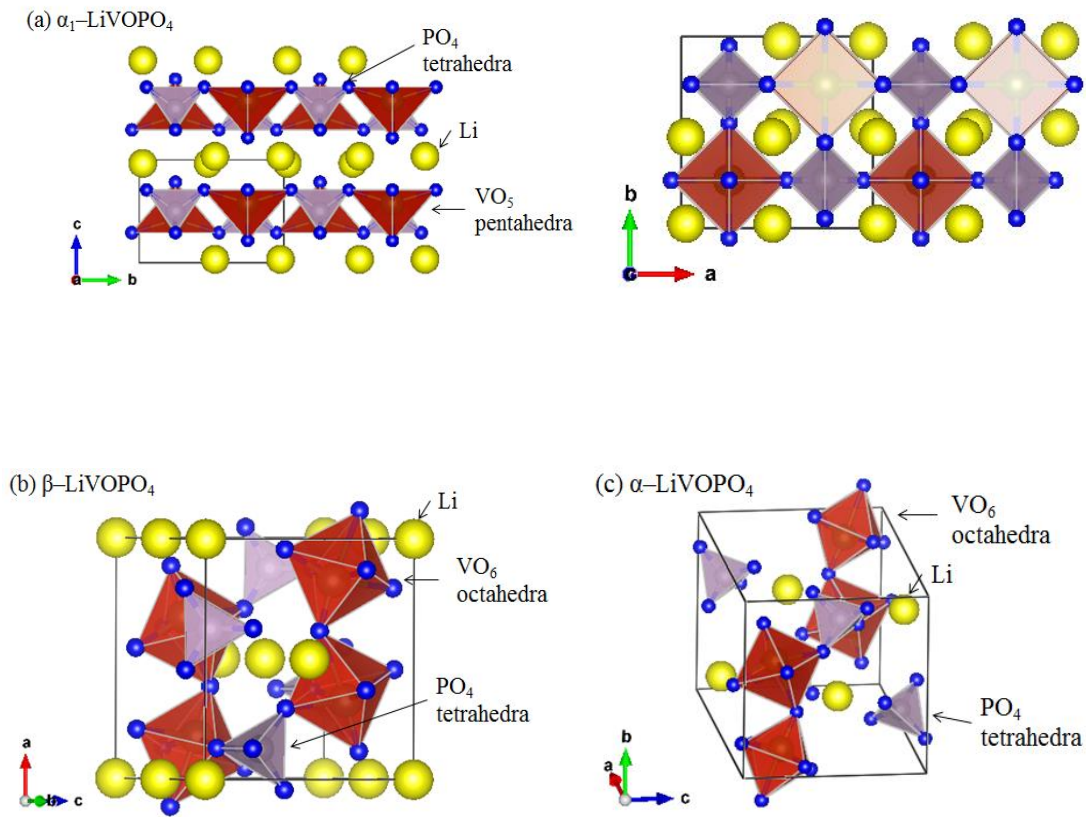


Fig. 2-6. Crystal structure of  $\alpha_1$ -LiVOPO<sub>4</sub> (a),  $\beta$ -LiVOPO<sub>4</sub> (b), and  $\alpha$ -LiVOPO<sub>4</sub> (c) drawn using parameters derived from the Rietveld refinement.  $\alpha_1$ -LiVOPO<sub>4</sub> consists of distorted VO<sub>5</sub> pentahedrons and PO<sub>4</sub> tetrahedrons, and VO<sub>5</sub> is connected to four other PO<sub>4</sub> tetrahedrons by corner sharing toward the a- and b-axis.  $\beta$ -LiVOPO<sub>4</sub> and  $\alpha$ -LiVOPO<sub>4</sub> are composed of distorted VO<sub>6</sub> octahedrons and PO<sub>4</sub> tetrahedrons. Both VO<sub>6</sub> octahedrons make a network with four PO<sub>4</sub> tetrahedrons and the two other VO<sub>6</sub> octahedrons by corner sharing.

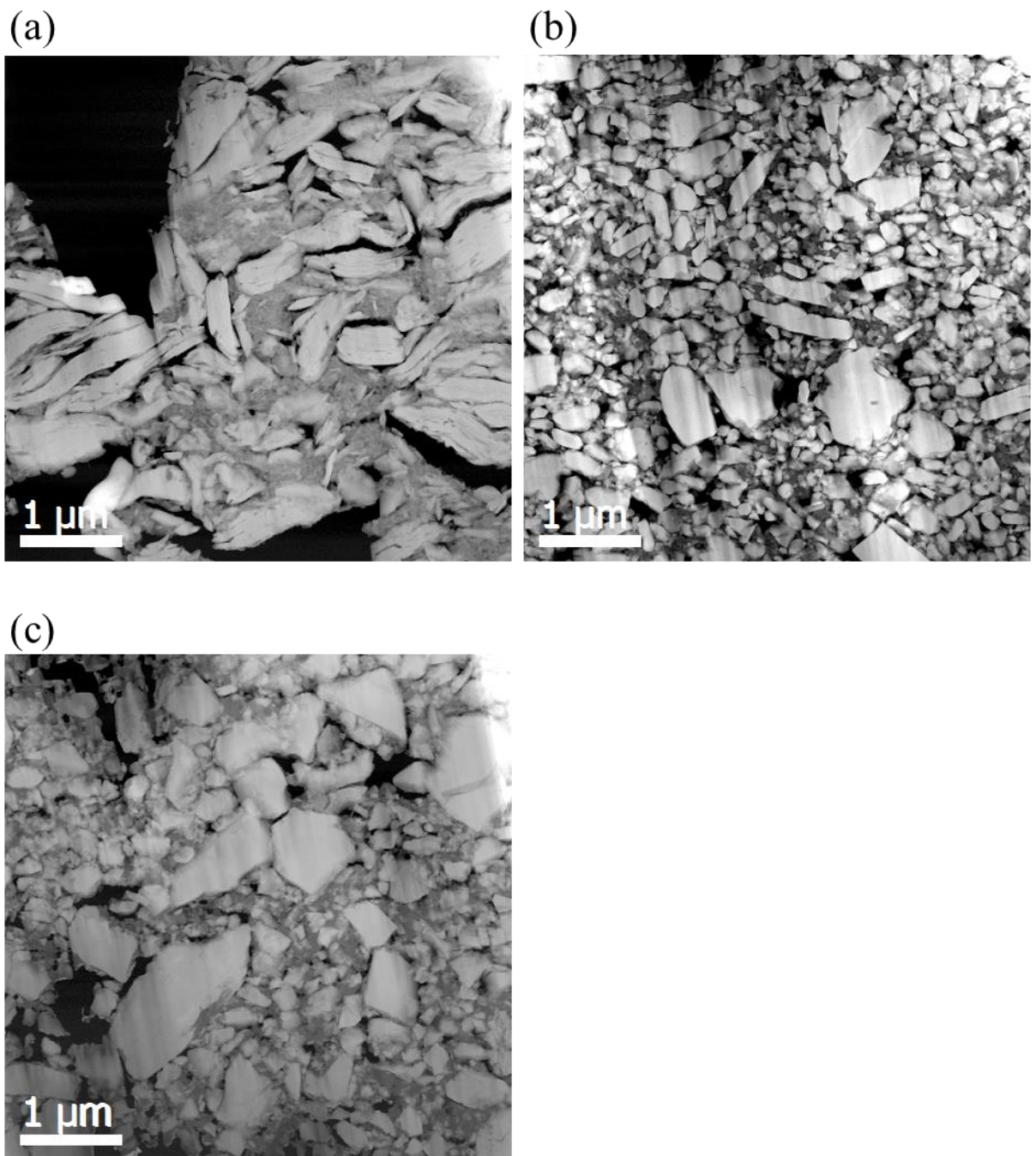


Fig. 2-7. Cross-sectional annular dark field STEM images of  $\alpha_1$ -LiVOPO<sub>4</sub> (a),  $\beta$ -LiVOPO<sub>4</sub> (b), and  $\alpha$ -LiVOPO<sub>4</sub> (c) cathode.

### 2.3.3 Electrochemical evaluation for LiVOPO<sub>4</sub>

We studied the electrochemical performance of  $\alpha_1$ -,  $\beta$ -, and  $\alpha$ -LiVOPO<sub>4</sub> in a voltage range of 2.8–4.3 V. Figure 2-8 shows the first and second charge/discharge curves at a rate of C/10. First and second charge capacities are listed in Table 2-2. The capacity of  $\alpha_1$ -LiVOPO<sub>4</sub> was higher than in previous reports despite the low crystallinity<sup>5)</sup>. The voltage profile of  $\alpha_1$ -LiVOPO<sub>4</sub> was slightly different from previous reports<sup>5, 11)</sup>. Open circuit voltage (OCV) before charging was around 3.5 V in our cell (vs. Li/Li<sup>+</sup>), compared to less than 3.0 V in previous reports. Considering that the plateau voltage is around 4.0 V, which is attributed to two-phase coexistence (LiVOPO<sub>4</sub> and VOPO<sub>4</sub>), and lithium extraction is finished from 4.2 to 4.3 V, OCV should be around 3.5 V before the first charge. Furthermore, a slight slope can be seen at the beginning stage of charging. It is considered that the low crystallinity of  $\alpha_1$ -LiVOPO<sub>4</sub> affected the potential sensitively.

The discharge capacity of  $\beta$ -LiVOPO<sub>4</sub> was 140 mAh/g. This capacity was higher than all previous reports<sup>1-3, 13)</sup>. The first charge of  $\beta$ -LiVOPO<sub>4</sub> showed an unstable voltage profile at the initial stage of the plateau region compared to the second charge profile. On the other hand, the capacity of  $\alpha$ -LiVOPO<sub>4</sub> was about half of theoretical capacity. Furthermore, an increase in the plateau voltage due to overvoltage was observed at the first charge voltage profile. Although the second charge/discharge curves of  $\alpha$ -LiVOPO<sub>4</sub> and  $\beta$ -LiVOPO<sub>4</sub> corresponded to previous reports, both first charge voltages were different<sup>1-4, 8, 9, 12-16)</sup>. This may have been due to some type of damage at the particle surface caused during the ball-milling process. It is assumed that something like activation is needed before stable insertion/extraction.

Discharge rate performance from C/10 to 5 C of  $\alpha_1$ -,  $\beta$ -, and  $\alpha$ -LiVOPO<sub>4</sub> at a voltage range of 2.8–4.3 V is shown in Fig. 2-9. We found that  $\alpha_1$ -LiVOPO<sub>4</sub> and  $\beta$ -LiVOPO<sub>4</sub> exhibited excellent rate performance. These cells could retain more than half of theoretical capacity at 1 C. On the other hand, although  $\alpha$ -LiVOPO<sub>4</sub> exhibited poor capacity, retention of high rate capacity was excellent. This characteristic indicates the possibility of  $\alpha$ -LiVOPO<sub>4</sub> working as cathode active material for high safety and high rate performance battery. Cycle performance is shown in Fig. 2-10. Charge/discharge condition was C/10 CC-CV (C/50 cutoff) charge and C/10 constant current (CC)

discharge at first, respectively, 50th, 100th and 200th cycles, and C/2 CC-CV (C/50 cutoff) charge 1 C CC discharge at the other cycles. The retention of capacity at 200 cycles was 94.4% ( $\alpha_1$ -LiVOPO<sub>4</sub>), 97.1% ( $\beta$ -LiVOPO<sub>4</sub>) and 108% ( $\alpha$ -LiVOPO<sub>4</sub>). All phases exhibited good cycle performance. As the charge/discharge was repeated, the capacity of  $\alpha$ -LiVOPO<sub>4</sub> gradually increased. A similar phenomenon was reported by Wang *et al.*, where capacity increased until the 22nd cycle<sup>4</sup>); however, our  $\alpha$ -LiVOPO<sub>4</sub> kept increasing during the cycle test.

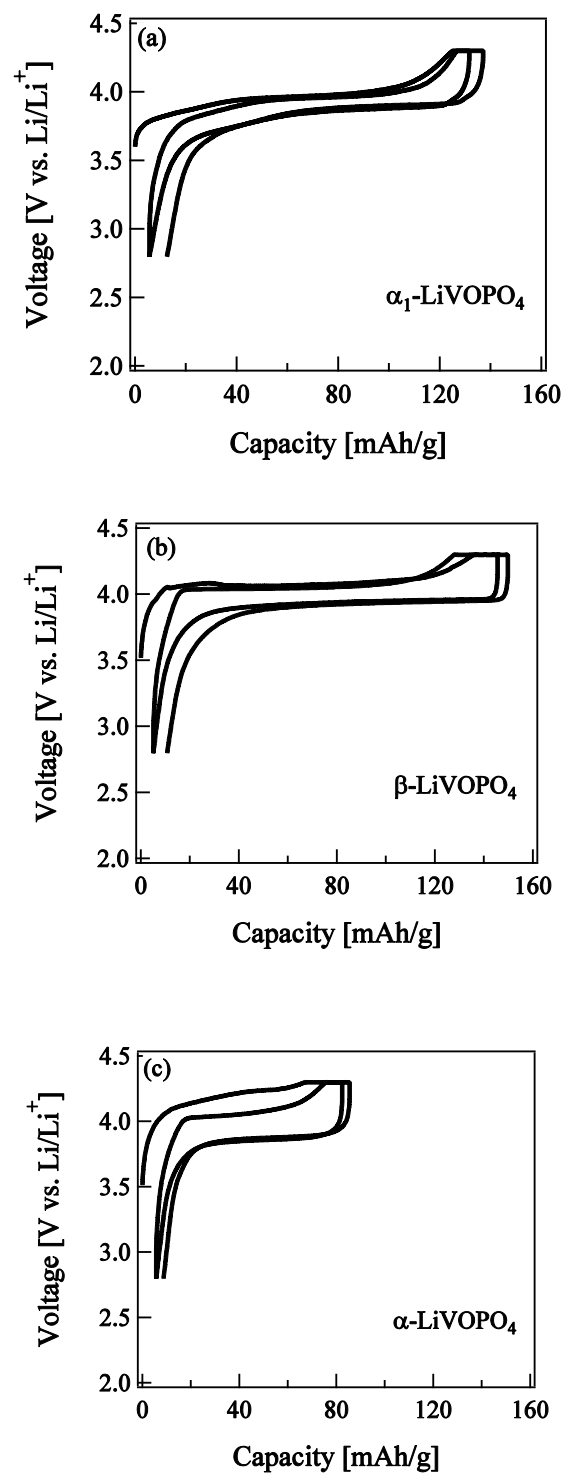


Fig. 2-8. First and second charge/discharge curves of  $\alpha_1\text{-LiVOPO}_4$  (a),  $\beta\text{-LiVOPO}_4$  (b), and  $\alpha\text{-LiVOPO}_4$  (c) at a voltage range of 2.8–4.3 V at  $C/10$  ( $1C = 1.03 \text{ mA/cm}^2$ ).

Table 2-2.

Results of 1st and 2nd charge/discharge capacity in the voltage range of 2.8–4.3 V vs. Li/Li<sup>+</sup> at a rate of C/10

Capacity	$\alpha_1$ -LiVOPO <sub>4</sub>	$\beta$ -LiVOPO <sub>4</sub>	$\alpha$ -LiVOPO <sub>4</sub>
1st charge [mAh/g]	131	145	82.4
1st discharge [mAh/g]	125	140	76.7
2nd charge [mAh/g]	131	144	79.8
2nd discharge [mAh/g]	124	141	76.8

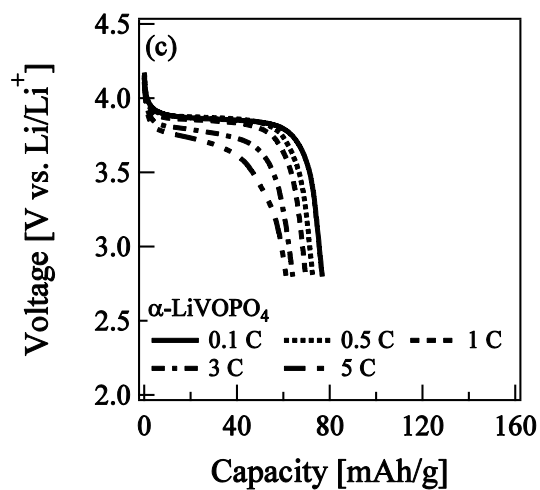
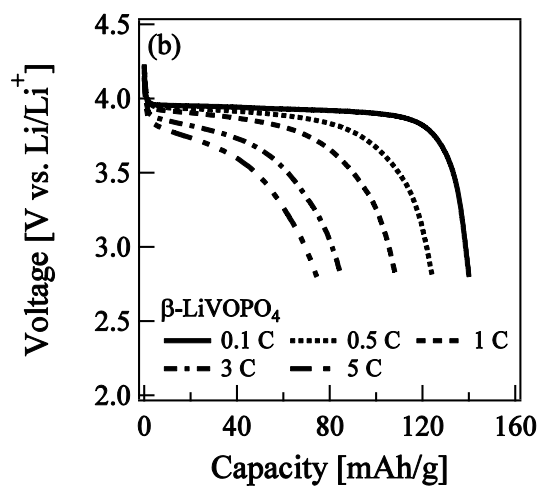
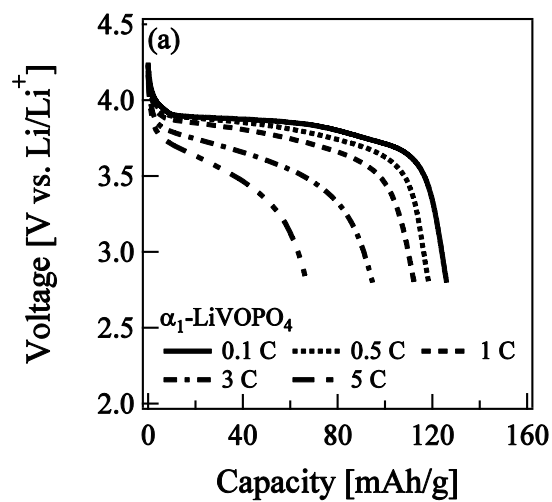


Fig. 2-9. Discharge rate performance of  $\alpha_1$ -LiVOPO<sub>4</sub> (a),  $\beta$ -LiVOPO<sub>4</sub> (b), and  $\alpha$ -LiVOPO<sub>4</sub> (c) at a voltage range of 2.8–4.3 V.

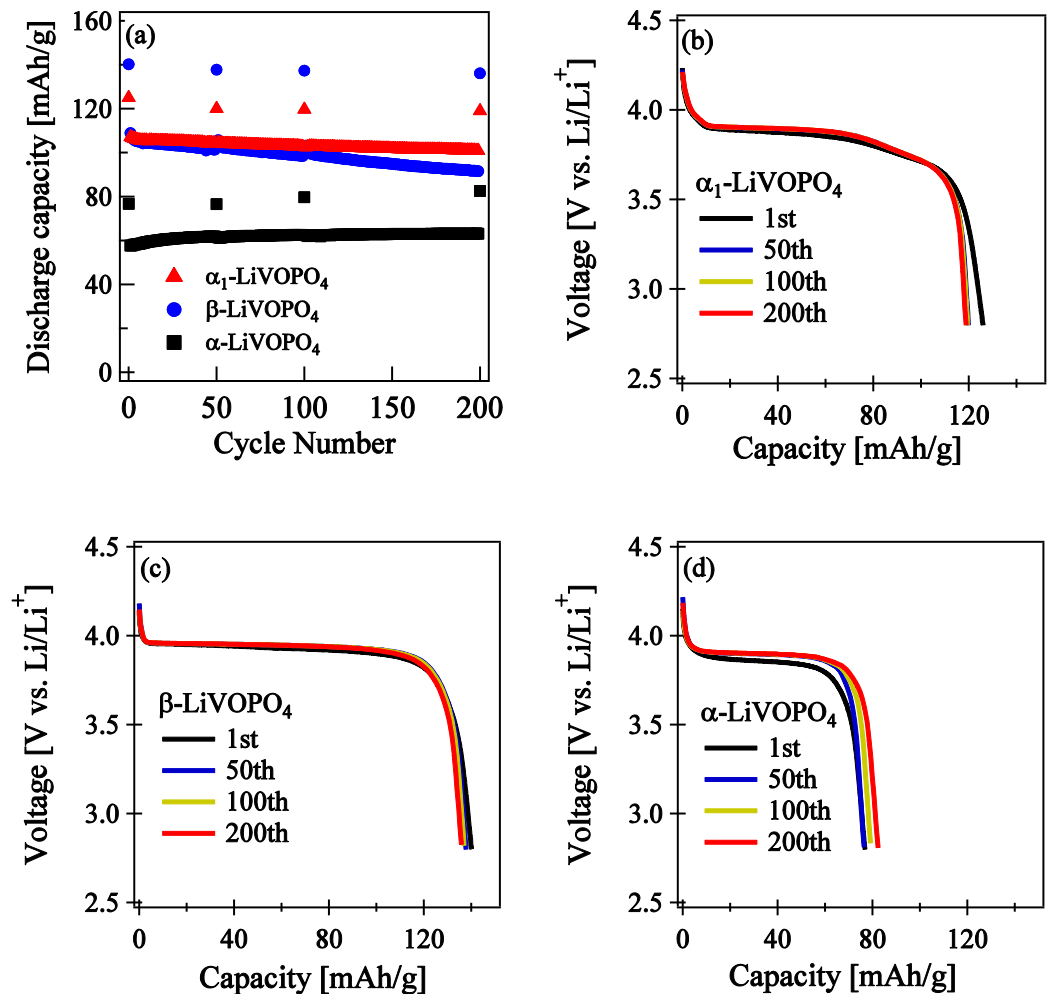


Fig. 2-10. Results of cycle performance C/10 CCCV (C/50 cutoff) charge and C/10 CC discharge at 1st, 50th, 100th and 200th cycles, and C/2 CCCV (C/50 cutoff) charge 1 C CC discharge at the other cycles (a). Discharge curves of  $\alpha_1$ -LiVOPO<sub>4</sub> (b),  $\beta$ -LiVOPO<sub>4</sub> (c), and  $\alpha$ -LiVOPO<sub>4</sub> (d) at 1st, 50th, 100th and 200th cycle.

#### 2.3.4 Lithium deintercalation capability of LiVOPO<sub>4</sub>

The relationship between particle size and lithium deintercalation from each phase particle was investigated by EELS spectrum imaging. After charging at 4.3 V at a rate of C/10 CC-CV (C/50 cutoff), sample preparation for STEM and EELS was examined. Figures 2-11, 2-12, and 2-13 show the results of EELS spectrum imaging of Li, and extracted spectra. Despite the particle size of  $\alpha_1$ -LiVOPO<sub>4</sub> being about 500 nm, EELS spectrum image revealed that almost all Li was extracted. As shown in Fig. 2-11 (b), particle edge is exhibited higher intensity and obviously Li EELS signal can be seen from Fig. 2-11 (c). It seems that the area where slight of Li remained correlated with lack of carbon additives. It is likely that electronic conductivity was lost around the area so that lithium in the particle could not be extracted perfectly in the charging process. On the other hand, particle edge of Fig. 2-11 (e) also shows higher signal intensity, however, as shown in Fig. 2-11 (f) Li EELS spectrum of “Area 3” did not exhibit distinct Li signal. Therefore, it is taken as noise in image processing. It is difficult to say why the capacity could not reach the theoretical value, but it seems that crystallinity relates to the lack of capacity, because some voids were found only in  $\alpha_1$ -LiVOPO<sub>4</sub> particles. These voids would prevent Li from deintercalation, and it is possible that Li would exist below the EELS detection limit (a few atomic %). On the other hand, the Li EELS signal was detected clearly from the 500-nm particle size  $\beta$ -LiVOPO<sub>4</sub> and  $\alpha$ -LiVOPO<sub>4</sub>, as shown in Fig. 2-12 (b), (c) and Fig. 2-13 (b), (c). As mentioned before, the  $\alpha$ -LiVOPO<sub>4</sub> cathode consisted of small and large particles in an even ratio. It can be said that capacity of  $\alpha$ -LiVOPO<sub>4</sub> might have been only half of theoretical capacity because only small particles could contribute to electrochemical performance, while the  $\beta$ -LiVOPO<sub>4</sub> cathode, formed of small particles with higher crystallinity, had the highest capacity of the three phases. From the comparison of particle size  $\beta$ -LiVOPO<sub>4</sub> (Fig. 2-12 (e)) and  $\alpha$ -LiVOPO<sub>4</sub> (Fig. 2-13 (e)), despite the particle size of  $\alpha$ -LiVOPO<sub>4</sub> being larger than  $\beta$ -LiVOPO<sub>4</sub>, the Li signal from  $\alpha$ -LiVOPO<sub>4</sub> could not be detected in all areas. Whereas, distinct Li signal was detected from particle edge of  $\beta$ -LiVOPO<sub>4</sub> as shown in “Area3” of Fig. 2-12 (e) and (f). Thus, it can be said that  $\alpha$ -LiVOPO<sub>4</sub> has a better Li extraction ability than  $\beta$ -LiVOPO<sub>4</sub>.

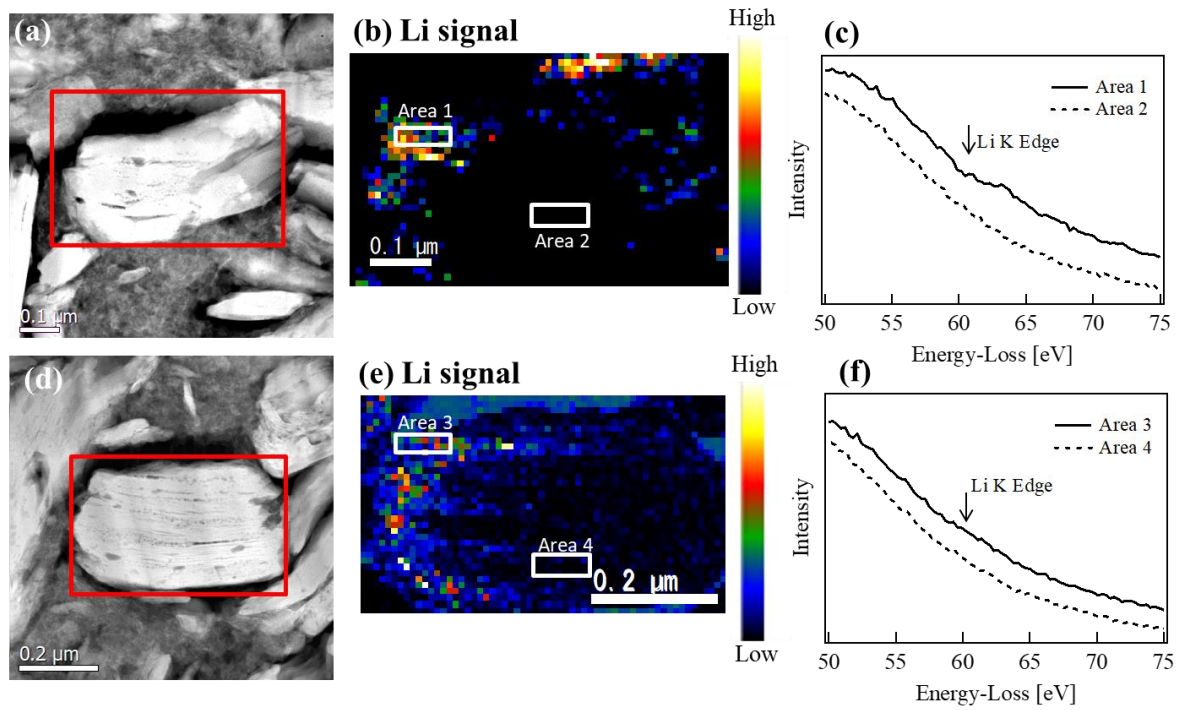


Fig. 2-11. ADF-STEM image of  $\alpha_1$ -LiVOPO<sub>4</sub> (a) (d); EELS signal image of Li from red square in ADF-STEM images (b) (e); extracted EELS spectra from white square in Li EELS signal images (c) (f).

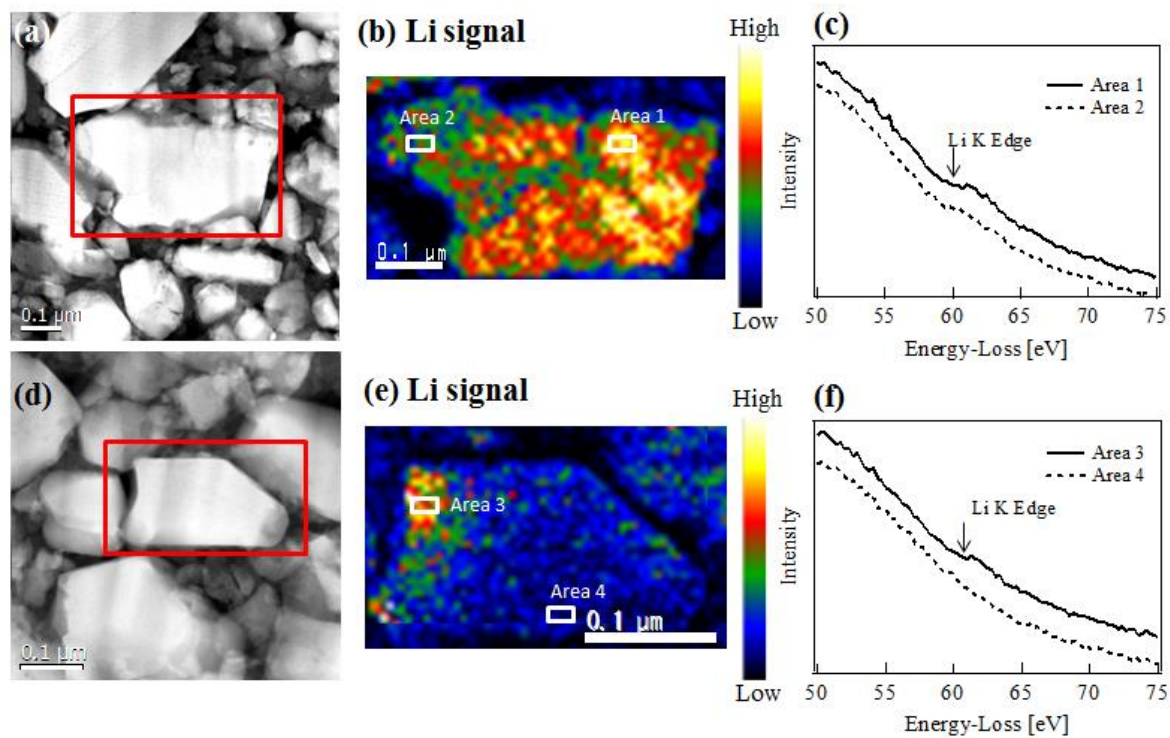


Fig. 2-12. ADF-STEM image of  $\beta$ -LiVOPO<sub>4</sub> (a) (d); EELS signal image of Li from red square in ADF-STEM images (b) (e); extracted EELS spectra from white square in Li EELS signal images (c) (f).

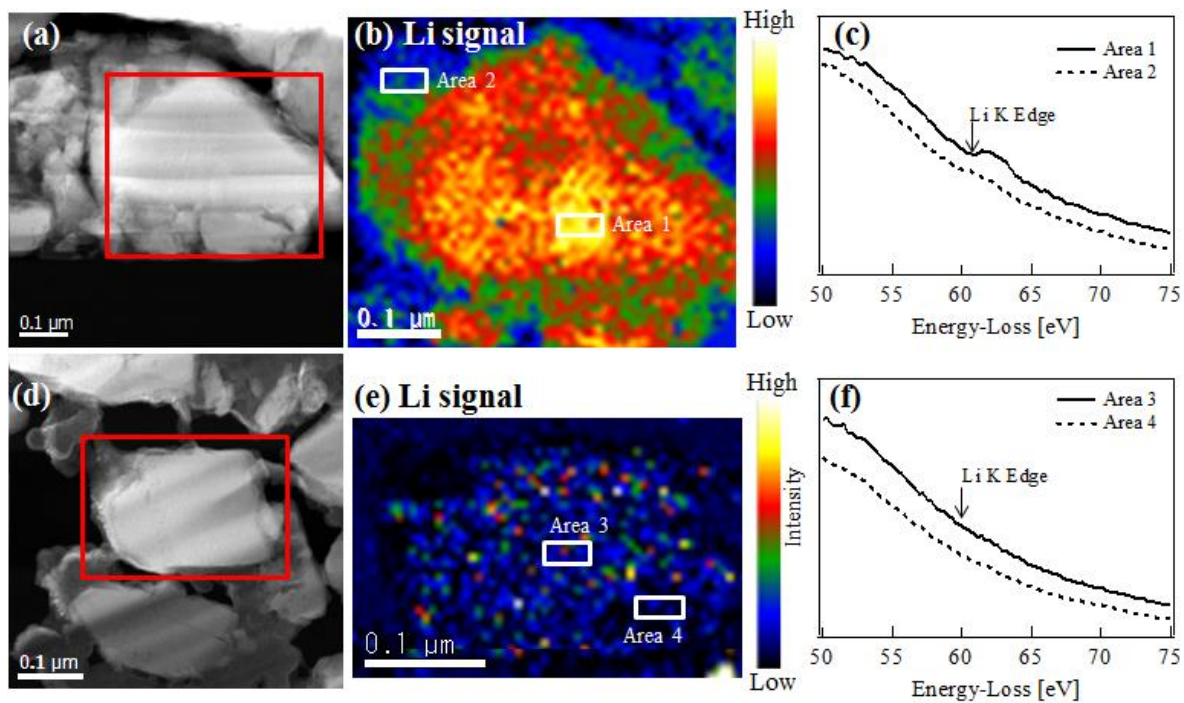


Fig. 2-13. ADF-STEM image of  $\alpha$ -LiVOPO<sub>4</sub> (a) (d); EELS signal image of Li from red square in ADF-STEM images (b) (e); extracted EELS spectra from white square in Li EELS signal images (c) (f).

## 2. 4 Conclusions

Three phases of  $\text{LiVOPO}_4$  were synthesized via a hydrothermal method and subsequent sintering process, and we characterized the electrochemical performance of each phase. The features of each  $\text{LiVOPO}_4$  synthesized by our hydrothermal method and ball-milling process were as follows.  $\alpha_1$ - $\text{LiVOPO}_4$  showed 125 mAh/g at first discharge, and Li EELS spectrum images revealed Li deintercalation from the large particle.  $\beta$ - $\text{LiVOPO}_4$  was shown to have excellent discharge capacity (140 mAh/g) at C/10, close to theoretical capacity.  $\alpha$ - $\text{LiVOPO}_4$  exhibited only 76.7 mAh/g due to the cathode being formed with large particles and small particles in an even ratio, while only small particles could contribute to the electrochemical property. However,  $\alpha$ - $\text{LiVOPO}_4$  showed better rate performance. We conclude from our study that  $\alpha$ - $\text{LiVOPO}_4$ , with a particle size below 200 nm, is superior to the other crystal phases.

## Reference

- 1 J. Barker, M.Y. Sadi, and J.L. Swoyer, *J. Electrochem. Soc.*, **151** A796 (2004).
- 2 B.M. Azmi, T. Ishihara, H. Nishiguchi, and Y. Takita, *J. Power Sources*, **146** 525 (2005).
- 3 M.M. Ren, Z. Zhou, L.W. Su, and X. P. Gao, *J. Power Sources*, **189** 786 (2009).
- 4 L. Wang, L. Yang, L. Gong, X. Jiang, K. Yuan, and Z. Hu, *Electrochim. Acta*, **56** 6906 (2011).
- 5 A.S. Hameed, M. Nagarathinam, M.V. Reddy, and B.V.R. Chowdan, J.J. Vittal, *J. Mater. Chem.*, **22** 7206 (2012).
- 6 K.L. Harrison and A. Manthiram, *Chem. Mater.*, **25** 1751 (2013).
- 7 F. Izumi and K. Momma, *Solid State Phenom.*, **130** 15 (2007).
- 8 A. Tang, J. Shen, Y. Hu, G. Xu, D. He, Q. Yi, and R. Peng, *J. Electrochem. Soc.*, **161** A10 (2014).
- 9 K. Saravanan, H.S. Lee, M. Kuezma, J.J. Vittal, and P. Balaya, *J. Matter. Chem.*, **21** 10042 (2011).
- 10 N. Dupre, G. Wallez, J. Gaubicher, and M. Quarton, *J. Solid State Chem.*, **117** 2896 (2004).
- 11 G. He, C. A. Bridges, and A. Manthiram, *Chem. Mater.*, **27** 6699 (2015).
- 12 Y. Yang, H. Fang, J. Zheng, L. Li, G. Li, and G. Yan, *Solid State Sci.*, **10** 1292 (2008).
- 13 C.J. Allen, Q. Jia, C.N. Chinnasamy, S. Mukerjee, and K. M. Abraham, *J. Electrochem. Soc.*, **158** A1250 (2011).
- 14 N.F. Quackenbush, L. Wangoh, D.O. Scanlon, R. Zhang, Y. Chung, Z. Chen, B. Wen, Y. Lin, J.C. Woicik, N.A. Chernova, S.P. Ong, M.S. Whittingham, and L.F.J. Piper, *Chem. Mater*, **27** 8211 (2015).
- 15 Y. Lin, B. Wen, K.M. Wiaderek, S. Sallis, H. Liu, S.H. Lapidus, O.J. Chupas, L.F.J. Piper, M.S. Whittingham, K.W. Chapman, and S.P. Ong, *Chem Mater*, **28** 1794 (2016).
- 16 Z. Liu, Z. Su, and H. Tian, *Ceram. Int.*, **44** 9372 (2018).

# Chapter 3

## **Electrochemical Characterization, Structural Evolution, and Thermal Stability of $\text{LiVOPO}_4$ over Multiple Lithium Intercalations**

### 3. 1 Introduction

As mentioned in Chapter 1, multi-electron phosphate materials such as  $\text{Li}_3\text{V}_2(\text{PO}_4)_3$ <sup>1, 2)</sup> and  $\text{LiVOPO}_4$ <sup>3-11)</sup> have attracted attention as an alternatives to  $\text{LiFePO}_4$  due to their higher energy densities. Rui *et al.* reported the characteristics of  $\text{Li}_3\text{V}_2(\text{PO}_4)_3$  as an anode and showed that Li intercalated stepwise between 2.0 V and 1.6 V and was about 130 mAh /g; however, its energy density is too low for it to be useful as an anode active material<sup>12)</sup>. Moreover,  $\text{Li}_3\text{V}_2(\text{PO}_4)_3$  could not be extracted last lithium, and the capacity related to the  $\text{V}^{3+}/\text{V}^{4+}$  couples<sup>13)</sup>. On the other hand,  $\text{LiVOPO}_4$  has three types of crystal structure:  $\alpha_1$ - $\text{LiVOPO}_4$  (tetragonal phase)<sup>3-5, 14, 15)</sup>,  $\beta$ - $\text{LiVOPO}_4$  (orthorhombic phase)<sup>6-8, 16-19)</sup>, and  $\alpha$ - $\text{LiVOPO}_4$  (triclinic phase; some reports described the third type as  $\varepsilon$ - $\text{LiVOPO}_4$ )<sup>9-11, 20-23)</sup>. Good electrochemical performance was found by the use of both the  $\text{V}^{3+}/\text{V}^{4+}$  and  $\text{V}^{4+}/\text{V}^{5+}$  redox couples. The crystal structure evolution from  $\text{LiVOPO}_4$  to  $\text{Li}_2\text{VOPO}_4$  in relation to  $\alpha_1$ - $\text{LiVOPO}_4$ <sup>3)</sup>,  $\beta$ - $\text{LiVOPO}_4$ <sup>6, 7)</sup>, and  $\alpha$ - $\text{LiVOPO}_4$ <sup>9, 10)</sup> has been studied, but the discharge voltages were 1.5 V, so it is hard to discuss the possibility of valence of vanadium becoming less than a trivalent state and generates larger capacity. Although  $\text{LiVOPO}_4$  is expected to have high thermal stability because it consists of  $\text{PO}_4$ , no report has actually evaluated this.

As described in Chapter 2, we succeeded in producing three phases of lithium vanadium phosphate ( $\alpha_1$ -,  $\beta$ -, and  $\alpha$ - $\text{LiVOPO}_4$ ) from the same precursor that was synthesized by the hydro-thermal method<sup>24)</sup>. In this chapter, we used these  $\text{LiVOPO}_4$  to reveal the relationship between electrochemical properties and crystal structure evolution in the low-voltage region up to 1.0 V using *operando* XRD and XAFS. We also discussed the thermal stability of  $\text{LiVOPO}_4$

## 3. 2 Experimental

### 3. 2. 1 Preparation for LiVOPO<sub>4</sub>

Three phases of LiVOPO<sub>4</sub> were prepared by a hydrothermal method and subsequent sintering process as described in Chapter 2 <sup>24</sup>). The prepared LiVOPO<sub>4</sub> was mixed with acetylene black at a weight ratio of 92:8, and ball milling was used to downsize the LiVOPO<sub>4</sub> particles and to carbon coat the surface. The crystal structure of each phase was confirmed using powder X-ray diffractometer (Ultima IV, Rigaku) with Cu K $\alpha$  radiation ( $\lambda = 0.15418$  nm).

### 3. 2. 2 Electrode and half-cell fabrication, and evaluation method

The electrochemical characterization was carried out with Al laminate-type cells assembled in a dry room in which the dew point was  $-40\text{ }^{\circ}\text{C}$ . Electrodes were fabricated by casting the slurry, which was made from the downsized and carbon-coated  $\text{LiVOPO}_4$  and PVDF at a weight ratio 92:8 in NMP. The active material was around  $6\text{ mg/cm}^2$  on Al foil. The half-cell type of Al laminate cells were used, consisting of the  $\text{LiVOPO}_4$  electrode as a cathode, Li metal on Cu as an anode, and a separator (2400, Celgard). As an electrolyte, 1 M of  $\text{LiPF}_6$  in a solution of ethylene carbonate (EC) and diethyl carbonate (DEC; volume ratio of EC:DEC = 3:7) was used. Charge/discharge testing was performed by a battery charge/discharge system (SM-8, Hokuto Denko) at room temperature.

### 3. 2. 3 Characterization for LiVOPO<sub>4</sub>

The crystal structure evolution of LiVOPO<sub>4</sub> during charging and discharging was measured by *operando* X-ray diffraction (XRD) in transmission geometry (Empyrean, Panalytical), using the same configuration of half-cells described above. The charge/discharge rate was C/10 at the voltage range of 4.8–1.0 V for the first charge/discharge and for the charge to 3.9 V. XRD patterns were collected every hour. The scan rate of a scan was 360 s, and the 2θ step size was 0.026 ° in the 2θ range of 10–36 °.

The vanadium valence of LiVOPO<sub>4</sub> in discharge states was analyzed from the V-K edge X-ray absorption near-edge structure (XANES). *Ex-situ* X-ray absorption spectroscopy (XAS) measurements for V-K edge absorption were performed at beamline BL05S1 at the Aichi Synchrotron Radiation Center. Figure 3-1 shows the photo inside the experimental hatch <sup>26</sup>). BL5S1 performs XAFS measurement to analyze the bonding state and local structure of atoms in the materials. Because the energy range is from 5 to 20 keV, it can measure scandium to molybdenum at the K-edge, and indium to uranium at the LIII-edge. Since the K-edge of vanadium is 5.5 keV, it is appropriate to choose this beamline. The measuring table layout is shown in Fig. 3-2 <sup>26</sup>).

The measured electrode samples were extracted from disassembled cells, which had been discharged at target voltage and resealed by an Al laminate in a glove box. The XAS data were collected in quick-scan mode. XANES data were normalized by using Athena developed by Ravel and Newville <sup>25</sup>). Energy was calibrated by using XANES of vanadium thin foil.

The thermal stability of LiVOPO<sub>4</sub> was evaluated by a differential scanning calorimetry (DSC, DSC6220, Hitachi) method at a heating rate of 5 °C/min up to 400 °C. Cells at the target voltage were disassembled in a glove box and the electrodes were washed with DEC. Subsequently, punch out with 3 mm of diameter from the electrode. Three sheets of punched-out samples were packed into stainless steel DSC capsules with 4.5 mg of electrolyte and then hermetically sealed.

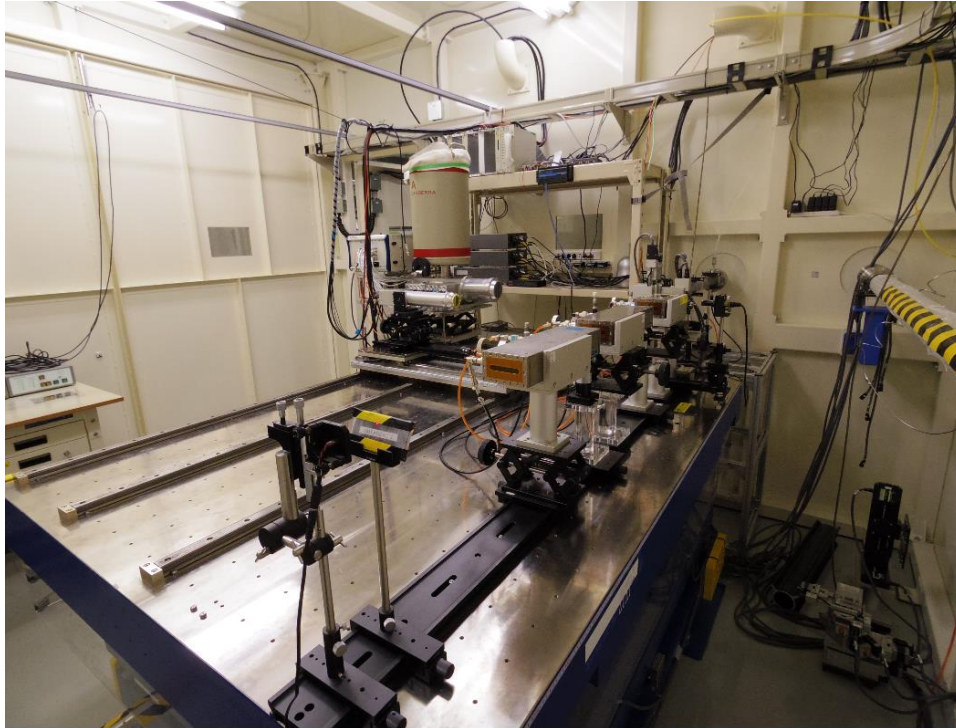


Fig. 3-1. Inside of beamline BL05S1 experiment hatch at Aichi synchrotron Radiation center <sup>26)</sup>.

Quoted from home page of Aichi synchrotron radiation center.

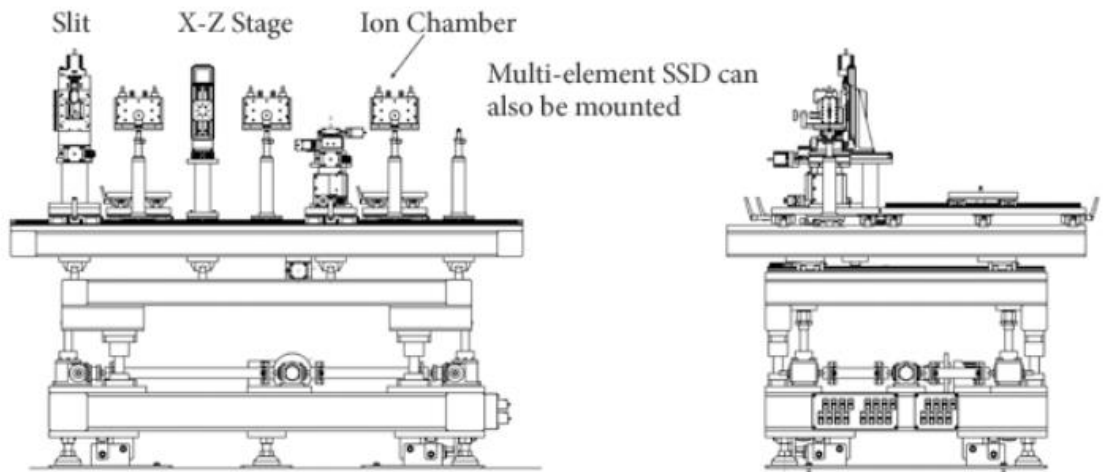


Fig. 3-2. Measuring table layout <sup>26)</sup>

Quoted from home page of Aichi synchrotron radiation center

### 3. 3 Results and Discussion

#### 3. 3. 1 Electrochemical performance at low voltage region

Figure 3-3 shows the first and second charge/discharge curves of  $\alpha_1$ -,  $\beta$ -, and  $\alpha$ -LiVOPO<sub>4</sub> in the voltage range of 1.0–4.5 V at a rate of 0.05 C (1 C = 1.07 mA/cm<sup>2</sup>). The profiles were the same at the first charge, but the discharge profiles and second charge profiles clearly differed among the three phases. The first charge and discharge capacities of  $\alpha_1$ -LiVOPO<sub>4</sub> were 123 mAh/g and 288 mAh/g, respectively. The characteristics of the  $\alpha_1$ -LiVOPO<sub>4</sub> charge/discharge curve correspond to those of previous reports<sup>3, 4</sup>. Although the first charge capacity of our  $\alpha_1$ -LiVOPO<sub>4</sub> was lower than those previously published values, the discharge capacity accorded with the discharge capacities considering different cutoff voltages. Discharge capacity from 3.0–1.0 V was 165 mAh/g, even though the theoretical capacity of the reaction (LiVOPO<sub>4</sub> (V<sup>4+</sup>) ↔ Li<sub>2</sub>VOPO<sub>4</sub> (V<sup>3+</sup>)) is 159 mAh/g. Therefore, it could be expected that the valence of vanadium was decreased to below V<sup>3+</sup>. On the other hand, charging from 1.0 V requires high voltage to deintercalate Li, which is associated with overpotential<sup>5</sup>). Therefore, the second charge capacity from 3.0–4.5 V was larger than the first. The first charge and discharge capacities of  $\beta$ -LiVOPO<sub>4</sub> were 139 mAh/g and 354 mAh/g, respectively. Three plateau regions appeared in the discharge curve at 3.9, 2.0, and 1.1 V. The first (V<sup>5+</sup>/V<sup>4+</sup>) and second (V<sup>4+</sup>/V<sup>3+</sup>) plateaus corresponded to previous reports<sup>6-8, 11</sup>). The discharge capacity from 3.0–1.0 V was 215 mAh/g. Apparently this is larger than the theoretical capacity, so the valence of vanadium should be decreased to below V<sup>3+</sup> or the structure change from  $\beta$ -LiVOPO<sub>4</sub> to Li<sub>3</sub>PO<sub>4</sub> occurred as Ren *et al.* reported<sup>8</sup>); if the valence of vanadium decreased, the reaction at the third plateau could be considered to be a V<sup>3+</sup>/V<sup>2+</sup> redox couple. The capacity of the second plateau region was 134 mAh/g, which almost matched the first charge capacity. Unlike the case with  $\alpha_1$ -LiVOPO<sub>4</sub>, the V<sup>4+</sup>/V<sup>3+</sup> discharge did not achieve theoretical capacity. On the other hand, the voltage profile of the second charge was slightly out of shape. The first charge capacity of  $\alpha$ -LiVOPO<sub>4</sub> was 99 mAh/g, but the discharge capacity from 4.5–1.0 V was 257 mAh/g and the capacity of 3.0–1.0V was 158 mAh/g. That is, the theoretical capacity could be achieved in the low-voltage region. This indicates that the lithium intercalate ability differs between high- and low-voltage regions.

Furthermore, the voltage profile is relatively the same for charging and discharging. Three distinct plateaus appeared in the range of 2.5–1.9 V. This reaction, in which the valence of vanadium is tetravalent and trivalent, has been discussed in detail <sup>6, 7, 9, 10</sup>). Hence the reaction of  $V^{3+}/V^{2+}$  cannot be expected in the region of 1.0–4.5 V.

The cycle characteristics were evaluated under the rate of C/20 (first and second cycles) and the C/10 condition. The cycle characteristics of the 2<sup>nd</sup>, 10<sup>th</sup>, 20<sup>th</sup>, and 30<sup>th</sup> charge/discharge curves are shown in Fig. 3-4 and indicate that the cycle characteristics were not stable. The capacity in the range of 3.0–4.5 V was almost constant, but the capacity of the low-voltage region decreased as the cycle number increased. This was attributed to the disappearance of  $V^{3+}/V^{4+}$  reactions. The capacity retention of  $\alpha$ -LiVOPO<sub>4</sub> was good compared to the other phases but slightly worse than in previous reports <sup>10, 11</sup>).

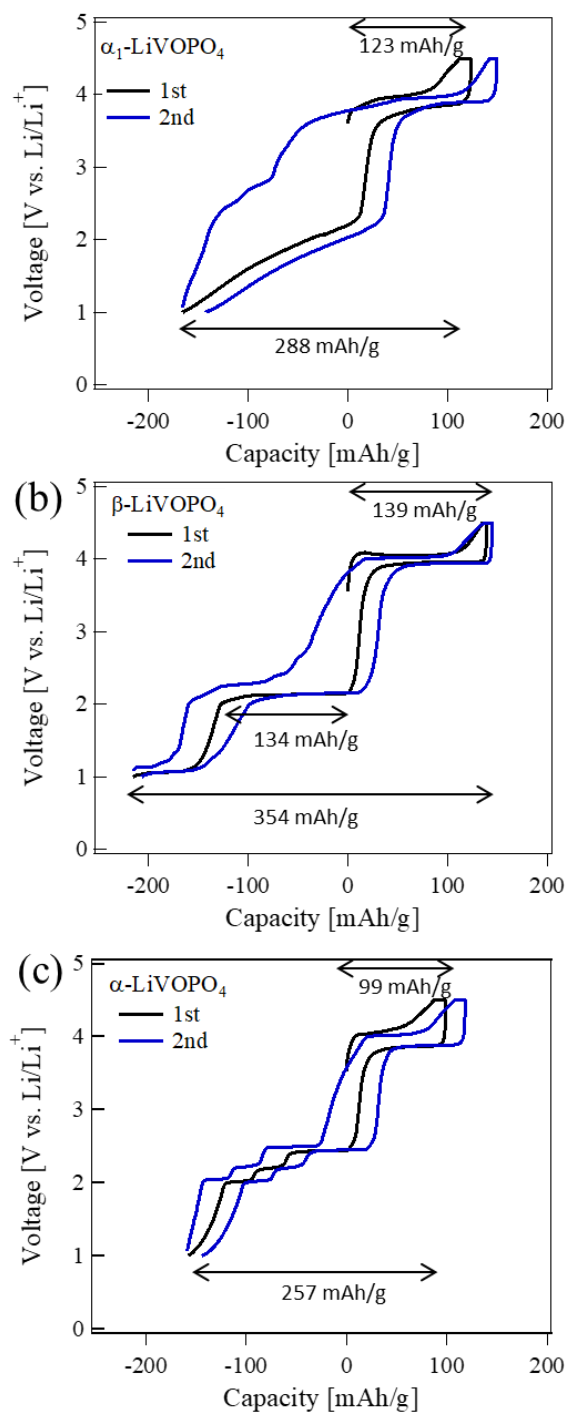


Fig. 3-3. First and second charge/discharge curves of  $\alpha_1\text{-LiVOPO}_4$  (a),  $\beta\text{-LiVOPO}_4$  (b), and  $\alpha\text{-LiVOPO}_4$  (c) in the range of 4.5–1.0 V at the rate of C/20.

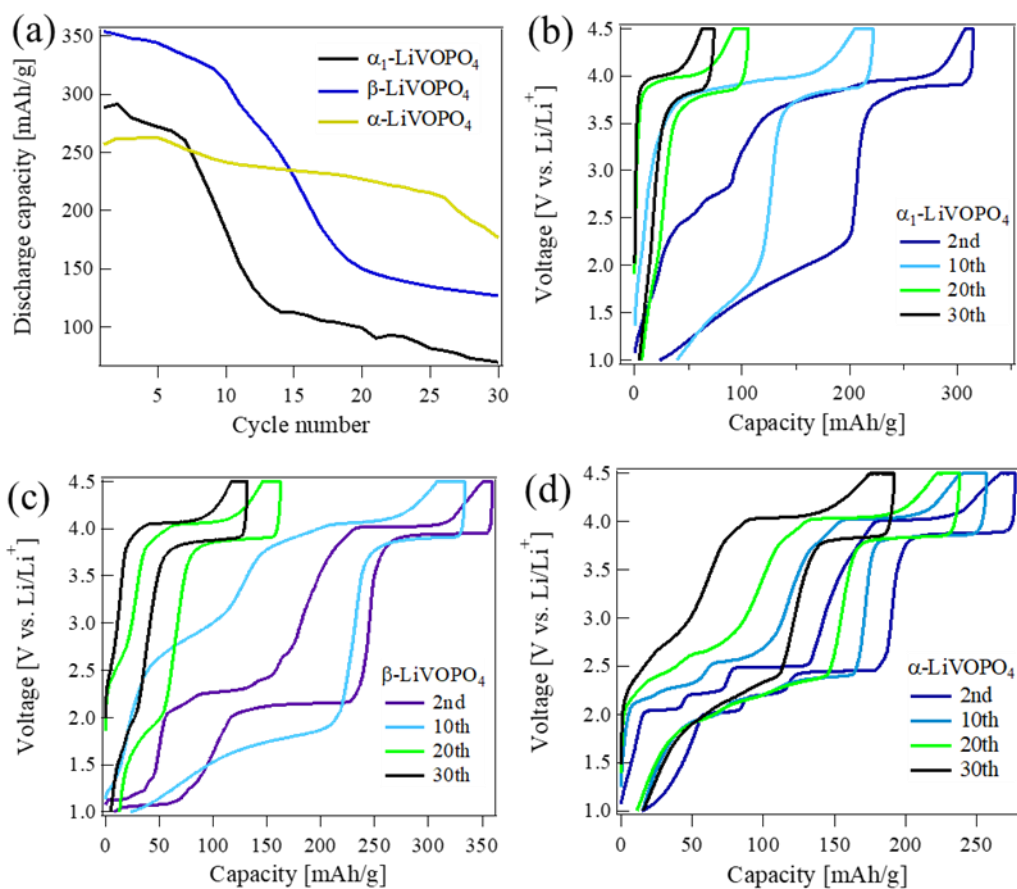


Fig. 3-4. Cycle characteristics of  $\alpha_1$ -LiVOPO<sub>4</sub>,  $\beta$ -LiVOPO<sub>4</sub>, and  $\alpha$ -LiVOPO<sub>4</sub> in the 4.5–1.0 V range at the rates of C/20 (first and second cycles) and C/10 (a). The 2<sup>nd</sup>, 10<sup>th</sup>, 20<sup>th</sup>, and 30<sup>th</sup> charge/discharge curves of  $\alpha_1$ -LiVOPO<sub>4</sub> (b),  $\beta$ -LiVOPO<sub>4</sub> (c), and  $\alpha$ -LiVOPO<sub>4</sub> (d).

### 3. 3. 2 Crystal evolution of LiVOPO<sub>4</sub> in charge/discharge

In order to understand the phase evolution of each LiVOPO<sub>4</sub> during charge/discharge, *operando* XRD was performed on an X-ray diffractometer equipped with Cu-K $\alpha_1$  radiation in transmission geometry, together with the charge/discharge data. The charging and discharging rate was C/10 in the voltage range of 3.5–4.8 V for the first charge, 4.8–1.0 V for the first discharge, and 1.0–3.9 V for the second charge. Every pattern was recorded in the 2 $\theta$  range of 10–36 ° every hour, corresponding to  $x = 0.1$  in Li <sub>$x$</sub> VOPO<sub>4</sub>. The results are shown in Fig. 3-5 ( $\alpha_1$ -LiVOPO<sub>4</sub>), Fig. 3-6 ( $\beta$ -LiVOPO<sub>4</sub>), and Fig. 3-7 ( $\alpha$ -LiVOPO<sub>4</sub>). Since there was not enough active material on the electrode, sufficient signal intensity could not be detected. We therefore discuss the whether the crystal structure evolution is two-phase or solid-solution behavior, based on changes in the main peak. If it was two-phase behavior, diffraction peaks from two kinds of crystal phase would be found simultaneously and no diffraction peak shifts would be found. If it was solid-solution behavior, on the other hand, a diffraction peak shift would be found.

Variations in the diffraction peaks of  $\alpha_1$ -LiVOPO<sub>4</sub> correspond to the results of *ex-situ* XRD reported by He *et al.*<sup>3)</sup>. The final diffraction pattern fully corresponded to the initial diffraction pattern. This suggests that the reaction is highly reversible even though the crystal structure changes dynamically. In the discharge from 4.8–1.0 V, the diffraction peak of  $\alpha_1$ -LiVOPO<sub>4</sub> decreases, that of  $\alpha_1$ -Li<sub>2</sub>VOPO<sub>4</sub> increases, and that of  $\alpha_1$ -LiVOPO<sub>4</sub> continues to appear distinctly up to 1.5 V. The state of structural change is clearly different between charging and discharging. In discharging, the diffraction peaks of  $\alpha_1$ -LiVOPO<sub>4</sub> and  $\alpha_1$ -Li<sub>2</sub>VOPO<sub>4</sub> can be distinguished as two-phase behavior. However, in charging from 1.0 V as the voltage increased, the shape of the peak collapsed, the full width at half maximum widened and gradually shifted to the high-angle side, indicating solid-solution behavior. It can be considered that the difference between Li<sup>+</sup> intercalation and deintercalation behaviors is associated with the difference in charge/discharge profiles in the low-voltage region. This supports two-phase behavior in low-voltage discharge as He *et al.* reported<sup>3)</sup>. However, it is solid-solution behavior in charging at low voltage.

Figure 3-6 shows the results of *operand* XRD for  $\beta$ -LiVOPO<sub>4</sub>. There are drastic changes in the XRD patterns as the amount of lithium changes. In the first charge, a peak

shift was not found and only diffraction peaks from each phases increase and decrease. This indicates two-phase behavior. In the first discharge, as the black arrows indicate, a diffraction peak shift is found in the latter half of the second plateau (2.1 V). The peak shift started after the  $\text{LiVOPO}_4$  peaks disappeared. After the peak shift (corresponding to the end of the second plateau), the peak location was not changed but the intensity started to decrease, and this diffraction peak disappeared at the third plateau. Ren *et al.* revealed that the crystal structure of discharging  $\beta\text{-LiVOPO}_4$  at 0.01 V changed to  $\text{Li}_2\text{O}$ , V and  $\text{Li}_3\text{PO}_4$  <sup>8)</sup>. However, we could not find such components, but two new weak peaks appeared at the  $2\theta$  region of 26–27 °. Due to low crystallinity, we did not know how to attribute the peaks. At least it could be said that, before  $\text{Li}_2\text{VOPO}_4$  decomposes to  $\text{Li}_2\text{O}$ , V and  $\text{Li}_3\text{PO}_4$  at 0.01 V, another crystal phases would exist. In the second charge, although an unknown peak was found at the lower plateau region as indicated by the black dashed arrow, the positions and behaviors of the other diffraction peaks agreed with those in discharging. Thus, unlike the case with  $\alpha_1\text{-LiVOPO}_4$ , the phase transition behaviors were the same in charging as in discharging. Therefore, in the charge/discharge curve, the plateau of low voltage appears at the same voltage during charging and discharging.

The results of *operando* XRD for  $\alpha\text{-LiVOPO}_4$  are shown in Fig. 3-7. The capacity of our  $\alpha\text{-LiVOPO}_4$  was half of theoretical capacity, so that the diffraction peaks of both  $\text{VOPO}_4$  and  $\alpha\text{-LiVOPO}_4$  appeared at 4.8 V. Considering the results of our previous study, lithium would perhaps not be deintercalate from large particles <sup>24)</sup>, and the diffraction peak of  $\alpha\text{-LiVOPO}_4$  would be from large particles. As shown in Fig. 3-3 (c), three peculiar plateaus appeared in the low-voltage region. As shown in Fig. 3-7, the plateau of 2.4 V ( $\text{LiVOPO}_4 \leftrightarrow \text{Li}_{1.5}\text{VOPO}_4$ ) indicates two-phase behavior, and the plateaus of 2.2 V ( $\text{Li}_{1.5}\text{VOPO}_4 \leftrightarrow \text{Li}_{1.75}\text{VOPO}_4$ ) and 2.0 V ( $\text{Li}_{1.75}\text{VOPO}_4 \leftrightarrow \text{Li}_2\text{VOPO}_4$ ) indicate solid-solution behavior because peak shifts occurred. These results agreed with that of previous report <sup>9)</sup>. In charging from 1.0 V, the crystal structure evolution was the same as in discharging. Therefore,  $\alpha\text{-LiVOPO}_4$  also exhibits plateaus at the same voltage in charging and discharging. Interestingly, because diffraction peaks of  $\alpha\text{-LiVOPO}_4$  clearly disappeared, unlike the case in 4.8 V charging, large particles also contribute to low-voltage charging/discharging.

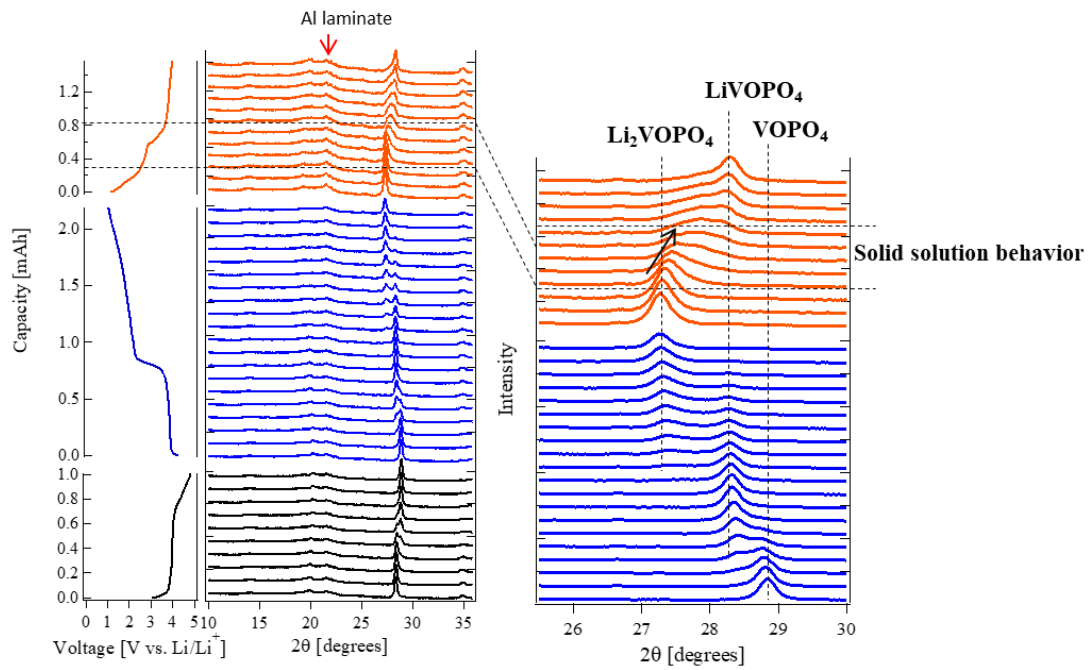


Fig. 3-5. *Operando* XRD patterns of  $\alpha_1$ -LiVOPO<sub>4</sub> with charge/discharge profiles at C/10 up to 4.8 V (left). An enlarged view of the 25.5–30° region of the first discharge and second charge. The dotted lines indicate the characteristic peak positions of the crystal phases.

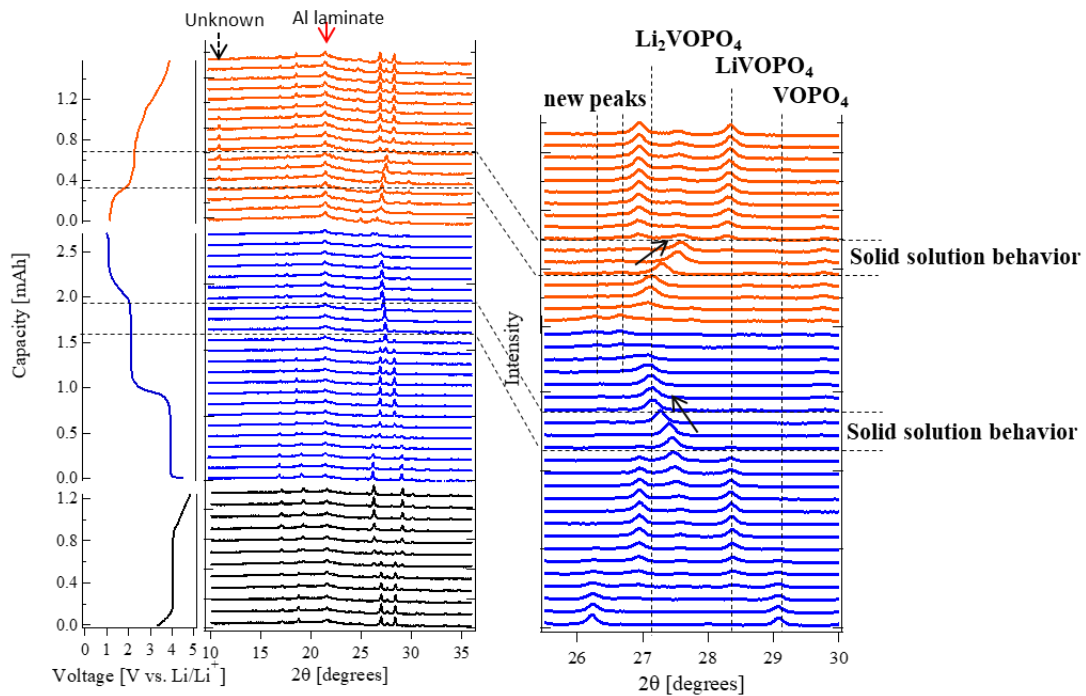


Fig. 3-6. *Operando* XRD patterns of  $\beta$ -LiVOPO<sub>4</sub> with charge/discharge profiles at C/10 up to 4.8 V (left). An enlarged view of the 25.5–30 ° region of the first discharge and second charge. The dotted lines indicate the characteristic peak positions of the crystal phases.

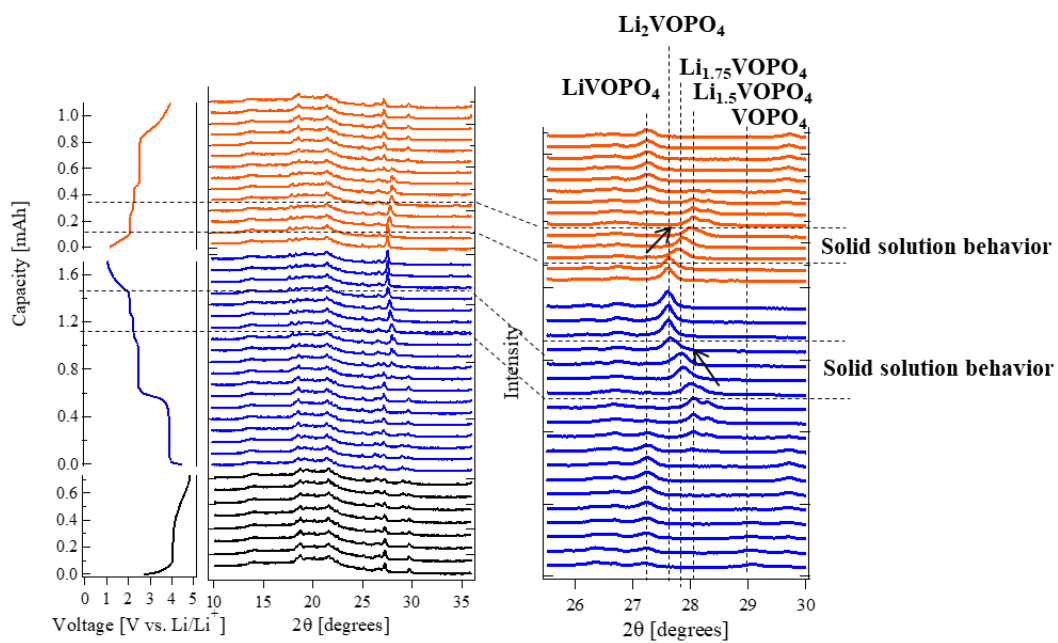


Fig. 3-7. *Operando* XRD patterns of  $\alpha$ - $\text{LiVOPO}_4$  with charge/discharge profiles at C/10 up to 4.8 V (left). Enlarged view of the 25.5–30° region of the first discharge and second charge. The dotted lines indicate the characteristic peak positions of the crystal phases.

### 3. 3. 3 Evaluation of valence of vanadium for LiVOPO<sub>4</sub> by XAFS

As mentioned above, the discharge capacities from 3.5–1.0 V of  $\alpha_1$ -LiVOPO<sub>4</sub> and  $\beta$ -LiVOPO<sub>4</sub> were larger than the theoretical capacity of LiVOPO<sub>4</sub> ( $V^{4+}$ )  $\leftrightarrow$  Li<sub>2</sub>VOPO<sub>4</sub> ( $V^{3+}$ ). On the other hand,  $\alpha$ -LiVOPO<sub>4</sub> exhibited the theoretical capacity even though the charge capacity from 3.5–4.5 V was 99 mAh/g. To explain this capacity from the viewpoint of charge compensation, information on the valence of vanadium at low voltage is needed. *Ex-situ* XAFS was performed to investigate the valence of vanadium in the low-voltage region and the results were compared with those of various vanadium oxides and vanadium metal as a standard valence. The results of the normalized XANES spectra of  $\alpha_1$ -LiVOPO<sub>4</sub>,  $\beta$ -LiVOPO<sub>4</sub>, and  $\alpha$ -LiVOPO<sub>4</sub> are shown in Fig. 3-8, Fig. 3-9, and Fig. 3-10, respectively. The pre-edge shape varied and energy shifts were seen, according to OCV changes. The pre-edge peak is due to the 1s  $\rightarrow$  3d transition, which is possible because of the O 2p and V 3d/4p hybrid orbit. The large pre-edge peak is attributable to the distortion of the VO<sub>6</sub> octahedra due to V=O<sup>6,7)</sup>. The pre-edge peak decreased as OCV decreased. This change trend of  $\beta$ -LiVOPO<sub>4</sub> and  $\alpha$ -LiVOPO<sub>4</sub> agreed with previous reports<sup>6,7)</sup>. From the results of the XANES absorption edge shift as shown in Fig.3-11, the valences of vanadium for  $\alpha_1$ -LiVOPO<sub>4</sub> and  $\beta$ -LiVOPO<sub>4</sub> at 1.5 V and for  $\alpha$ -LiVOPO<sub>4</sub> at 1.5 V and 1.0 V should be V<sup>+3</sup> because they corresponded to the absorption edge of V<sub>2</sub>O<sub>3</sub>. Although it is difficult to determine the absolute valences of vanadium at 1.0 V of  $\alpha_1$ -LiVOPO<sub>4</sub> and  $\beta$ -LiVOPO<sub>4</sub>, it can be said that it is sufficiently smaller than at least trivalent. This study revealed the vanadium valence behavior of  $\alpha_1$ -LiVOPO<sub>4</sub> in the low-voltage region using XAFS. He *et al.* reported the crystal structure of  $\alpha_1$ -Li<sub>2</sub>VOPO<sub>4</sub> using neutron and X-ray diffraction with Rietveld refinement. V–O bonding of  $\alpha_1$ -Li<sub>2</sub>VOPO<sub>4</sub> was longer than  $\alpha_1$ -LiVOPO<sub>4</sub>, and the summary of bond valence sums of vanadium for the vanadium coordination environment in  $\alpha_1$ -Li<sub>2</sub>VOPO<sub>4</sub> was trivalent<sup>3)</sup>. From our XANES results, the trivalent of vanadium was OCV at 1.5 V, and  $\alpha_1$ -LiVOPO<sub>4</sub> must finish changing to  $\alpha_1$ -Li<sub>2</sub>VOPO<sub>4</sub> at 1.5 V in discharging. This is supported by our *operando* XRD as shown in Fig. 3-5, where the crystal structure finished changing around 1.5 V. Additional lithium insertion from 1.5–1.0 V suggests that the framework of the crystal structure is not changing; rather, only the valence of vanadium changes. We tried to

estimate the valence of vanadium from the edge shift of XANES spectra. We attempted two ways to determine the vanadium absorption edge energy ( $E_0$ ).

(1) First derivative of normalized intensity

Normalized intensity was first-order differentiated, and the maximum value that appears after the pre-edge peak was taken as  $E_0$ . Figure 3-12 shows the result of the first derivative of normalized intensity for kinds of vanadium oxide and  $\text{LiVOPO}_4$ . The arrows in figures indicate  $E_0$  position. Even at 3.5 V, which is the initial state of  $\text{LiVOPO}_4$ , it can be confirmed that the profile differs slightly for each crystal phase. These are thought to be due to the crystal structure. Figure 3-13 shows the relationship between the valence of vanadium and  $E_0$ , and the valence of vanadium for each state of  $\text{LiVOPO}_4$  derived from the relationship. The linearity was confirmed by plotting the valence of vanadium oxide and  $E_0$ . The valence of  $\text{LiVOPO}_4$  in the table is calculated by putting  $E_0$  of  $\text{LiVOPO}_4$  measured at each voltage on this line.  $\beta$ - and  $\alpha_1$ - $\text{LiVOPO}_4$  can reproduce the tendency that the valence decreases from 1.5 V to 1.0 V, however,  $\alpha_1$ - $\text{LiVOPO}_4$  whose capacity at 1.0 V is lower than  $\beta$ -  $\text{LiVOPO}_4$  has a lower valence, and the correlation with the electrochemical characteristics is not sufficient.

(2) Normalized intensity at 0.4

Figure 3-14 shows the case where  $E_0$  is the energy at which the normalized XANES intensity is 0.4. This method also shows linearity between the valence of vanadium oxide and  $E_0$ . Similarly, as a result of calculating the valence of each  $\text{LiVOPO}_4$ , the valence of  $\text{LiVOPO}_4$  in the initial state shows  $\text{V}^{4+}$ . The valence of  $\beta$ - $\text{LiVOPO}_4$  at 1.0 V is slightly lower in terms of battery capacity. But the valence of  $\beta$ - $\text{LiVOPO}_4$  is lower than  $\alpha_1$ - $\text{LiVOPO}_4$  that the relationship about the valence between  $\beta$  and  $\alpha_1$  correlates with battery characteristics.

From these results, it is difficult to quantify the valence of vanadium strictly from XANES, but it can be said that the method of setting  $E_0$  at the position of absorbed intensity at 0.4 is more reliable.

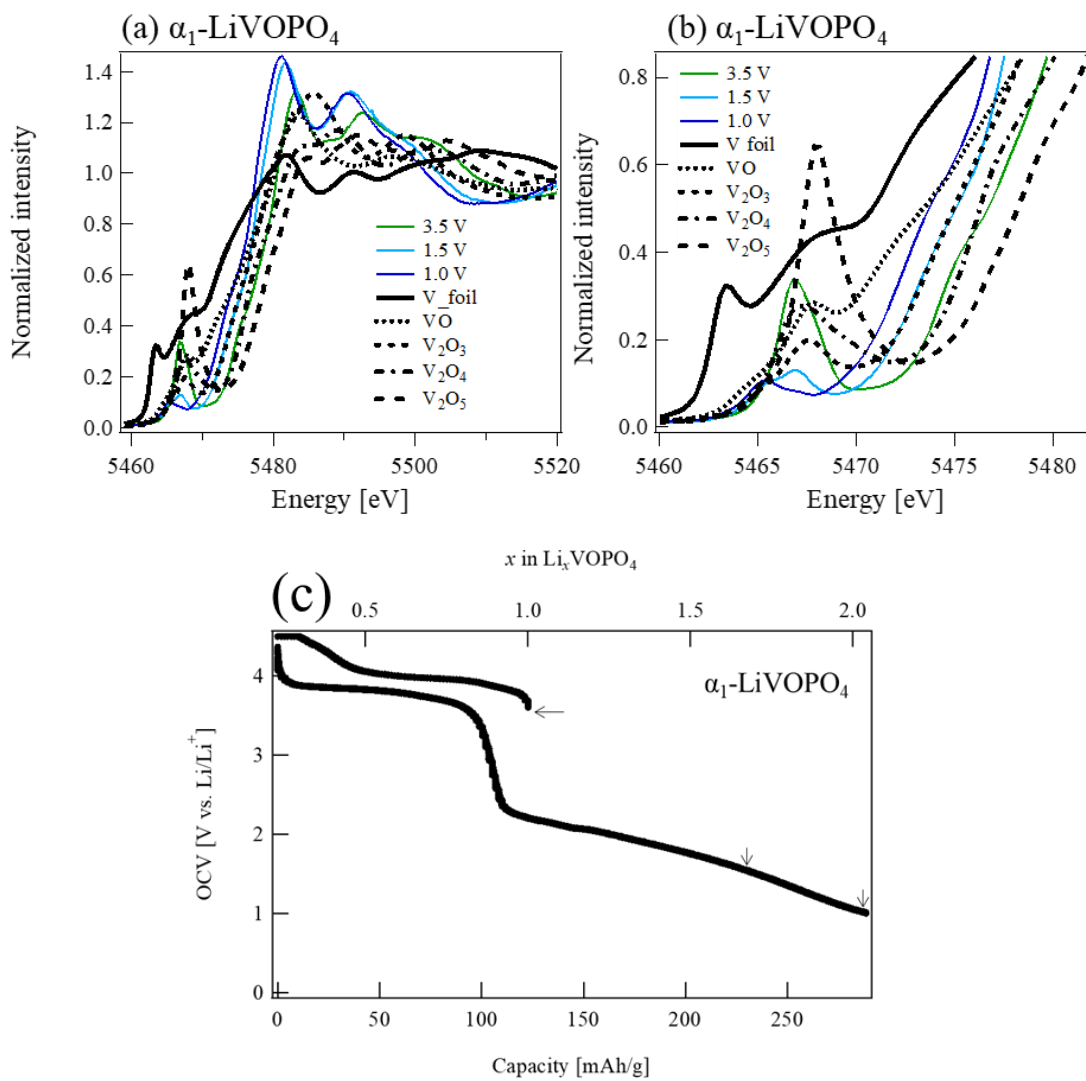


Fig. 3-8. Normalized V K-edge XANES spectra of  $\alpha_1$ -LiVOPO<sub>4</sub> (a), (b) at various states of OCV comparisons of various vanadium oxides and vanadium metal. (b) is enlarged views of the pre-edge peaks. Arrows in (c) indicate measured points.

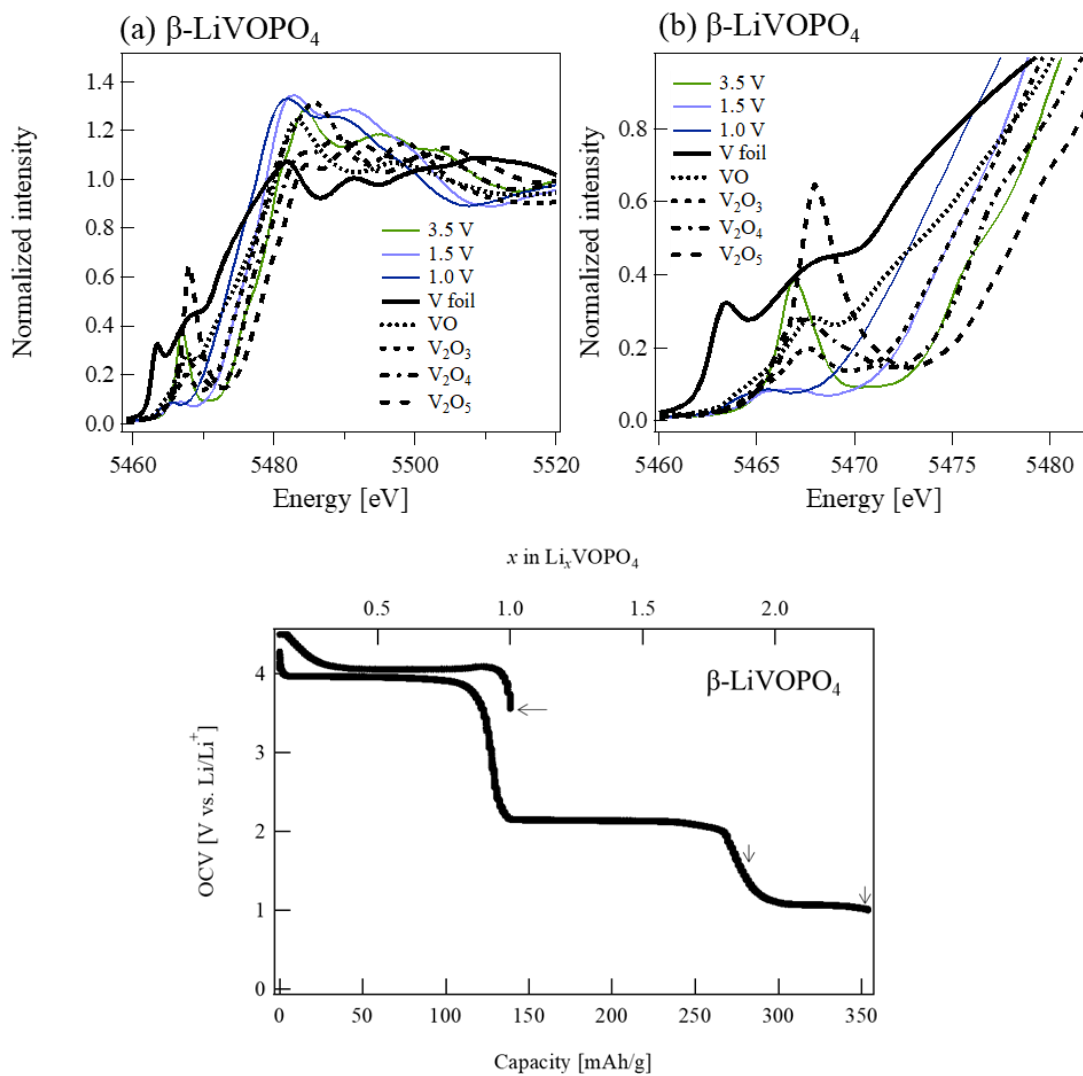


Fig. 3-9. Normalized V K-edge XANES spectra of  $\beta\text{-LiVOPO}_4$  (a), (b) at various states of OCV comparisons of various vanadium oxides and vanadium metal. (b) is enlarged views of the pre-edge peaks. Arrows in (c) indicate measured points.

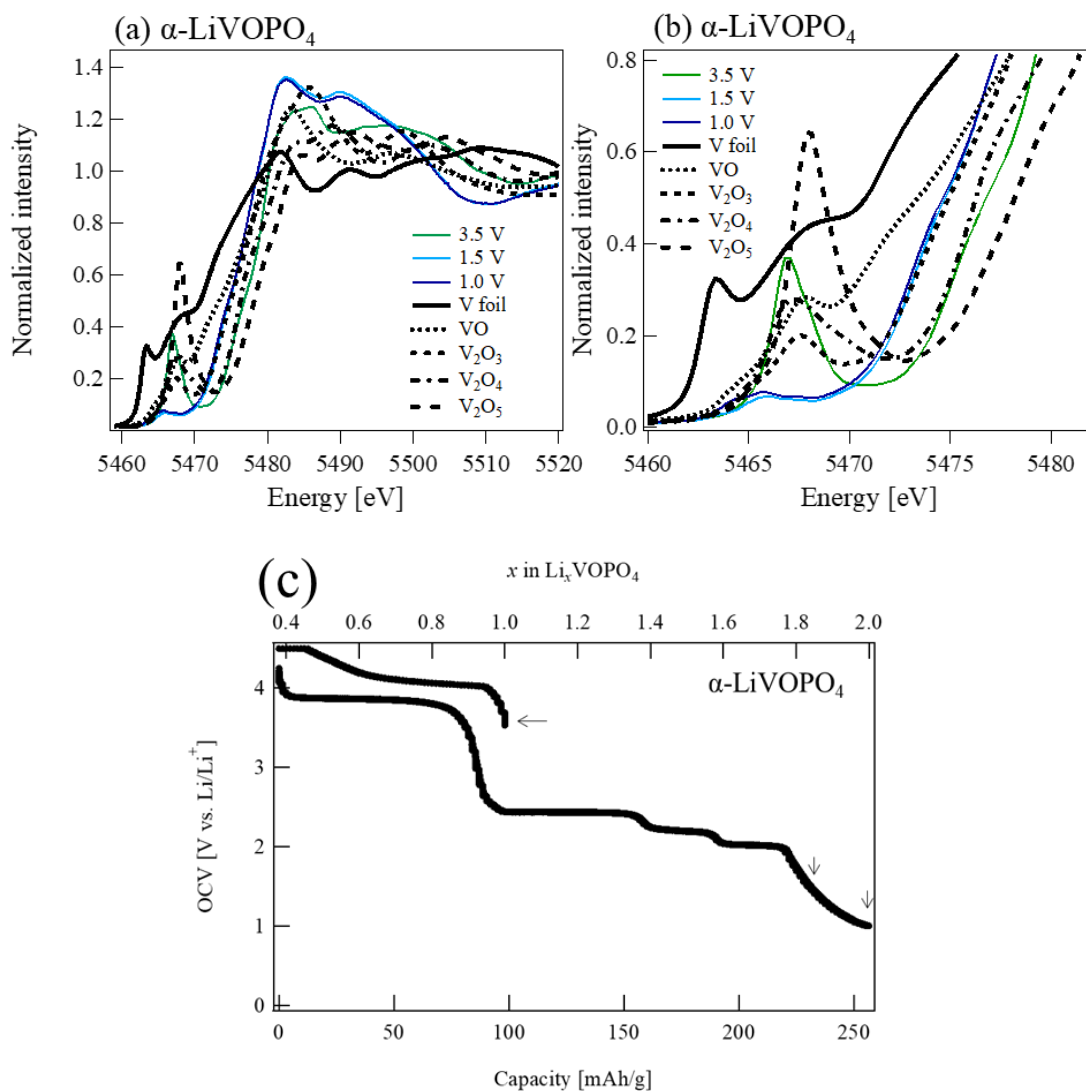


Fig. 3-10. Normalized V K-edge XANES spectra of  $\alpha$ -LiVOPO<sub>4</sub> (a), (b) at various states of OCV comparisons of various vanadium oxides and vanadium metal. (b) is enlarged views of the pre-edge peaks. Arrows in (c) indicate measured points.

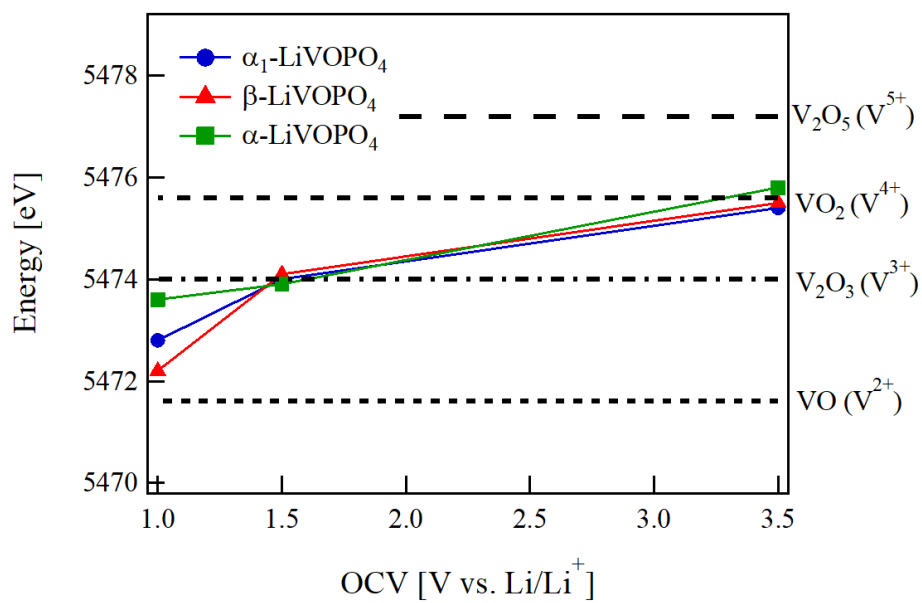


Fig. 3-11. XANES measured OCV and vanadium K-edge energy at 0.4 of the normalized intensity.

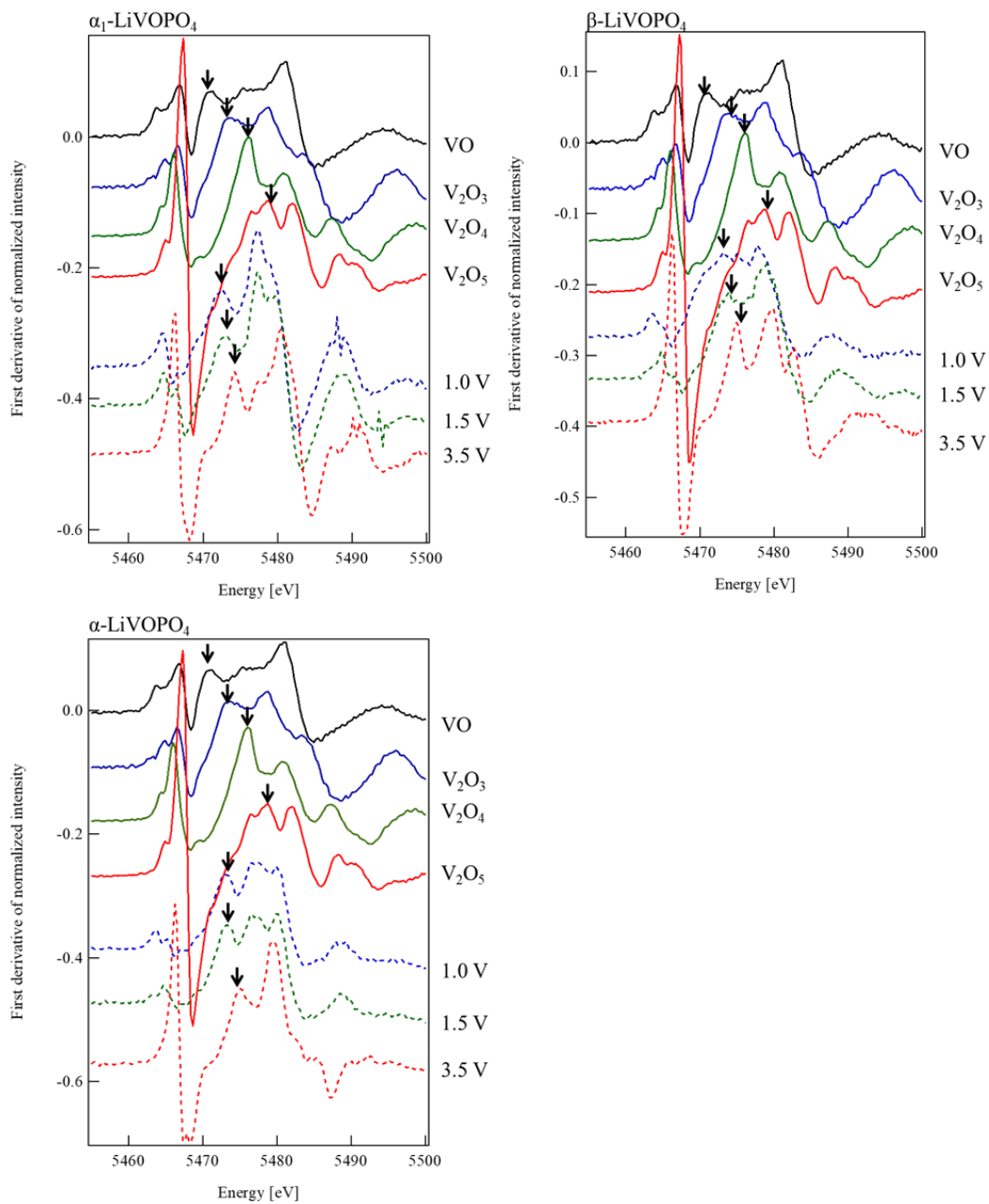


Fig. 3-12. The first derivative of normalized XANES intensity for kinds of vanadium oxide and LiVOPO<sub>4</sub>. The arrows in figures indicate the absorption edge position.

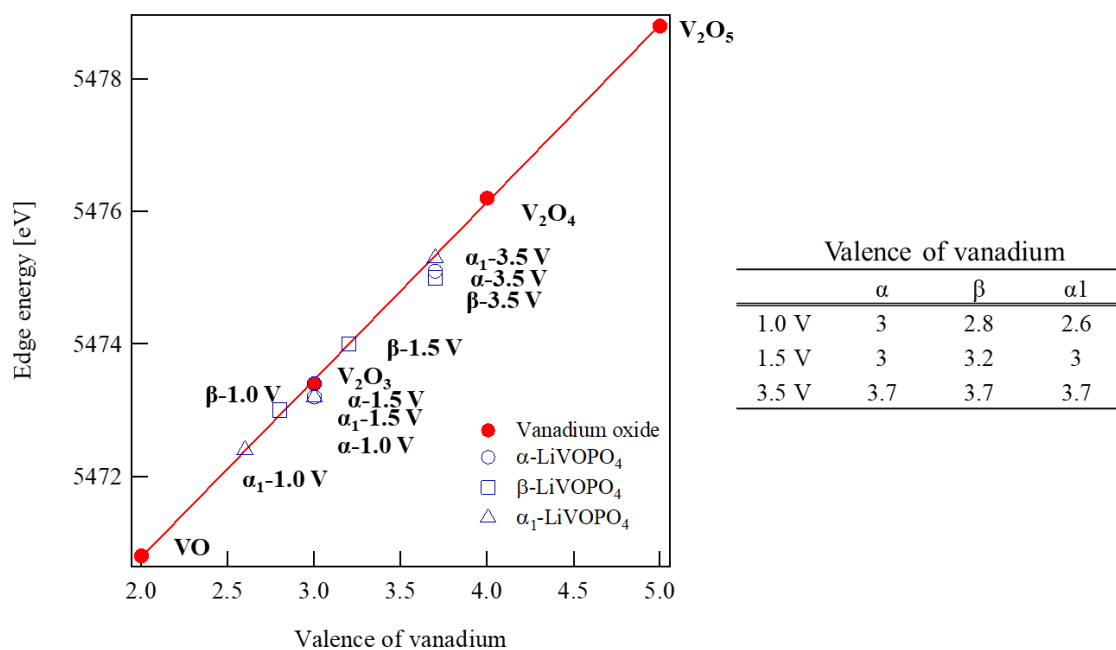


Fig. 3-13. The relationship between the valence of vanadium and the edge energy, and the valence of vanadium for each state of  $\text{LiVOPO}_4$  derived from the relationship. The edge energy is the maximum value of first derivative of normalized XANES intensity.

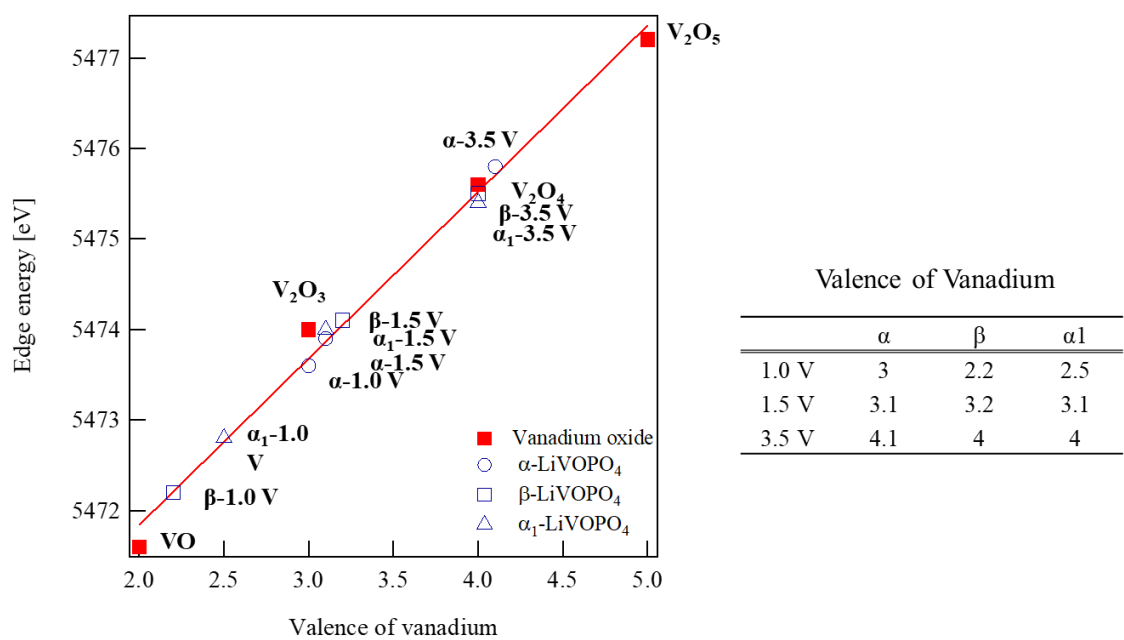


Fig. 3-14. The relationship between the valence of vanadium and the edge energy, and the valence of vanadium for each state of LiVOPO<sub>4</sub> derived from the relationship.

The edge energy is at 0.4 of normalized XANES intensity.

### 3. 3. 4 Thermal stability of LiVOPO<sub>4</sub>

The thermal stability of LiVOPO<sub>4</sub> was investigated using DSC. Figure 3-15 shows DSC profiles of  $\alpha_1$ -LiVOPO<sub>4</sub>,  $\beta$ -LiVOPO<sub>4</sub>,  $\alpha$ -LiVOPO<sub>4</sub>, and LiCoO<sub>2</sub> at 4.5 V charge and LiFePO<sub>4</sub> at 3.8 V charge. The DSC profiles of all LiVOPO<sub>4</sub> had the same shape and were similar to LiFePO<sub>4</sub>. All PO<sub>4</sub> tetrahedral corners of LiVOPO<sub>4</sub> are shared with VO<sub>6</sub> octahedra, which is different from the case with LiFePO<sub>4</sub>. LiFePO<sub>4</sub> shares one edge of PO<sub>4</sub> tetrahedra with FeO<sub>6</sub> octahedra. However, the difference in crystal structures is not related to thermal stability. Since both LiVOPO<sub>4</sub> and LiFePO<sub>4</sub> are composed of highly thermostable PO<sub>4</sub>, there is no oxygen release, so here is no clear difference in DSC profiles. Figure 3-16 shows the DSC profiles of LiVOPO<sub>4</sub> at 4.5 V charging and 1.0 V discharging. These profiles differ. It is difficult to discuss a strictly quantitative comparison of the total exothermic reaction enthalpy because the baseline and temperature range for calculating total exothermic enthalpy for each datum cannot always be constant. The exothermic enthalpy values are shown in Fig. 3-16 as reference values. The exothermic reaction enthalpy of LiVOPO<sub>4</sub> is small enough compared with LiCoO<sub>2</sub>. Although  $\alpha_1$ -,  $\beta$ -, and  $\alpha$ -LiVOPO<sub>4</sub> discharged down to 1.0 V have different crystal structures and amounts of Li, they all showed a similar slight exothermic reaction around 90 °C. Although we could not determine the reason for the exothermic reaction at 1.0 V of the profile around 90 °C, the exothermic reaction enthalpy is around 190 J/g at most, which is considered too low to reduce thermal stability. The high thermal stability of LiVOPO<sub>4</sub> is maintained even in the low-voltage region.

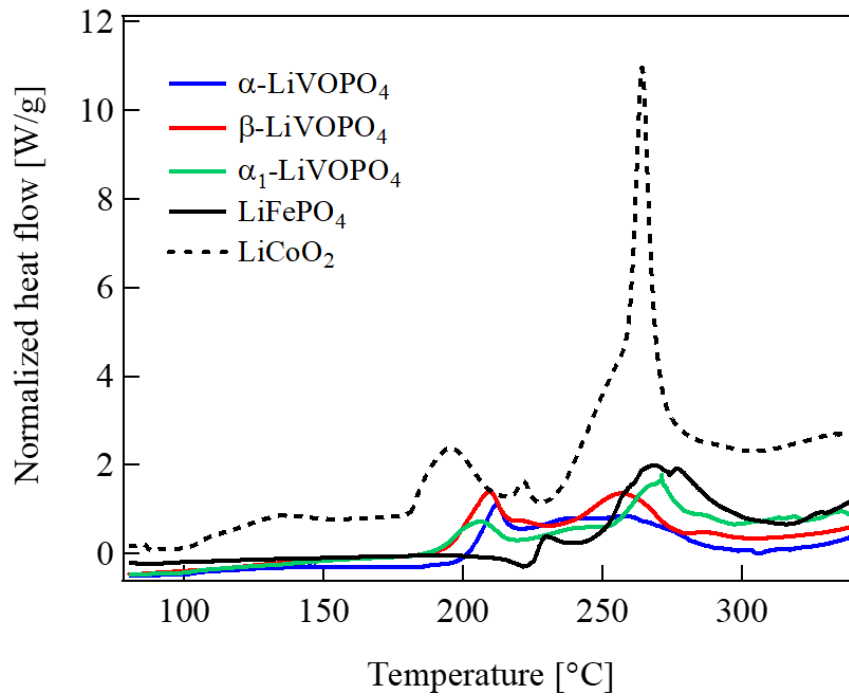


Fig. 3-15. DSC profiles of LiVOPO<sub>4</sub>, LiFePO<sub>4</sub>, and LiCoO<sub>2</sub> with electrolyte at a heating rate of 5 °C/min after 4.5 V charge for LiVOPO<sub>4</sub> and LiCoO<sub>2</sub>, and 3.8 V for LiFePO<sub>4</sub>.

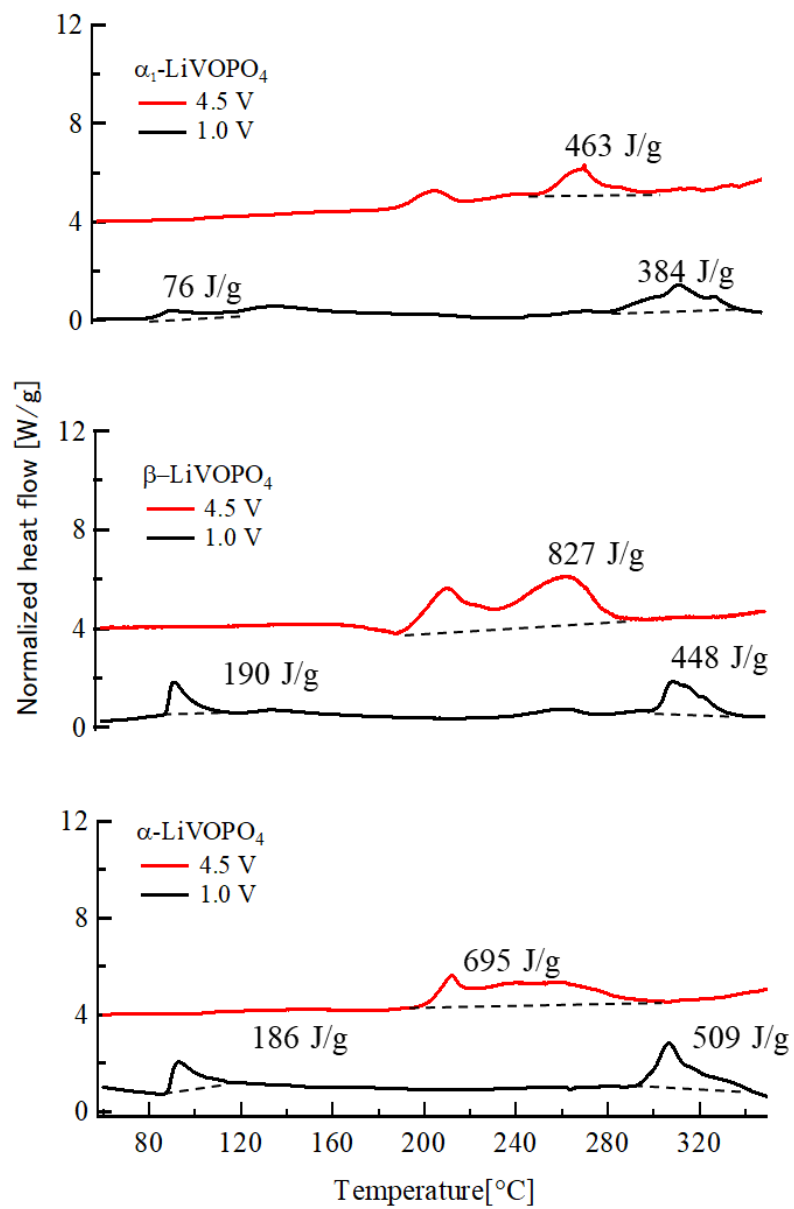


Fig. 3-16. DSC profiles of LiVOPO<sub>4</sub> at 4.5 V charging and 1.0 V discharging with electrolyte at a heating rate of 5 °C/min.

### 3. 4 Conclusions

$\alpha_1$ -,  $\beta$ -, and  $\alpha$ -LiVOPO<sub>4</sub> have been synthesized from the same precursor, and controlled subsequent sintering temperature. The capacities in the ranges of 3.5–4.5 V and 3.5–1.0 V differed. The capacity of the high-voltage region is influenced by the particle size, although the capacity of the low-voltage region was close to the theoretical capacity. Moreover,  $\alpha_1$ - and  $\beta$ -LiVOPO<sub>4</sub> exhibited beyond theoretical capacity in discharging to 1.0 V due to the decrease in the vanadium valence to below V<sup>3+</sup>. This was supported by *ex-situ* XANES analysis. *Operando* XRD determined whether the crystal structure evolution was solid-solution behavior or two-phase behavior during charging/discharging, and the difference in the charge/discharge profiles of  $\alpha_1$ -LiVOPO<sub>4</sub> was associated with crystal structure evolution. The thermal stability of LiVOPO<sub>4</sub> was demonstrated by DSC for the first time. The DSC profiles of LiVOPO<sub>4</sub> in the charging state were similar to that of LiFePO<sub>4</sub> and the total exothermic enthalpy were smaller than that of LiCoO<sub>2</sub>. Although the root cause could not be identified, the DSC profile of LiVOPO<sub>4</sub> at 1.0 V appeared as an exothermic reaction around 90 °C. However, it was not so large, and the total exothermic enthalpy from 80–350 °C was the same as that at 4.5 V charging. Since  $\alpha_1$ -,  $\beta$ -, and  $\alpha$ -LiVOPO<sub>4</sub> have high energy densities and high thermal stabilities, we conclude that they can be expected to serve not only as a next-generation polyanion cathode materials to replace LiFePO<sub>4</sub> but also as an anode materials with high thermal stability.

## Reference

- 1 M.Y. Saidi, J. Barker, H. Huang, J.L. Swoyer, and G. Adamson, *J. Power Sources*, **119-121** 266 (2003).
- 2 H. Huang, S.C. Yin, T. Kerr, N. Taylor, and L.F. Nazar, *Adv. Mater.*, **14** 1525 (2002).
- 3 G. He, C.A. Bridges, and A. Manthiram, *Chem. Mater.*, **27** 6699 (2015).
- 4 N.F. Quackenbush, L. Wangoh, D.O. Scanlon, R. Zhang, Y. Chung, Z. Chen, B. Wen, Y. Lin, J.C. Woicik, N.A. Chernova, S.P. Ong, M.S. Whittingham, and L.F.J. Piper, *Chem. Mater.*, **27** 8211 (2015).
- 5 Z. Chen, Q. Chen, L. Chen, R. Zhang, H. Zhou, N.A. Chernova, and M.S. Whittingham, *J. Electrochem. Soc.*, **160** A1777 (2013).
- 6 K.L. Harrison, C.A. Bridges, C.U. Segre, C.D. Varnado Jr., D. Applestone, C.W. Bielawski, M.P. Paranthaman, and A. Manthiram, *Chem. Mater.*, **26** 3849 (2014).
- 7 C.J. Allen, Q. Jia, C.N. Chinnasamy, S. Mukerjee, and K.M. Abraham, *J. Electrochem. Soc.*, **158** A1250 (2011).
- 8 M.M. Ren, Z. Zhou, and X.P. Gao, *J. Appl. Electrochem.*, **40** 209 (2010).
- 9 M. Bianchini, J.M. Ateba-Mba, P. Dagault, E. Bogdan, D. Carlier, E. Suard, C. Masquelierade, and L. Croguennec, *J. Mater. Chem. A*, **2** 10182 (2014).
- 10 Y.C. Lin, B. Wen, K.M. Wiaderek, S. Sallis, H. Liu, S.H. Lapidus, O.J. Borkiericz, N.F. Quachenbush, N.A. Chernova, K. Karki, F. Omenya, P.J. Chupas, L.F.J. Piper, M.S. Whittingham, K.W. Chapman, and S.P. Ong, *Chem. Mater.*, **28** 1794 (2016).
- 11 H. Zhou, Y. Shi, F. Xin, F. Omenya, and M.S. Whittingham, *Appl. Mater. Interfaces*, **9** 28537 (2017).
- 12 X.H. Rui, N. Yesibolati, and C.H. Chen, *J. Power Sources*, **199** 2279 (2011).
- 13 G. Hautier, A. Jian, S.P. Ong, B. Kang, C. Moore, R. Doe, and G. Ceber, *Chem. Mater.*, **23** 3495 (2011).
- 14 N. Dupre, G. Wallez, J. Gaubicher, and M. Quarton, *J. Solid State Chem.*, **117** 2896 (2004).
- 15 A.S. Hameed, M. Nagarathinam, M.V. Reddy, B.V.R. Chowdan, and J.J. Vittal, *J. Mater. Chem.*, **22** 7206 (2012).
- 16 J. Barker, M.Y. Sadi, and J.L. Swoyer, *J. Electrochem. Soc.*, **151** A796 (2004).

- 17 B.M. Azmi, T. Ishihara, H. Nishiguchi, and Y. Takita, *J. Power Sources*, **146** 525 (2005).
- 18 M.M. Ren, Z. Zhou, L.W. Su, and X.P. Gao, *J. Power Sources*, **189** 786 (2009).
- 19 L. Wang, L. Yang, L. Gong, X. Jiang, K. Yuan, and Z. Hu, *Electrochim. Acta*, **56** 6906 (2011).
- 20 Y. Yang, H. Fang, J. Zheng, L. Li, G. Li, and G. Yan, *Solid State Sci.*, **10** 1292 (2008).
- 21 A. Tang, J. Shen, Y. Hu, G. Xu, D. He, Q. Yi, and R. Peng, *J. Electrochem. Soc.*, **161** A10 (2014).
- 22 Z. Liu, Z. Su, and H. Tian, *Ceram. Int.*, **44** 9372 (2018).
- 23 K. Saravanan, H.S. Lee, M. Kuezma, J.J. Vittal, and P. Balaya, *J. Mater. Chem.*, **21** 10042 (2011).
- 24 A. Nojima, A. Sano, S. Fujita, K. Ohtsuki, and S. Okada, *J. Electrochem. Soc.*, **166** A3731 (2019).
- 25 B. Ravel and M. Newville, *J. Synchrotron Radiat.*, **12** 537 (2005).
- 26 [http://www.astf-kha.jp/synchrotron/en/userguide/gaiyou/bl5s1i\\_xxafs.html](http://www.astf-kha.jp/synchrotron/en/userguide/gaiyou/bl5s1i_xxafs.html)

# Chapter 4

## **Bipolar battery using $\text{LiVOPO}_4$**

#### 4. 1 Introduction

As described in Chapters 2 and 3,  $\text{LiVOPO}_4$  is an attractive material with high potential. In this study, an experimental cell using Li metal has been used to evaluate  $\text{LiVOPO}_4$ , but in an actual lithium secondary battery, graphite must be used. In addition, as shown in Chapter 3,  $\text{LiVOPO}_4$  has potential as an anode active material. For example, it is possible to produce a battery composed of  $\text{LiVOPO}_4$  for both cathode and anode, which can be expected to reduce both material and manufacturing costs. In the case of a graphite system, there is a risk that the Cu of the current collector could dissolve by the voltage of anode increase during overdischarge, and the dissolved Cu would then be deposited on the anode surface and short-circuited during recharging. Batteries built only with  $\text{LiVOPO}_4$  do not have such a risk, so the risk of swelling and firing is small even if the built-in device is not used for a long time and reaches an overdischarged state. The number of materials with bipolar properties is limited, and this high-safety and easy-to-manufacture  $\text{LiVOPO}_4$  feature should be applied to bipolar batteries.  $\text{Li}_3\text{V}_2(\text{PO}_4)_3$  also has a potential for bipolar cells, and Mao *et al.* provided an example of a bipolar cell from both fabrication and evaluation <sup>1)</sup>.

In this chapter we describe the results of the fabrication and evaluation of bipolar cells combining  $\text{LiVOPO}_4$  of each crystal phase.

## 4. 2 Experimental

Electrodes using  $\text{LiVOPO}_4$  of each crystal phase were prepared in the same way as in Chapter 3. Electrodes were fabricated by casting the slurry, which was made from downsized and carbon-coated  $\text{LiVOPO}_4$  and PVdF at a weight ratio of 92:8 in NMP. The active material was around  $6 \text{ mg/cm}^2$  on Al foil. The cathode was then punched into a disc with an active area of about  $1.13 \text{ cm}^2$ . Cells were assembled in a dry room in which the dewpoint was  $-40 \text{ }^\circ\text{C}$  in order to remove the influence of moisture mixing. Removal of the coating on the excess part, formation of a tab, and connection to the Al lead by ultrasonic welding are shown in Fig. 4-1. As the figure shows, an Al laminate film was used for the outer package, and the integrated lead and electrode were arranged orthogonally to each other. Between the electrodes, a separator (2400, Celgard) was set. The Al laminate was then folded at the center of the Al laminate and heat-pressed on the sealant with an impulse sealer (Fuji Impulse Corp.). After drying at  $80^\circ\text{C}$  for 12 hours in a vacuum dryer, the electrolyte was injected. As an electrolyte, 1 M of  $\text{LiPF}_6$  in a solution of ethylene carbonate (EC) and diethyl carbonate (DEC; volume ratio of EC:DEC = 3:7) was used. After the injection, the bipolar Al laminate cell was completed by sealing the other side.

Charge/discharge testing was performed by a battery charge/discharge system (SM-8, Hokuto Denko) at room temperature. Similar to the results in Chapter 3, the capacity is higher on the low-voltage side in any crystal phase. Therefore, since the coating weight is the same for both the cathode and the anode, and the anode capacity is always higher than that of the cathode, it seems that Li deposition on the anode surface does not occur. By limiting the discharge cutoff voltage at 0 V, it can be considered that lithium ions contributing to charge/discharge are released from the cathode. The battery characteristics were evaluated for rate characteristics and cycle characteristics in the voltage range of 2.5 to 0.0 V. The charge condition was CC-CV charge (C/50 cutoff) and the discharge condition was CC discharge. The C rate was the same for charge and discharge. The first 5 cycles were performed at C/20, then the C rate was increased and each cycle was performed 5 times, and finally C/20 was performed for 5 cycles again.

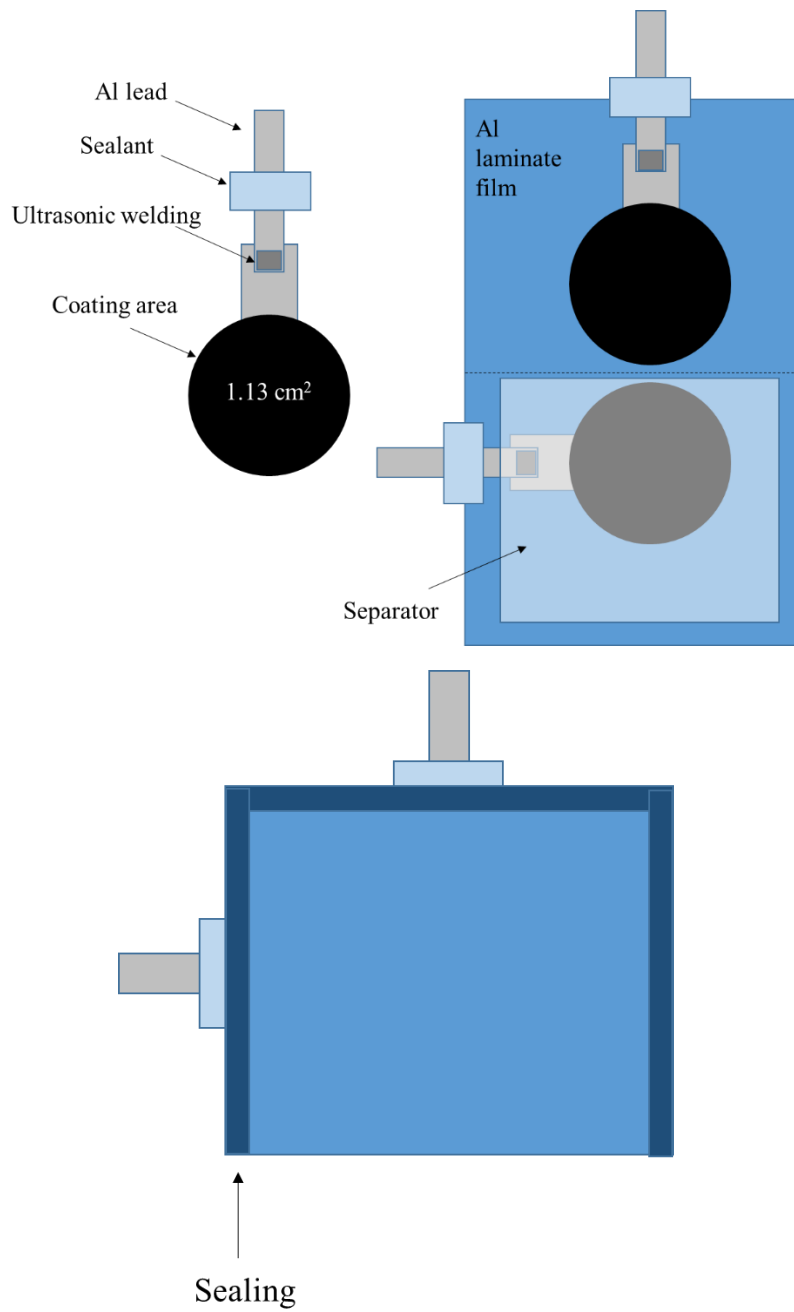


Fig. 4-1 Bipolar Al laminate cell

### 4.3 Results and discussion

Figures 4-2, 4-3, and 4-4 show the charge/discharge curves at various C rates; the cathode is fixed to  $\alpha_1$ -LiVOPO<sub>4</sub>,  $\beta$ -LiVOPO<sub>4</sub>, and  $\alpha$ -LiVOPO<sub>4</sub>, respectively, and the anode is changed to LiVOPO<sub>4</sub> of each crystal phase. Table 4-1 shows the capacity and initial efficiency of each cell. The results of the cycle performance of the cathode are fixed to  $\alpha_1$ -LiVOPO<sub>4</sub>,  $\beta$ -LiVOPO<sub>4</sub>, and  $\alpha$ -LiVOPO<sub>4</sub>, as shown in Figs. 4-5, 4-6, and 4-7, respectively.

As shown in Chapter 2, the charge and discharge curves of each crystal phase in the voltage range of 2.8 to 4.5 V (vs. Li/Li<sup>+</sup>) are the same, but the profiles in bipolar cells are different. This is because the profile of each crystal phase as an anode is different. In fact, it can be seen that the profiles of cells having different crystal phases in the cathode and the same crystal phase in the anode are almost the same. Since the charge/discharge profiles of each cathode are basically the same regardless of the phase, there is a difference in capacity under low C rate conditions depending on the cathode as shown in figures 4-8, 4-9, and 4-10. That is, the charging depth for the anode differ in which phase of LiVOPO<sub>4</sub> is selected. For example, since  $\beta$ -LiVOPO<sub>4</sub> has the largest capacity among the three phases, the opposing anode will accept more lithium. The following points were noted from the results of these combinations.

(1)  $\alpha_1$ -LiVOPO<sub>4</sub> is not suitable for an anode

All the charge/discharge profiles using  $\alpha_1$ -LiVOPO<sub>4</sub> as the anode show very large polarization. Moreover, the initial efficiency is the lowest regardless of which crystal phase is used for the cathode. As shown in Chapter 2, the initial efficiency of the cathode is 93% or more in any crystal phase. Nevertheless, the low initial efficiency can be attributed to the large hysteretic voltage profile of  $\alpha_1$ -LiVOPO<sub>4</sub> as an anode.

(2) There is no cycle degradation, as was the case in Chapter 3

As shown in Fig. 3-4 (a), the cycle performances are low in the voltage range of 1.0 – 4.5 V (vs. Li/Li<sup>+</sup>). However, all levels have 80% or more capacity retention, and  $\beta$ -LiVOPO<sub>4</sub> and  $\alpha$ -LiVOPO<sub>4</sub> are more than 90%. Considering the capacity of the cathode, the voltage of the anode is considered to be about 1.5 V (vs. Li/Li<sup>+</sup>). Considering previous reports, the cycle performance may be good if not used up to

1.0 V (vs. Li/Li<sup>+</sup>)<sup>2,3</sup>).

- (3) The initial efficiency is poor when  $\alpha$ -LiVOPO<sub>4</sub> is the cathode.

As Table 4-1 shows, the level using  $\alpha$ -LiVOPO<sub>4</sub> for the cathode tends to have poor initial efficiency. However, the discharge capacity is not far from the value shown in Table 2-2. Namely, the charging capacity is higher than that of the half cell. Looking at the charge/discharge profiles shown in Fig. 4-4 (a), the inflection point near 1.8 V, which is characteristic of the  $\alpha$ -LiVOPO<sub>4</sub> anode, is seen except during the first discharge. The inflection point appears around 1.8 V in the subsequent low-rate charge/discharge profile. From this, it is considered that the charge capacity apparently increased due to some side reaction occurring in the initial charge.

- (4) The performance of  $\beta$ -LiVOPO<sub>4</sub> as an anode is comparable to that of  $\alpha$ -LiVOPO<sub>4</sub>.

Even if the cycle characteristics and rate characteristics are compared, the capacity retention is comparable, so the characteristics of these two phases as anodes are considered comparable.

Based on these results, the combination of  $\beta$ -LiVOPO<sub>4</sub> for the cathode and  $\alpha$ -LiVOPO<sub>4</sub> for the anode is considered suitable as a battery, as is that of  $\beta$ -LiVOPO<sub>4</sub> for both the cathode and the anode.

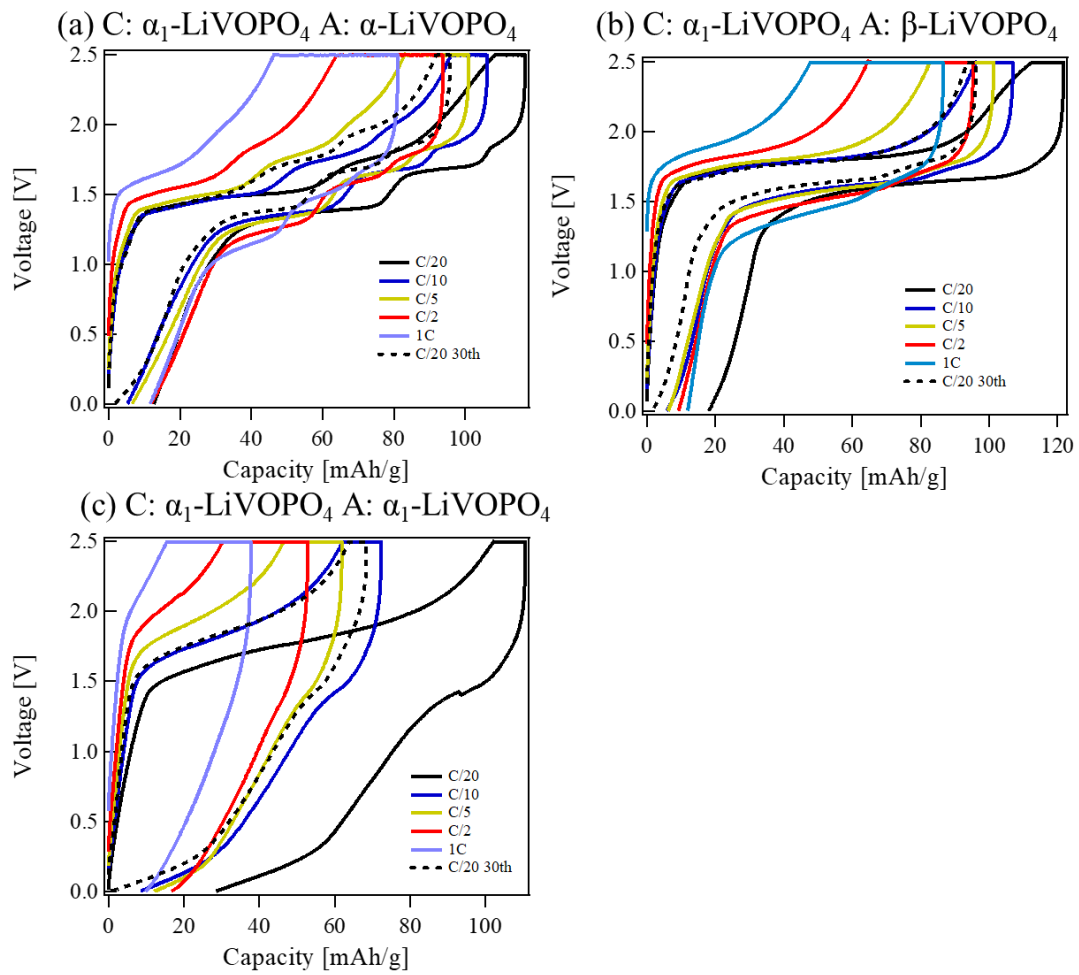


Fig. 4-2. Charge/discharge curves of a bipolar cell at various C rates. The cathode is fixed to  $\alpha_1$ -LiVOPO<sub>4</sub>. The anode is  $\alpha$ -LiVOPO<sub>4</sub> (a),  $\beta$ -LiVOPO<sub>4</sub> (b), and  $\alpha_1$ -LiVOPO<sub>4</sub>

(c).

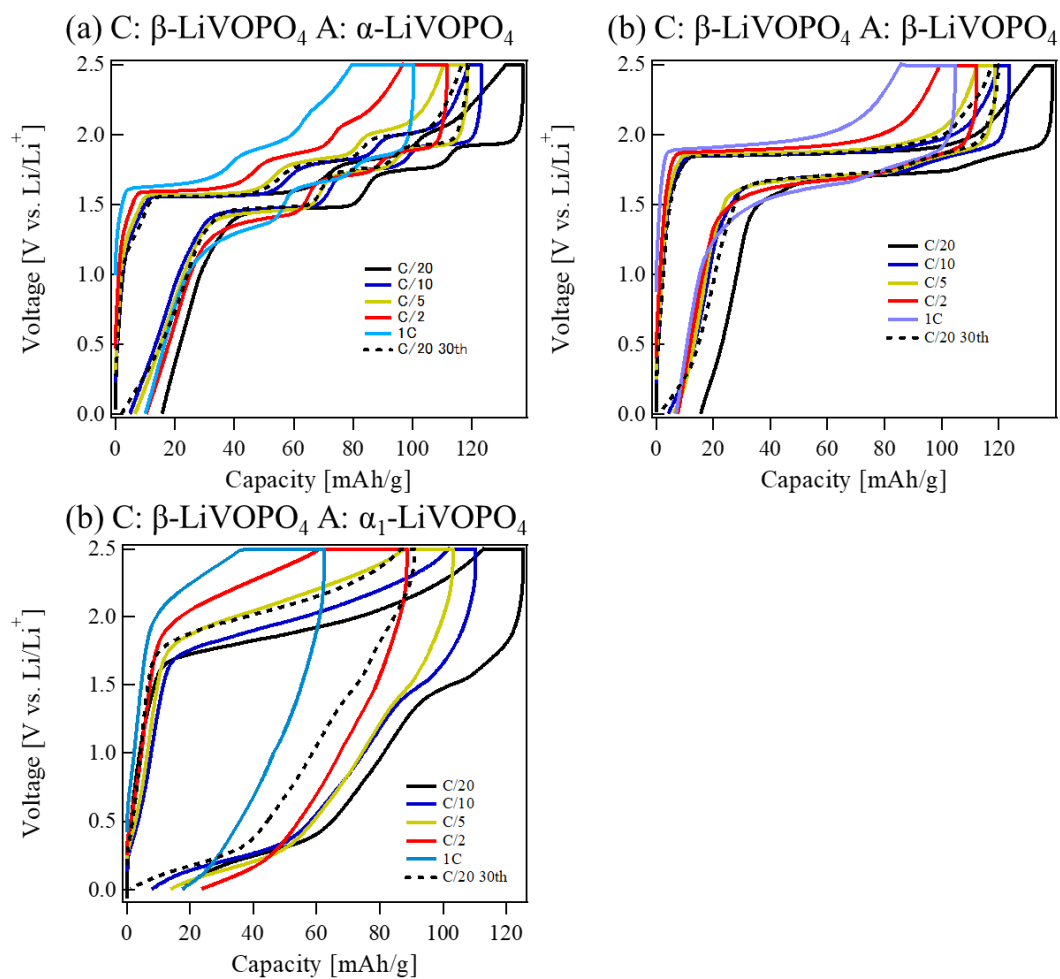


Fig. 4-3. Charge/discharge curves of a bipolar cell at various C rates. The cathode is fixed to  $\beta$ -LiVOPO<sub>4</sub>. The anode is  $\alpha$ -LiVOPO<sub>4</sub> (a),  $\beta$ -LiVOPO<sub>4</sub> (b), and  $\alpha_1$ -LiVOPO<sub>4</sub> (c).

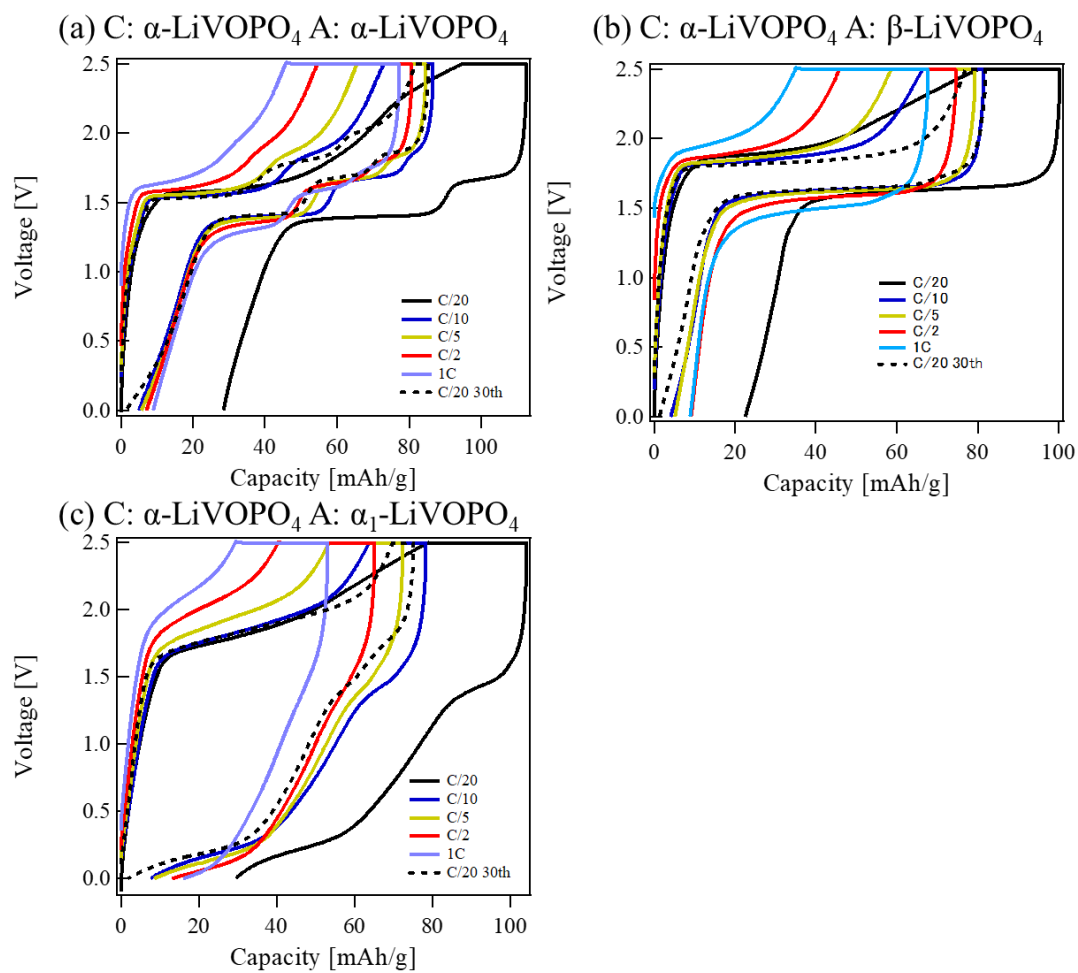


Fig. 4-4. Charge/discharge curves of a bipolar cell at various C rates. The cathode is fixed to  $\alpha$ -LiVOPO<sub>4</sub>. The anode is  $\alpha$ -LiVOPO<sub>4</sub> (a),  $\beta$ -LiVOPO<sub>4</sub> (b), and  $\alpha_1$ -LiVOPO<sub>4</sub> (c).

Table 4-1. The charge/discharge capacities of a bipolar cell; the cathode is fixed to  $\alpha_1$ -LiVOPO<sub>4</sub> (a),  $\beta$ -LiVOPO<sub>4</sub> (b), and  $\alpha$ -LiVOPO<sub>4</sub> (c).

(a)

Cathode/Anode	$\alpha_1/\alpha$		$\alpha_1/\beta$		$\alpha_1/\alpha_1$	
Initial efficiency	89%		85%		74%	
Capacity[mAh/g]	Charge	Discharge	Charge	Discharge	Charge	Discharge
C/20	117	104	122	104	111	82
C/10	101	99	102	99	62	61
C/5	94	92	95	93	51	52
C/2	81	79	86	84	38	37
1C	69	68	74	72	27	26
C/20 30cycs	96	94	96	95	68	68
Retention	82%	90%	79%	91%	62%	83%

(b)

Cathode/Anode	$\beta/\alpha$		$\beta/\beta$		$\beta/\alpha_1$	
Initial efficiency	89%		89%		86%	
Capacity[mAh/g]	Charge	Discharge	Charge	Discharge	Charge	Discharge
C/20	137	121	139	123	125	108
C/10	119	117	119	118	104	102
C/5	112	110	112	111	89	88
C/2	100	99	104	104	62	62
1C	90	89	97	96	40	38
C/20 30cycs	118	116	120	119	91	90
Retention	86%	96%	86%	96%	73%	83%

(c)

Cathode/Anode	$\alpha/\alpha$		$\alpha/\beta$		$\alpha/\alpha_1$	
Initial efficiency	75%		78%		72%	
Capacity[mAh/g]	Charge	Discharge	Charge	Discharge	Charge	Discharge
C/20	113	84	100	78	104	75
C/10	84.5	81.9	79.7	77.6	72.8	70.0
C/5	81	79	75	73	65	63
C/2	74	73	67	65	52	51
1C	70	67	59	57	37	36
C/20 30cycs	85	84	82	81	75	73
Retention	76%	100%	82%	104%	72%	98%

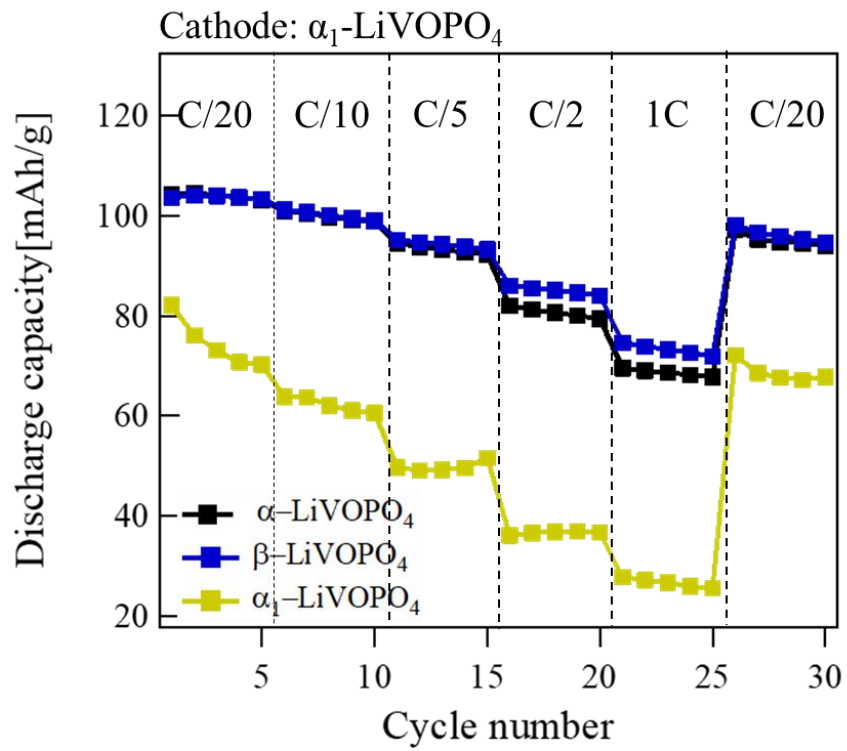


Fig. 4-5. Cycle performance of bipolar cells. The cathode is fixed to  $\alpha_1$ -LiVOPO<sub>4</sub>.

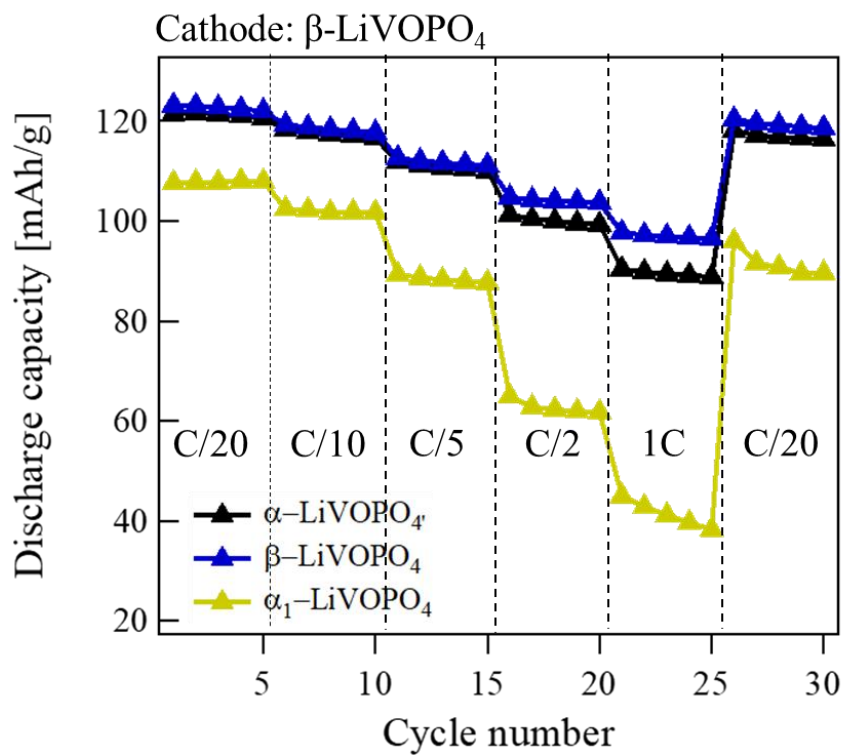


Fig. 4-6. Cycle performance of bipolar cells. The cathode is fixed to  $\beta\text{-LiVOPO}_4$ .

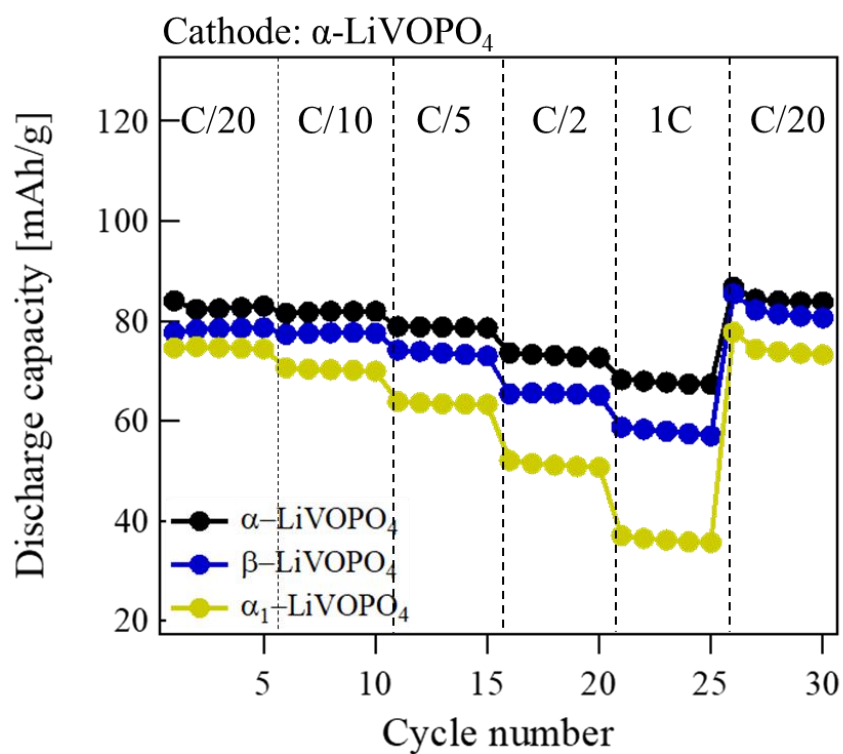


Fig. 4-7. Cycle performance of bipolar cells. The cathode is fixed to  $\alpha$ -LiVOPO<sub>4</sub>.

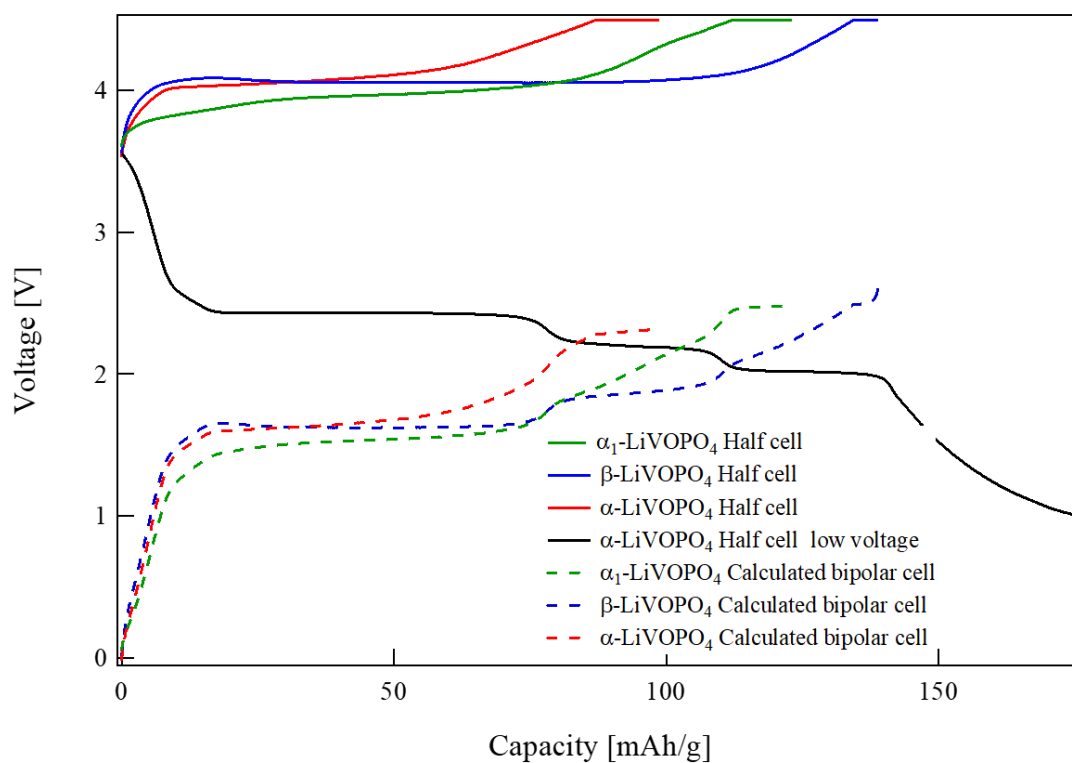


Fig. 4-8. Half cells of charge profile for each crystal phase and of discharge profile for  $\alpha$ -LiVOPO<sub>4</sub>. The dash lines are calculated charge profiles of bipolar cell using  $\alpha$ -LiVOPO<sub>4</sub> as the anode.

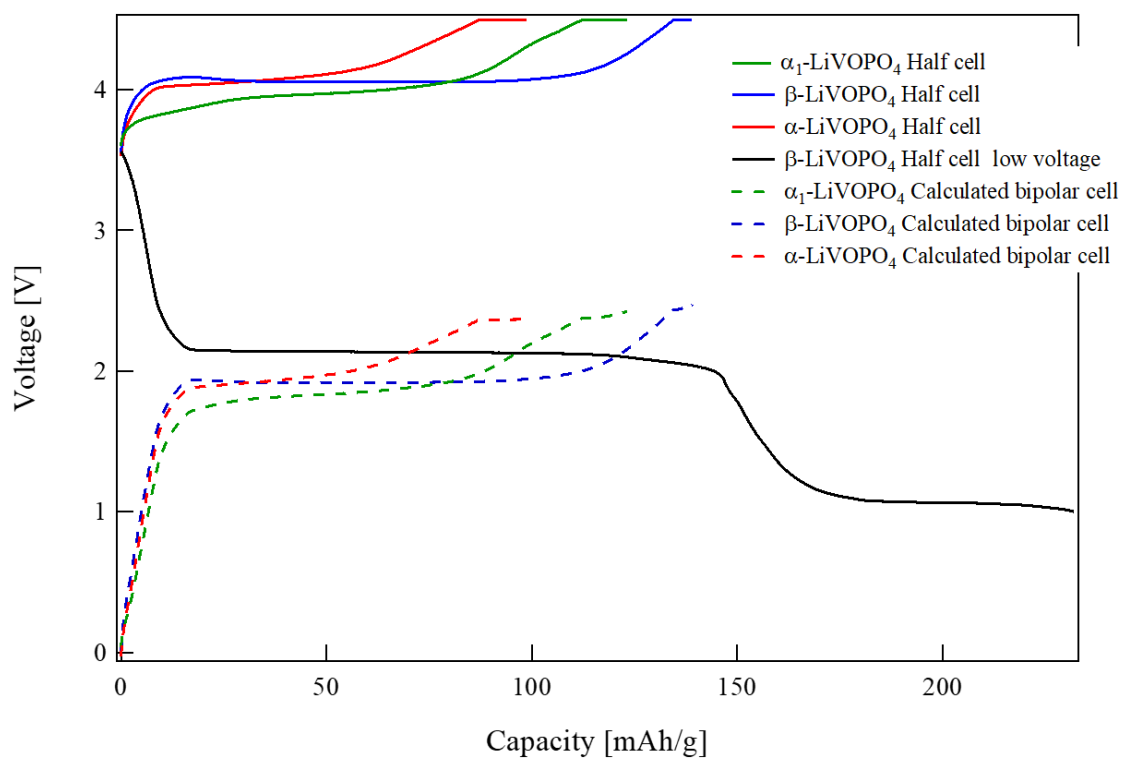


Fig. 4-9. Half cells of charge profile for each crystal phase and of discharge profile for  $\beta$ -LiVOPO<sub>4</sub>. The dash lines are calculated charge profiles of bipolar cell using  $\beta$ -LiVOPO<sub>4</sub> as the anode.

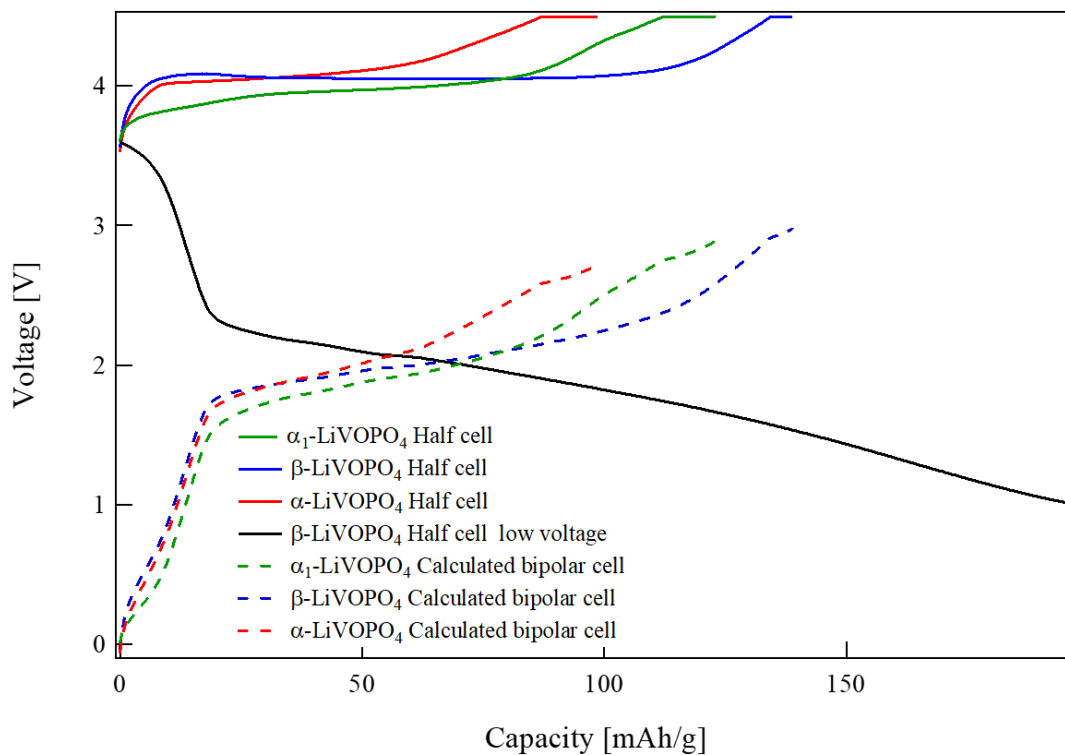


Fig. 4-10. Half cells of charge profile for each crystal phase and of discharge profile for  $\alpha_1$ -LiVOPO<sub>4</sub>. The dash lines are calculated charge profiles of bipolar cell using  $\alpha_1$ -LiVOPO<sub>4</sub> as the anode.

#### 4. 4 Conclusions

By using  $\text{LiVOPO}_4$  with different crystal phases for the anode, we were able to show that the voltage profiles completely differed. It became clear that, in the fabrication of bipolar batteries using  $\text{LiVOPO}_4$ , the use of  $\beta\text{-LiVOPO}_4$  and  $\alpha\text{-LiVOPO}_4$  for the anode is appropriate in terms of cycle characteristics and rate characteristics. Which crystal phase to use for the anode will depend on the intended use of the battery. For example, when  $\beta\text{-LiVOPO}_4$  is used, the voltage profile is flat over the entire use region. A battery with such a voltage profile would be useful for devices that always require the same voltage. When  $\alpha\text{-LiVOPO}_4$  is used for the anode, three inflection points appear in the voltage profile. For devices whose states of capacity need to be clarified, it is easy to estimate the remaining amount of capacity from this inflection point.

## Reference

- 1 W. Mao, H. Tang, Z. Tang, J. Yan, and Q. Xu, *J. Electrochem. Lett.*, **2** A69 (2013).
- 2 H. Zhou, Y. Shi, F. Xin, F. Omenya, and M.S. Whittingham, *Appl. Mater. Interfaces*, **9** 28537 (2017).
- 3 Y.C. Lin, B. Wen, K.M. Wiaderek, S. Sallis, H. Liu, S.H. Lapidus, O.J. Borkiericz, N.F. Quachenbush, N.A. Chernova, K. Karki, F. Omenya, P.J. Chupas, L.F.J. Piper, M.S. Whittingham, K.W. Chapman, and S.P. Ong, *Chem. Mater.*, **28** 1794 (2016).

# Chapter 5

## **Conclusions**

LIBs have been widely used in devices that require portability, such as mobile phones and notebook PCs, because of their high energy density. More than 20 years have passed since LIBs entered the market, during which time energy density has more than doubled. As a result, the use of batteries has expanded, and high energy density and high power have been demanded from electric vehicles, power tools, drones, and the like. However, these requirements are premised on high safety and low cost. Considering global pollution from fossil fuels, electrification and the use of renewable energy are indispensable. For this purpose, it is essential to improve battery characteristics.

In this study, I focused on cathode active materials, which are key to determining battery characteristics. A battery's cathode active material not only has a deep relationship with its energy density but also greatly affects its safety. Therefore, a cathode active material must have both high energy density and thermal stability.

A material having a layered rock salt structure such as  $\text{LiCoO}_2$  is often used as a cathode active material. Although  $\text{LiCoO}_2$  has high energy density, when Li is removed by charging, the crystallinity becomes unstable and there is a risk of it falling into a thermal runaway. In the worst case, if the cathode falls into a thermal runaway, the battery will catch fire or explode. The cause of thermal runaway is oxygen release from the cathode. Polyanion cathode active materials are unlikely to cause oxygen release. One such material,  $\text{LiFePO}_4$ , has been recognized in the market because of its low cost and high safety, but it has the disadvantage of low operating voltage. This research focused on  $\text{LiVOPO}_4$ , which has a higher operating voltage than  $\text{LiFePO}_4$ , and investigated the possibility of deployment to secondary batteries using  $\text{LiVOPO}_4$ .

Chapter 1 describes the environment surrounding the battery, market needs, and research trends in  $\text{LiVOPO}_4$ . The purposes of this study are to develop a method of synthesizing  $\text{LiVOPO}_4$  to achieve the theoretical capacity and to improve the high C rate performance while considering mass productivity, as well as to clarify the relationship between electrochemical properties and crystal structure.

Chapter 2 describes  $\text{LiVOPO}_4$  synthesis and its battery characteristics. I succeeded in producing three phases of lithium vanadyl phosphate ( $\alpha_1\text{-LiVOPO}_4$ ,  $\beta\text{-LiVOPO}_4$ ,  $\alpha\text{-LiVOPO}_4$ ) from the same precursor, synthesized by a hydrothermal method. The phases

were formed simply by controlling the sintering temperature. I studied the relationship between their electrochemical performance and particle characterization using powder XRD, STEM, and EELS. *In-situ* heating XRD revealed the relationship between sintering temperature and generated phases of LiVOPO<sub>4</sub>;  $\alpha_1$ -LiVOPO<sub>4</sub> appeared at low temperature, and we were able to extract over 80 % of lithium (131 mAh/g) from large particles (about 500 nm).  $\beta$ -LiVOPO<sub>4</sub> appeared between 420 and 690 °C, and at C/10 showed the highest discharge capacity of the three phases (140 mAh/g). The single phase of  $\alpha$ -LiVOPO<sub>4</sub> appeared at over 720 °C. The discharge capacity of  $\alpha$ -LiVOPO<sub>4</sub> was half of theoretical capacity, but the retention of the high rate capacity was the best of the three phases. The battery performance of our LiVOPO<sub>4</sub> compared with previous reports is shown in Fig. 5. EELS mapping of Li at a full charge state revealed that particles of  $\alpha$ -LiVOPO<sub>4</sub> contributed to the electrochemical properties only below 200 nm. This study reveals that particles of  $\alpha$ -LiVOPO<sub>4</sub> below 200 nm should be considered as a prospective candidate for next-generation phosphate cathode materials.

Chapter 3 describes the electrochemical properties, crystal evolution, and thermal stability of the three LiVOPO<sub>4</sub> phases at a low-voltage region.  $\alpha_1$ -LiVOPO<sub>4</sub>,  $\beta$ -LiVOPO<sub>4</sub>, and  $\alpha$ -LiVOPO<sub>4</sub> are known as multiple lithium intercalation cathode materials. They were characterized by means of half-cell performance, *operando* XRD, XAS, and DSC. The *operando* XRD revealed differences in crystal structure evolution during charging/discharging among the three crystal phases. Although the charge/discharge profiles and the crystal structure evolution behaviors were the same among the three crystal phases in the range of 3.5–4.5 V, the profiles and behaviors differed completely in the range of 1.0–3.5 V. From the results of the DSC profiles, the thermal stability of each phase of LiVOPO<sub>4</sub> is similar to that of LiFePO<sub>4</sub> in the fully charged state.

Chapter 4 describes bipolar batteries using LiVOPO<sub>4</sub>. By using LiVOPO<sub>4</sub> with different crystal phases for the anode, I was able to show that the voltage profiles differed completely. It became clear that, in the fabrication of bipolar batteries using LiVOPO<sub>4</sub>, the use of  $\beta$ -LiVOPO<sub>4</sub> and  $\alpha$ -LiVOPO<sub>4</sub> for the anode is appropriate in terms of cycle characteristics and rate characteristics.

This study shows that it is possible to synthesize all crystalline phases of LiVOPO<sub>4</sub>

by hydrothermal synthesis with excellent mass productivity. The battery characteristics of each crystal phase were also clarified, and  $\alpha$  phase and  $\beta$  phase could show the potential as the next generation cathode active material. However, in this study, many conductive assistants were put in the electrode to increase the electric conductivity.  $\text{LiFePO}_4$  can be carbon coated on the surface of active material during synthesis process, but  $\text{LiVOPO}_4$  cannot do that. Therefore, the active material ratio in the electrode is lower than that of  $\text{LiFePO}_4$ , and it is difficult to achieve an energy density higher than that of  $\text{LiFePO}_4$ . Therefore,  $\text{LiVOPO}_4$  also needs carbon coating technology like  $\text{LiFePO}_4$ . I hope that the remaining issues will be solved and that  $\text{LiVOPO}_4$  will be installed in next-generation LIBs.

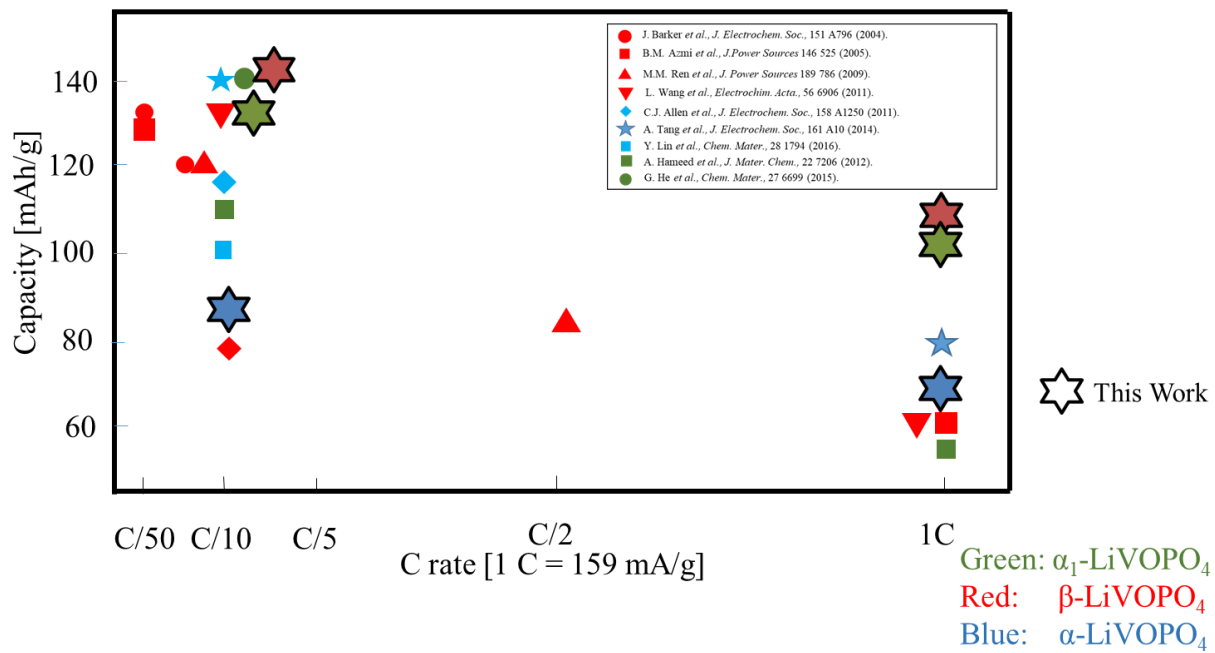


Fig. 5. The half-cell performance of LiVOPO<sub>4</sub> synthesized by our method.

## **Acknowledgement**

I would like to express my heartfelt thanks to Prof. Shigeto Okada, *Institute of Materials Chemistry and Engineering, Kyushu University*, for his kind guidance. I would also like to express my deep appreciation to Prof. Tatsumi Ishihara, and Prof. Hisahiro Einaga for their guidance in preparing the doctoral thesis.

I would also like to thank TDK Corporation and Dr. Atsushi Sano for giving me the opportunity of this research and for his great support and consideration in advancing the doctoral course for working adults.

I would like to express my gratitude to Mr. Keitaro Ohtsuki and Mr. Shin Fujita in TDK Corporation's. Advice and comments given by them has been a great help in this study.

I would like to express the deepest appreciation to Hiroki Kitamura, Yasunaga Kagaya, Kenichi Nishikawa, and Shota Goto in TDK Corporation's material analysis department for very helpful in their analysis.

I'd like to give my special thanks to my family. Their endless support and great love made me strong and confident.

Thank you so much.

January, 2020

Akinobu Nojima